Winter 1981

HIGH ENERGY COSMIC RAY CHARGE AND ENERGY SPECTRA MEASUREMENTS ABOVE 100 GEV/NUC

JON H. CHAPPELL

Chappell, Jon H.

HIGH ENERGY COSMIC RAY CHARGE AND ENERGY SPECTRA MEASUREMENTS ABOVE 10.0 GEV/NUC

University of New Hampshire PH.D. 1981

HIGH ENERGY COSMIC RAY CHARGE AND ENERGY SPECTRA MEASUREMENTS ABOVE 10.0 GeV/nuc

BY

JON H. CHAPPELL

B.S. (Physics), University of Louisville, 1972

DISSERTATION

Submitted to the University of New Hampshire

in Partial Fulfillment of

the Requirements for the Degree of

Doctor of Philosophy

Graduate School

Department of Physics

December 1981

This dissertation has been examined and approved.

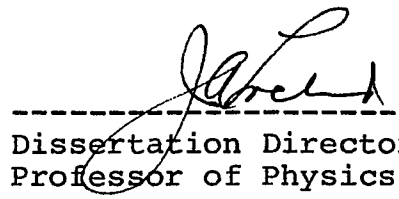

Dissertation Director, J.A. Lockwood
Professor of Physics

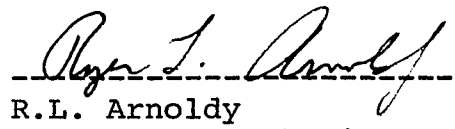

R.L. Arnoldy
Professor of Physics

L. Fisk
Professor of Physics

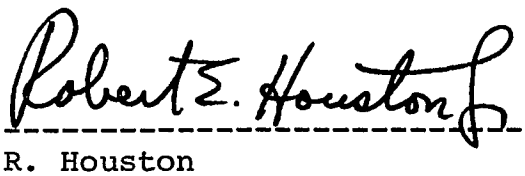

R. Houston
Professor of Physics

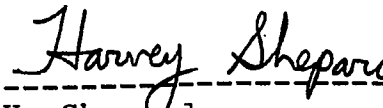

H. Shepard
Professor of Physics

17-Aug-1981
Date

ACKNOWLEDGEMENTS

It is the end of a long task, and I am now faced with the more difficult problem of adequately thanking those people who have helped and encouraged me over the past six years. Words of thanks fall desperately short of expressing my feeling towards my friends and colleagues.

I want specifically to thank:

Al Knight and Arthur Anderson, who have spent many long hours in the machining and fabrication of the parts of the experiment. They have consistently provided me with the highest quality workmanship.

Sue Horner, who has the impossible task of solving the administrative problems of the department (and the world). I'm sure that without her help and suggestions this thesis would have taken much longer.

Jack Mulhern and Barry Harrington, who are the two finest educators I have known. Their style, standards and most of all their enthusiasm for teaching are the qualities that I have admired most.

Jim Kish, who provided the mechanical and electrical engineering skills that made the balloon flight possible. Jim has provided me with a repertoire of experimental techniques and electronics that form the foundation of this thesis.

My thesis committee members, who provided me with constructive criticism and encouragement at the most crucial times.

And Margie Simpson, my loving companion, who has given me untiring support and help over the past years. Even through the most difficult of times, and the long hours spent in the lab and on the balloon flight, she has given me her love and understanding. She, more than anyone, has helped in the completion of this thesis.

The data presented in this thesis have been provided by W.R. Webber. The analysis and interpretation of the data are the sole responsibility of J. H. Chappell. Financial support was obtained through NASA Grant NGR 30-002-052.

TABLE OF CONTENTS

LIST OF ILLUSTRATIONS

page

CHAPTER I

CHAPTER II

CHAPTER III

CHAPTER IV

CHAPTER V

CHAPTER VI

CHAPTER VII

LIST OF TABLES

CHAPTER II

CHAPTER IV

CHAPTER V

CHAPTER VII

ABSTRACT

HIGH ENERGY COSMIC RAY CHARGE AND ENERGY SPECTRA

MEASUREMENTS ABOVE 10.0 GeV/nuc

by

JON H. CHAPPELL

University of New Hampshire, December, 1981

In 1976, 1977 and 1978, three balloon flights were conducted to measure the energy spectra of cosmic ray nuclei. A gas Cerenkov detector with different gas thresholds of 8.97, 13.12, and 17.94 GeV/nuc was employed to extend these measurements to high energies. The total collection factor for these flights is greater than twenty m^2 ster-hr. Individual charge resolution is achieved over the charge range Z=4-26, and overlapping differential spectra are obtained from the three flights up to $\sim$100GeV/nuc.

CHAPTER I

INTRODUCTION

A wealth of information is provided by measurement of the energy spectra and of the chemical composition of high energy cosmic rays. These measurements provide clues to the cosmic ray origin, acceleration mechanisms, and galactic cosmic ray propagation.

The questions concerning the origin and acceleration of cosmic rays are by no means resolved. In 1934 Baade and Zwicky suggested that cosmic rays were produced and accelerated by discrete supernova sources. Other theories proposed a much different origin: magnetic waves propagating through the galaxy which could accelerate particles in the interstellar medium (Fermi 1949). In more recent models (Axford et al. 1977; Bell 1978; Blandford and Ostriker 1978; Ostriker 1980) one begins to see a synthesis of these earlier models in which the energy from supernova explosions is convected away by shock waves which then accelerate the cosmic rays. These later models suggest that cosmic rays may be accelerated by shockwaves in an efficient resonant scattering process.

Differences observed between the cosmic rays and local solar system abundances are related to the nucleosynthsis process itself, to various injection and acceleration

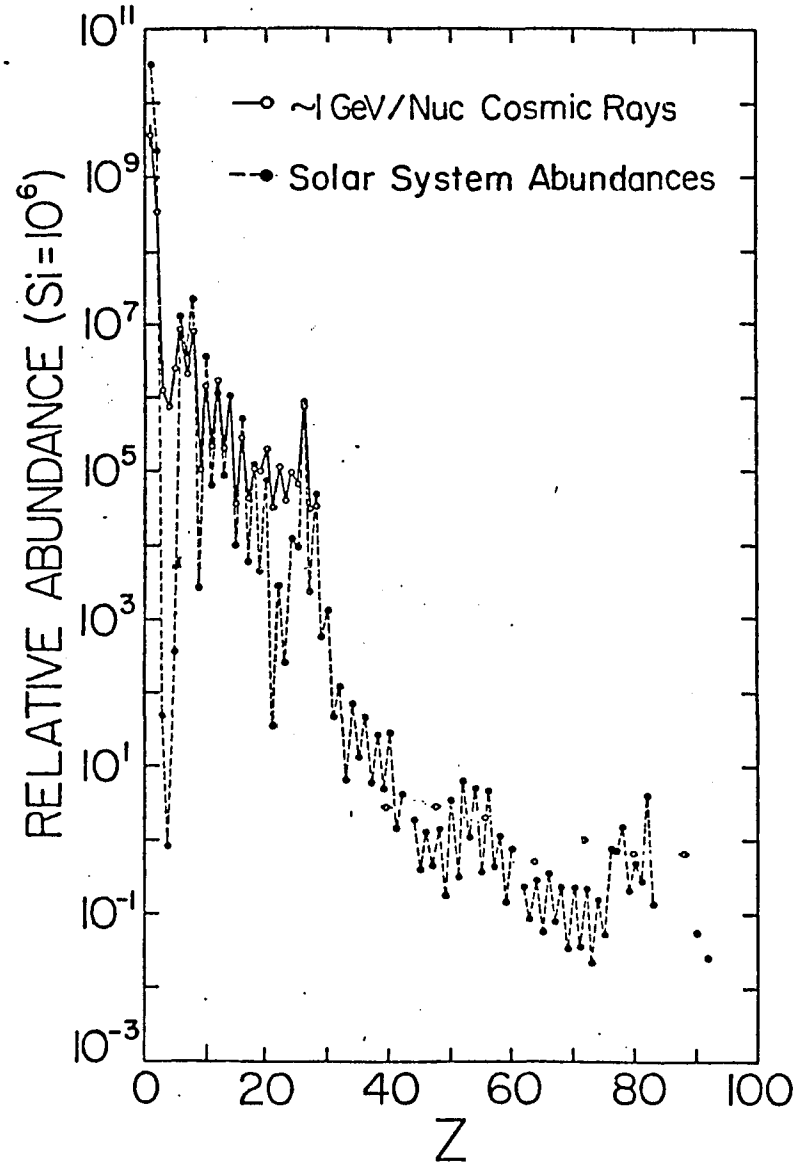

I.1 The cosmic ray abundances vs. the solar system abundances

mechanisms, to nuclear fragmentation in the interstellar medium, and to solar and galactic propagation effects. Accurate charge and energy spectra measurements of the cosmic rays are necessary in order to disentangle the questions of origin, acceleration, and propagation.

The structure of the interstellar medium dramatically affects the observed composition of the cosmic rays. As the cosmic rays diffuse away from their sources, the galactic magnetic field directs, contains, and scatters their motions. After a short period their directionality is totally randomized. During this diffusion process, the cosmic rays undergo collisions with the interstellar medium and fragment into lighter secondary nuclei. The number of the cosmic rays that undergo a spallation reaction increases as the confinement time in the galaxy increases. The resulting effect on the composition is that the abundances of certain species are enhanced and can be overabundant by a factor of 10^5 as compared to their solar system counterparts as shown in Figure I.1. One of the difficulties in the deconvolution of the observed spectra back to the source spectra is that these spallation reactions are energy dependent. One of the benefits of a high energy measurement is that the cross sections and ionization energy losses have reached their asymptotic value above a few Gev/nuc. One other advantage of measuring the high energy spectra is that these high energy particles have a shorter residence time

(ie. traverse less material) in the interstellar medium before they reach the earth. The composition we observe approaches that of the source as the amount of material traversed becomes less.

Perhaps the most exciting information in this thesis comes from the measurement of the relative abundances of the fragmented secondary nuclei compared to the parent nuclei. By systematic investigation of various secondary to primary ratios one is able to determine the distribution of path lengths in the interstellar medium needed to reproduce the observed ratics, since the amount of material traversed is directly proportional to the production of the secondary components. Observations of these secondary to primary ratios at various energies give direct evidence of the material content of the interstellar medium. The actual shape of the pathlength distribution provides constraints on the age and distribution of cosmic ray sources. The pathlength distribution is perhaps one of the most significant measurements to be made in the study of the propagation of cosmic rays in the interstellar medium.

Observations at lower energies by Garca Munoz et al. (1977) and Lezniak and Webber (1978b) suggest that the distribution of pathlengths shows an absence of the shorter pathlengths. In the high energy range an important feature observed is that the secondary to primary ratios are energy

dependent above a few GeV/nuc. As one samples the higher energies the ratios decrease in value. One explanation for this is that the higher energy particles have a shorter residence time in the interstellar medium than the lower energy particles, thereby reducing the amount of secondary fragmentation.

I-2) PROPAGATION MODELS

There have been several proposed propagation models to explain the features found in these observations. (A more detailed discussion of cosmic ray propagation is presented in Chapter VI.)

1) The "leaky box" model. This model is a first order approximation derived from the cosmic ray transport equation with the assumption that the galaxy is a closed box where uniform mixing of cosmic rays occurs (ie. with no spatial gradients). This model assumes that the particles encounter the boundary such that the probablity of escape is low. The diffusion term in the transport equation is replaced by a generalized loss or escape term. This yields a solution leading to a distribution of pathlengths that is an exponential of the form

$$P(x) \sim \exp\left[-x/\lambda_e\right] \qquad (1.1)$$

Where λ represents a characteristic escape mean free path.

2) The "double leaky box" model. This model by Cowsik and Wilson (1975) proposes a physical model demanding that the cosmic rays propagate through a shell of matter surrounding the source which is characterized by λ_1. This is followed by the cosmic rays escaping and propagating through material in the galaxy in a leaky box model with an escape mean free path characterized by λ_2. λ_1 is energy dependent and λ_2 is energy independent. The resultant pathlength distribution is a convolution of two exponential pathlength distributions. This yields a pathlength distribution function deficient in the short pathlengths. The energy dependence of λ_1 is designed to reproduce the energy dependent effects observed in relative abundances of the high energy events.

3) The diffusive models. These models take advantage of the full transport equation using different initial and boundary conditions. The solution to the diffusive model with certain boundary conditions will give results similar to those of the leaky box model: however, the physical interpretation of the propagation mechanisms will differ. For example, the "no near source" model of Lezniak and Webber (1978b) uses the full transport equation with boundary conditions that demand that the observer be located in the galaxy far from any nearby cosmic ray sources. This

diffusion model produces an exponential distribution of pathlengths that is deficient in short pathlengths similar to the double leaky box.

The dynamic halo model of Owens and Jokipii (1977) and of Jones (1979) assumes that the cosmic rays diffuse in the galactic disk with a constant diffusion coefficient and are eventually convected into the halo region which is characterized by a near zero density. This model reproduces the observed energy dependence of the mean amount of matter traversed, as does the leaky box model, by constructing a "double zone" (galaxy and halo) model with differing physical parameters. Both models predict the mean age of the cosmic rays as indicated from the Be measurements.

4) The "Closed Galaxy" model. This model by Peters and Westergard (1977) proposes a propagation model that is characterized by a steady state injection of cosmic rays by sources located in the spiral arms. Once the cosmic rays are injected, they are confined in the spiral arms by the galactic magnetic fields. The particles that diffuse across the field lines and escape from the spiral arms will diffuse rapidly throughout the galactic disk and the galactic halo. The model implies that the observed cosmic rays are being sampled from two populations: 1) "young" species which are the particles trapped in the spiral arms, and 2) "old" species which have diffused into the galactic disk and halo

confinement volume. The relative abundances that this model predicts show a decrease in the secondary to primary ratios as a function of energy above ~10 GeV/nuc. This is due to the fact that the younger species will traverse less matter with increasing energy before they escape from the spiral arms. However, at energies above ~ 100 GeV/nuc the model shows a marked increase in the secondary to primary ratios as a function of energy because with increasing energy the population of the young species decreases and the old species population will begin to dominate causing the secondary to primary ratio to rise to an equilibrium value.

I-3) EXAMPLES OF PREVIOUS EXPERIMENTS

Two major difficulties present themselves when measuring cosmic rays with energies greater than ~ 10. GeV/nuc.: 1) that of properly identifying the charge, and 2) that of determining the energy of the incident particle. Not only is the instrumentation difficult but to overcome the problem of low fluxes at these energies demands large geometry factors and long exposures. Several different instrumentational approaches to these problems have been made.

The following list summarizes the high energy experiments made to date.

Juliusson (1974). This experiment consisted of a combination of solid scintillators and solid Cerenkov detectors used for charge determination. These were combined with two gas Cerenkov counters as shown in Figure I.2. This instrument was flown three times in different configurations with Cerenkov thresholds of 24, 31, and 40 GeV/nuc. A total collection factor of ~7.6 m^2 sr hr was achieved.

Caldwell (1977) used a similar instrument as shown in Figure I.3. The instrument was flown twice with a Cerenkov thresholds of 19. and 30. GeV/nuc for a total collection factor of ~ 4.5 m^2sr hr.

Orth et al. (1978) employed a magnetic spectrometer in combination with solid scintillators as shown in Figure I.4. This covered the energy range from 2 to 150 GeV/nuc with a collection factor of .706 m^2sr hr.

Simon et al. (1979). This experiment consisted of 1) a gas Cerenkov detector with a threshold of 16.5 Gev/nuc.; 2) an array of scintillators for charge and position measurement; and 3) a total energy calorimeter. The instrument configuration is shown in Figure I.5 and was flown for a total exposure factor of 9.8 m^2sr hr.

Lezniak and Webber (1978) used a detector array containing a gas Cerenkov detector that was the forerunner of the instrument described in this thesis and which will not be discussed here.

The results of the above experiments will be shown and discussed in Chapter VII.

The measurements presented in this thesis represent improvements over previous measurements in two areas. 1) These measurements have the greatest statistical accuracy over a large energy range of any measurements made to date. 2) By demanding a consistency between the integral and differential fluxes with regard to the three balloon flights with different gas Cerenkov energy thresholds, we believe we have been sucessful in removing systematic errors in the derivation of the high energy cosmic ray energy spectra.

This thesis has been divided into six major divisions. Chapter II begins with a physical description of the cosmic ray telescopes. Chapters III and IV discuss the problems and derivation of the charge and the energy spectra of the cosmic ray particles. Chapters V, VI, and VII are devoted to the presentation and discussion of the results.

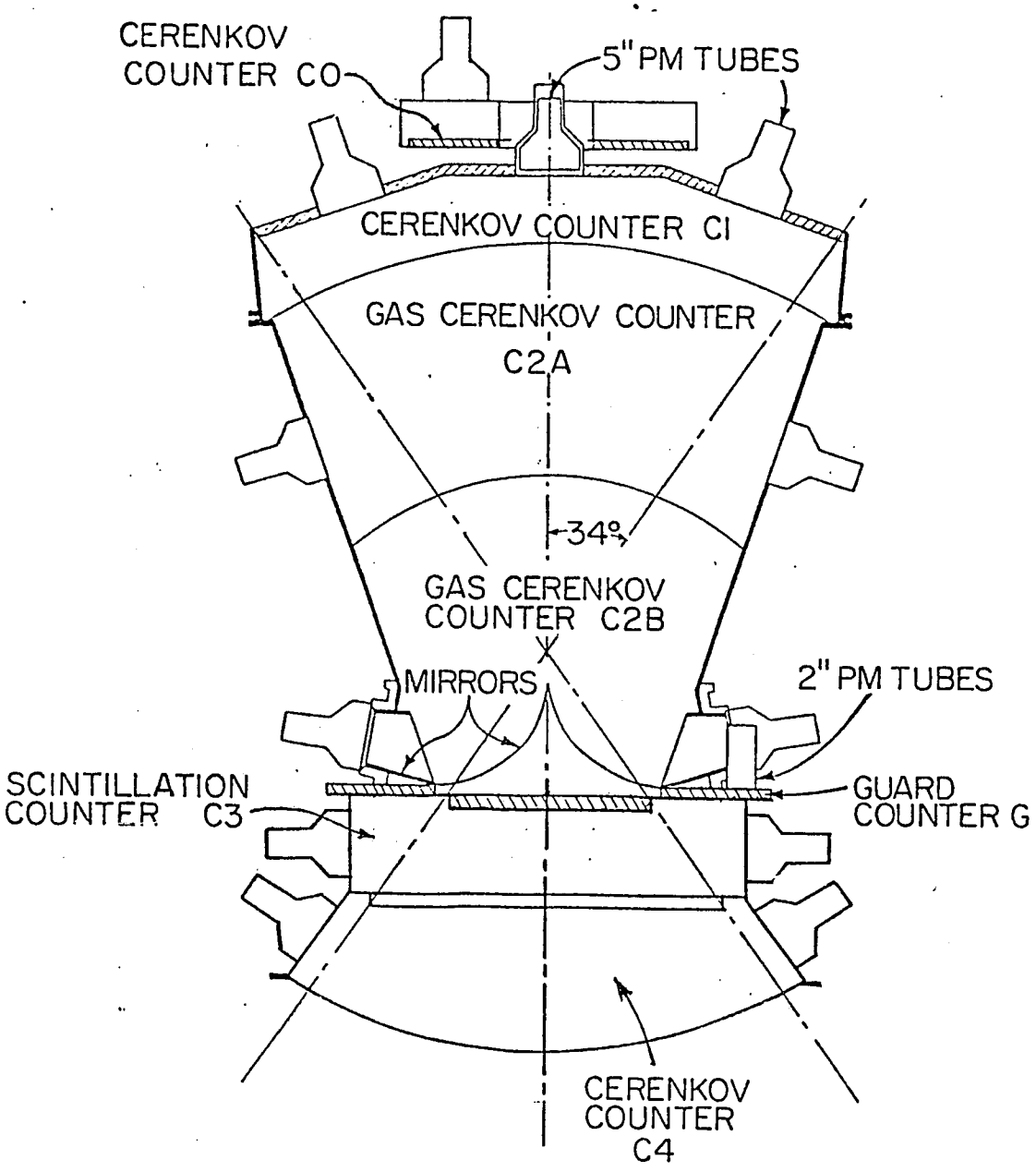

I.2 Univ. of Chicago (Juliusson) experiment design

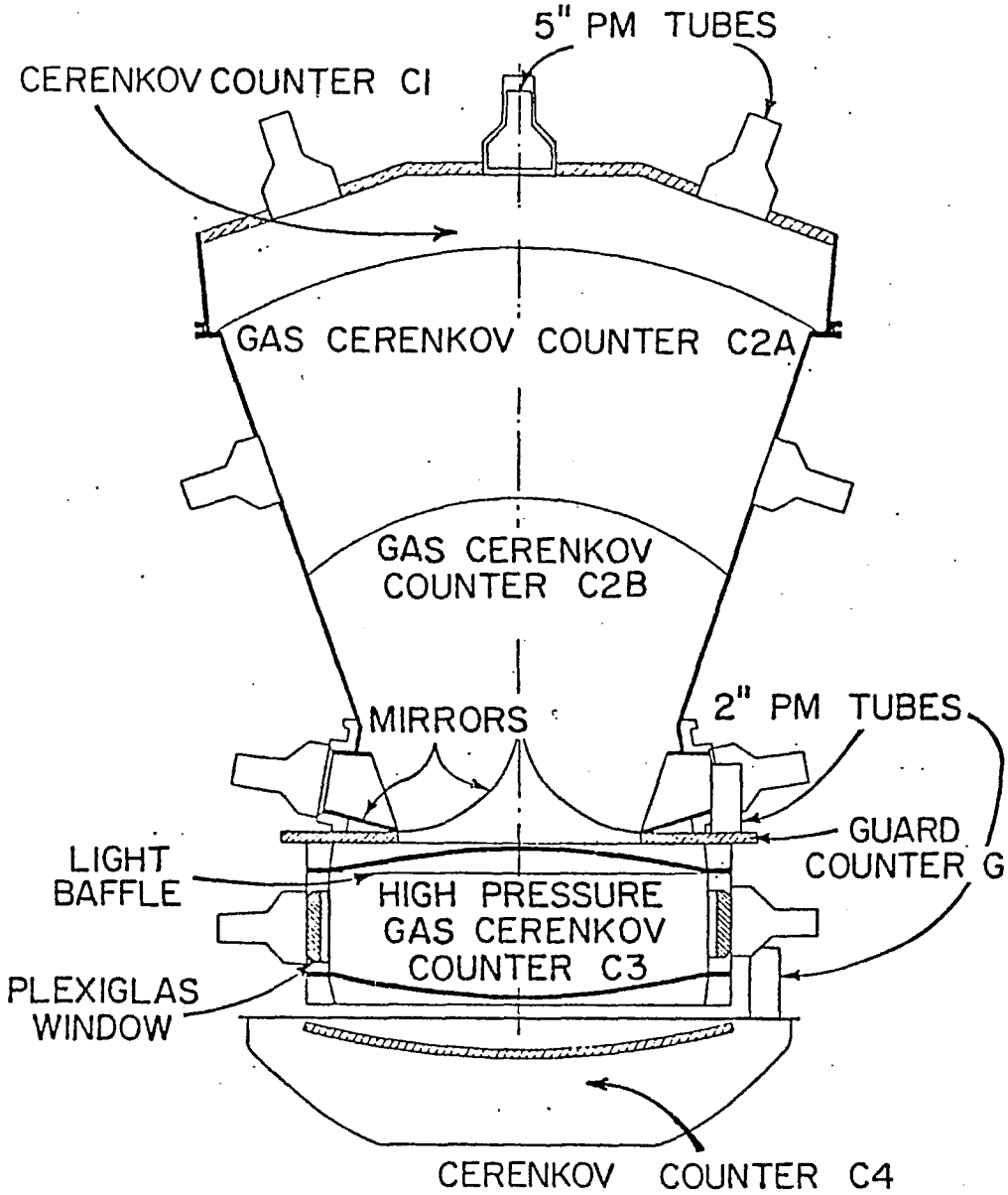

I.3 Univ. of Chicago (Caldwell) experiment design

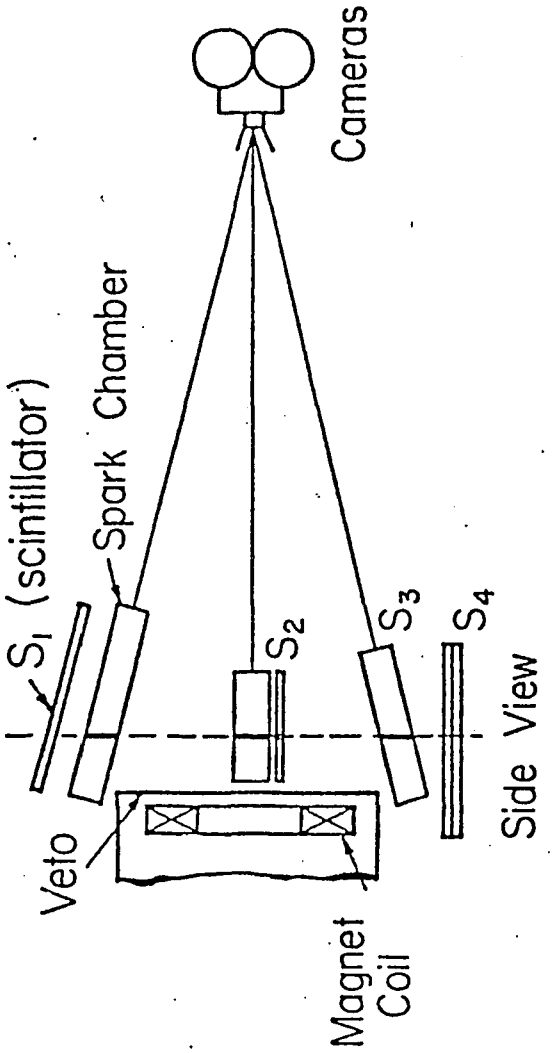

I.4 Univ. of California, Berkeley (Orth) experiment design

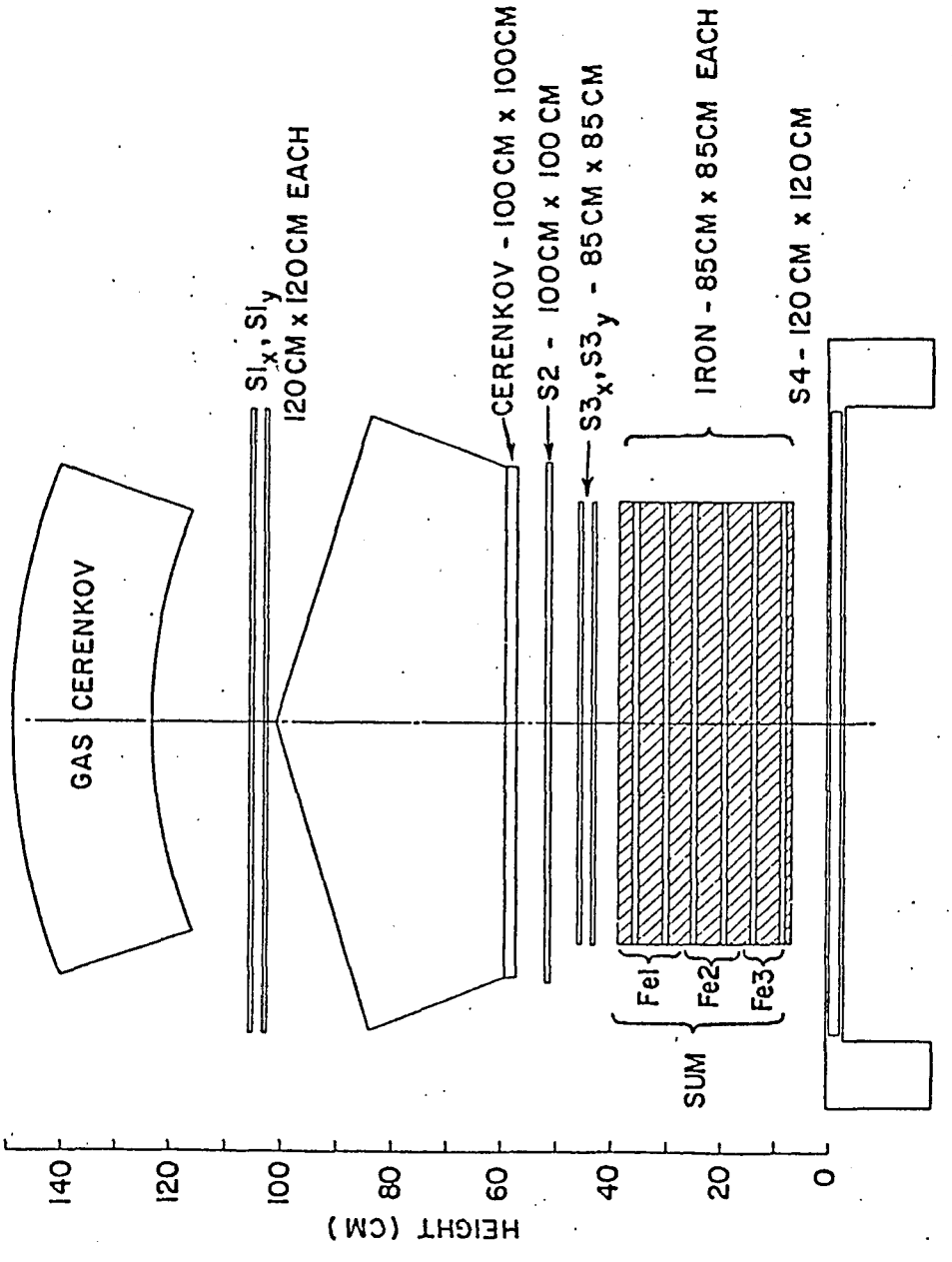

I.5 Max Planck Institute - Goddard Space Flight Center (Simon) experiment design

CHAPTER II

INSTRUMENT DESCRIPTION AND BALLOON FLIGHTS

Schematic diagrams of the instruments are shown in Figures II.1, II.2, and II.3. These were multipurpose instruments designed to perform low energy isotope measurements as well as measurement of the chemical composition of the high energy cosmic rays.

For the high energy measurement each instrument contained:

1) A gas Cerenkov detector used to determine the particle velocity above the Cerenkov threshold.
2) A multi-element array of solid Cerenkov and scintillator counters used to determine the charge and the low energy cosmic ray spectra from ~320 MeV/nuc to ~4 GeV/nuc, and the pathlength corrections.

Below is a short description of the more important detector elements.

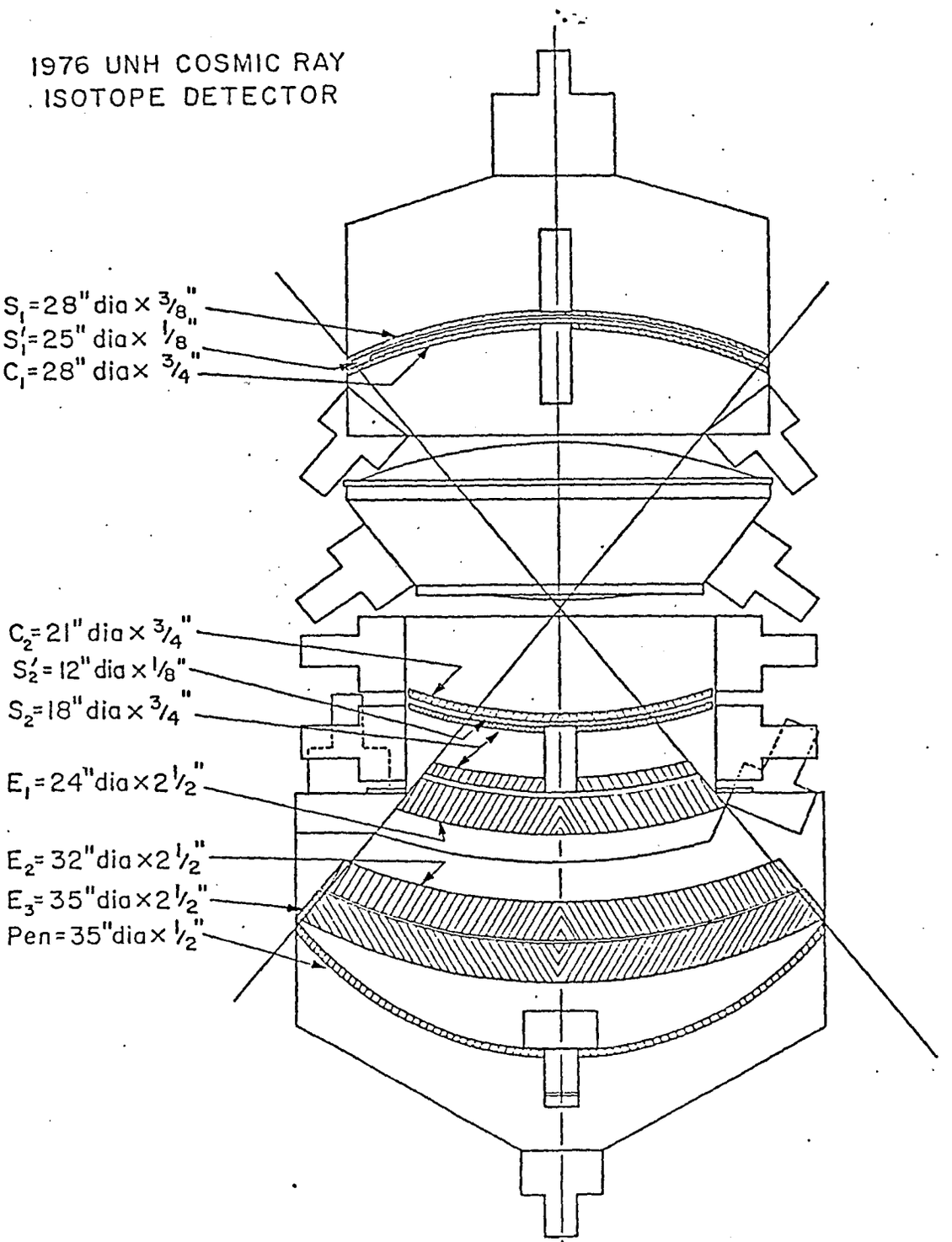

II.1 1976 UNH cosmic ray telescope

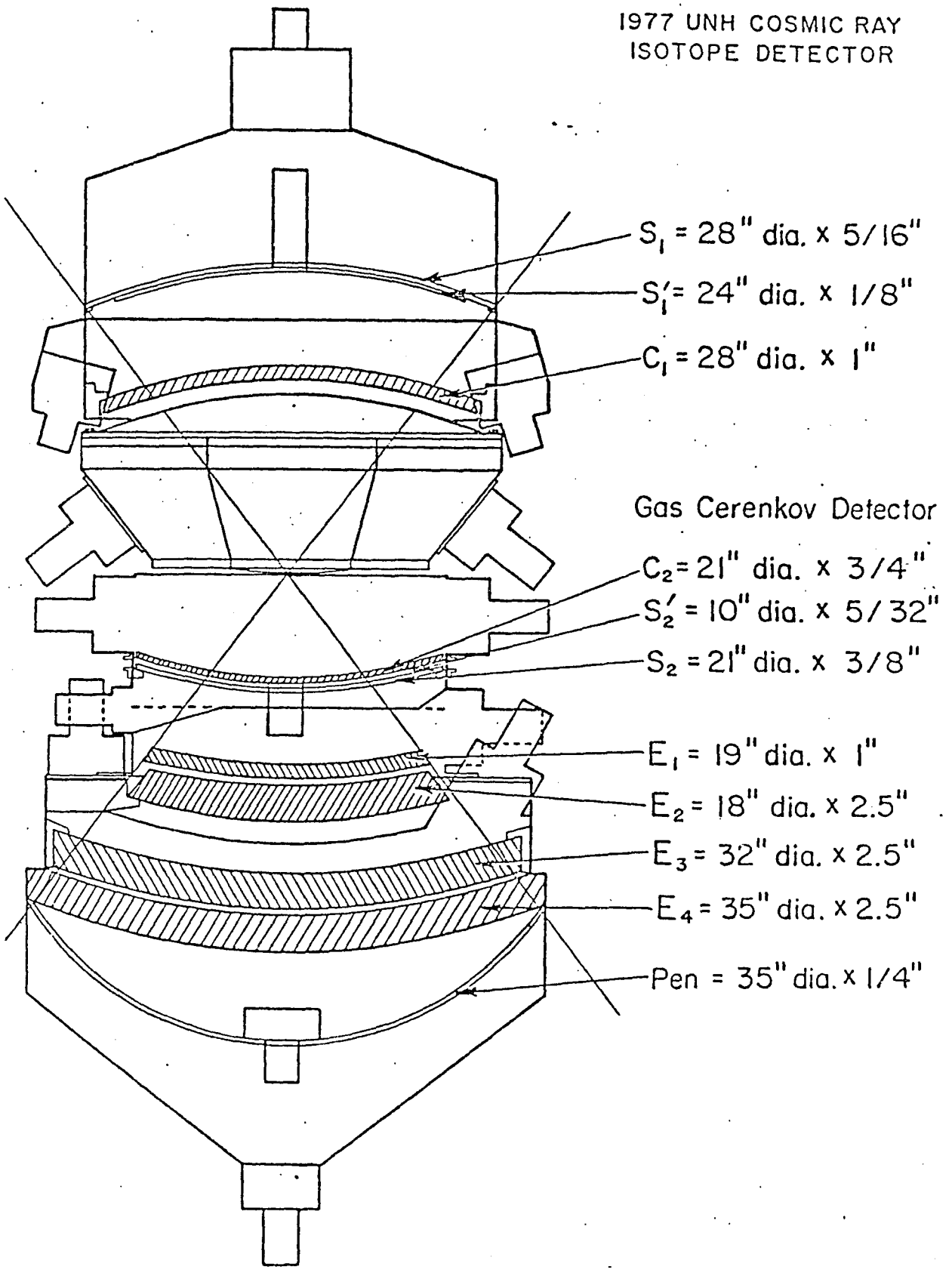

II.2 1977 UNH cosmic ray telescope

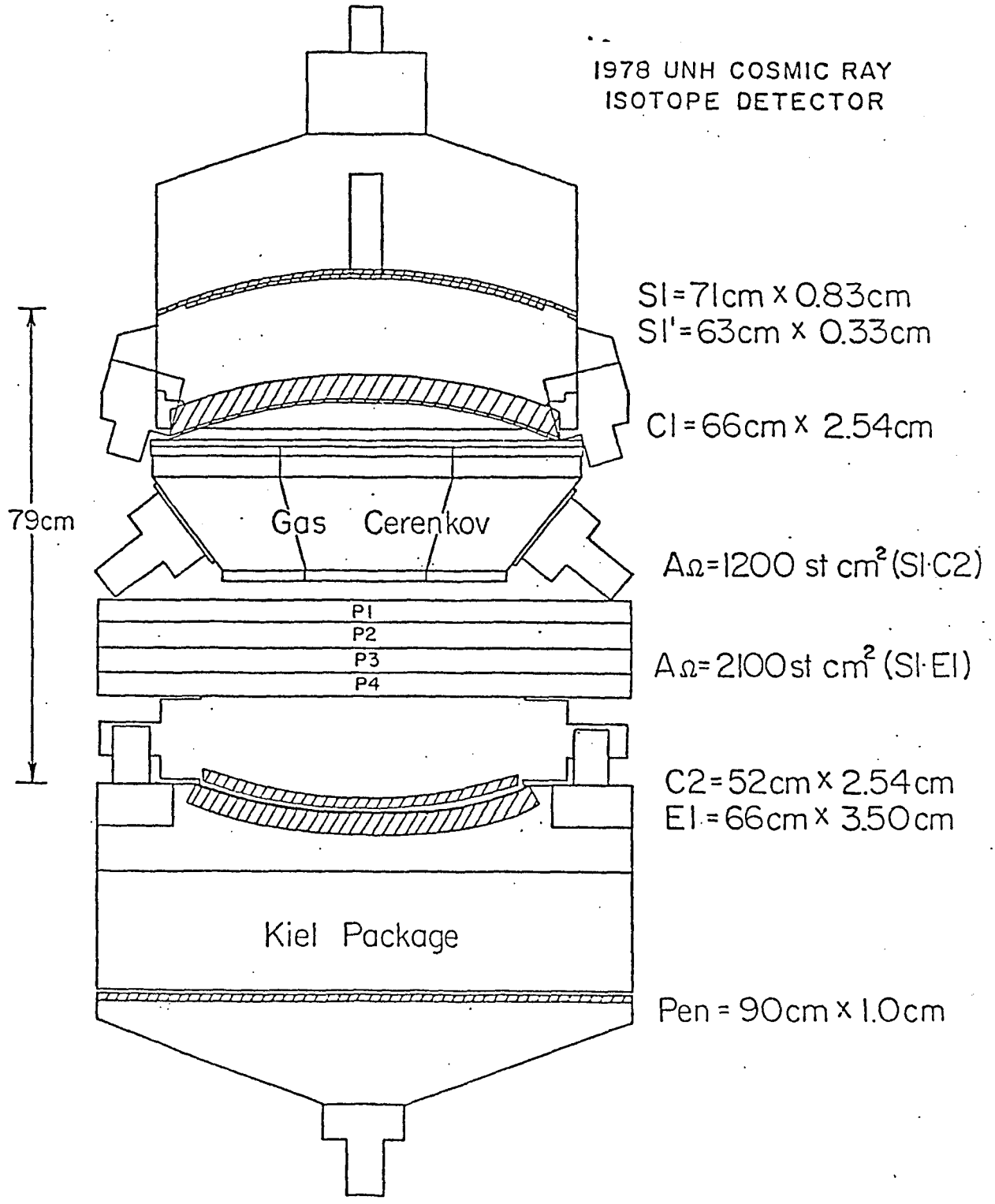

II.3 1978 UNH Cosmic Ray Telescope

II-2) THE GAS CERENKOV DETECTOR

The Freon-12 gas Cerenkov detector was flown at different pressures for each flight. Pressures of 58.0, 29.11, and 16.11 psia were used in 1976, 1977, and 1978 respectively. This gives an index of refraction of 1.00451, 1.00223, and 1.00123 which corresponds to energy thresholds of 8.97, 13.12, and 17.94 Gev/nuc.

The light collected from the 25.0 cm thick Freon-12 gas detector was diffusively reflected by a .030 cm thick layer of BaSO paint. The Cerenkov photons were then collected by two separate banks of 4 five inch photomultiplier tubes (EMI 9791 B). The resolution of the detector varied as a function of pressure yielding resolutions of 108.8%, 147.9% and 212.0% FWHM for $\beta = 1$, Z=1 particles. This translates to 6.3, 3.4, and 1.7 photoelectrons respectively. The techniques used in determining the gas counter resolution is discussed in Chapter IV-4. A thin, curved baffle was installed in the gas detector to reduce the path length variations. The resulting path length distribution function had a FWHM of 14.0%.

The two banks of photomultiplier tubes were matched by observing the light from a light emitting diode placed in the center of the detector. The matching was further verified by comparing the light output from ground level

muons.

II-3) THE CHARGE MODULE

The charge module consists of the solid scintillators S1, S1' and S2 and the solid Cerenkov detectors C1 and C2 (see Figures II.1, II.2, II.3). These detectors were used to identify the charge, the events that interacted in the telescope, and the radial entry point of the cosmic ray in the telescope.

The S1, S1' detector consisted of two photomultiplier tubes viewing the same plastic scintillator. The NE 102 scintillator has a 28 inch diameter and a radius of curvature of 34 inches. The detector thickness was .819 gm/cm^2 (t=.794cm, ρ=1.032 gm/cm^3). The S1 detector consisted of a 7 inch photomultiplier tube (EMI D445) viewing the entire scintillator in a diffusive white box. The plastic was compensated by a white mask technique such that the pulse height variations from a monoenergetic MeV electron source (Bi 207) was less than 2% over the area of this scintillator. The detector was curved in order to reduce the path length variations.

The S1' detector consisted of a 2 inch photomultiplier tube (EMI 9656) which was optically coupled to the center of the NE 102 plastic inside the white diffusion chamber.

The pulse height in the S1 detector is a function of Z^2 and β of the incident particle. The S1' views the same detector, but the tube is optically coupled to the plastic therefore the pulse height in the S1' detector is proportional to Z^2 , β , and w(r), where w(r) is the radial attenuation function. It follows that:

$$2.1) \qquad \frac{S1'}{S1} = \frac{S1'(Z^2, \beta, w(r))}{S1(Z^2, \beta)} \cong w(r)$$

This implies that the ratio of S1'/S1 is related to the radial attenuation function w(r). Radial maps were made prior to the flights to determine the radial fall-off function w(r). Once accurately determined, w(r) can then be inverted to find the radial entry point of the cosmic ray as a function of S1'/S1. The standard deviation for determining the radial entry point is $\pm$ 3.0 cm FWHM for radii greater than 8.0 cm. All of the solid plastic detectors were curved in order to reduce the pathlength variations within the instrument. The pathlength correction factors were determined by computing the mean pathlength for all possible trajectories for a given radius in the S1 detector. The techniques for determining the pathlength corrections and their associated errors using the radial entry point have been discussed by Simpson (1977).

The remaining elements of the 1976 and 1977 charge module consist of two solid Cerenkov detectors, C1 and C2, and a second scintillator S2. These detectors were also

compensated using a white mask technique (Webber, Damle, and Kish (1972); Webber, Lezniak, and Kish (1973)). The uniformity was verified by using a collimnated monoenergetic MeV electron source. The compensation was carried out until the non-uniformities were below 2% FWHM over a wide range of random points taken over the detector surface area. By milling and sanding the UVT lucite material, thickness variations were reduced to the 1% level on all of the detectors. The surfaces on all plastic detectors were prepared in an unpolished state in order to negate the effects of any light trapped by total internal reflection. The detector walls were painted with a .040 cm thick layer of $BaSO_4$ paint.

As with the gas detector, each of the solid Cerenkov detectors are viewed by two banks of photomultiplier tubes. Table II.1 summarizes the configurations for the 1976, 1977, and the 1978 flights. Table II.2 through II.4 list the various materials and thickness associated with each flight instrument.

II-4) GEOMETRY FACTORS

The geometry factors for the telescope were defined by the S1-S2 coincidence detector elements. For the high energy mode, there existed trajectories in the telescope

which would trigger the S1-S2 coincidence but partially or totally miss the gas detector element. This necessitated a calculation of a three element geometry factor for the telescope.

The geometry factor for a two element telescope is defined by

$$2.2) \qquad G_{13} = \int_{S1}\int_{S3} \frac{(\hat{r}\cdot\vec{ds_1})\cdot(\hat{r}\cdot\vec{ds_3})}{|r|^2}$$

The three element geometry factor was determined by demanding that for each r trajectory vector defined by $d\overline{S1}$ and $d\overline{S3}$, $\hat{r}$ must pass through an area bounded by R2max as shown in Figure II.4. The three element geometry factor was then numerically calculated and the results are listed in Table II.5. Correction factors were incorporated in the collection factors that include electronic dead time and the time lost due to poor data transmission.

II-5) The Balloon Flights and Data Formats

The Fall 1976 flight took place from Sioux Falls, South Dakota on 24-Sept-1976 with a float duration of 20 hours. The 1977 and 1978 flights were conducted at Yorkton, Saskatchewan, Canada, during the Fall turnaround periods on 1-Sept-1977 and 10-Sept-1978 for a duration at float altitude of 49 and 47.5 hours respectively. The total

TABLE II.1

Summary of detector configurations

Year	detector	dimensions	of P.M. tubes
1976	S1	3/8"-28" dia.	1-7"
	C1	3/4"-28" dia.	8-5"
	Gas Cerenkov	12" -20" dia.	8-5"
	C2	3/4"-21" dia.	12-5"
	S2	3/4"-18" dia.	4-5"
1977	S1	3/8"-28" dia.	1-7"
	C1	1" -28" dia.	8-5"
	Gas Cerenkov	12" -20" dia.	8-5"
	C2	3/4"-21" dia.	12-5"
	S2	3/8"-21" dia.	4-5"
1978	S1	3/8"-28" dia.	1-7"
	Gas Cerenkov	12" -20" dia.	8-5"
	4-MWPC	22" -22"	-
	C2	1" -21" dia.	12-5"

TABLE II.2

1976 Material list

Name	material	thickness [g/cm^2]
atmosphere	air	3.80
insulation	plastic	.1422
gondola	Al	.5894
S1	NE 102	.8192
bottom S1	Al	.0138
S1'	NE 102	.3277
top C1	Al foil	.0067
C1	UVT-lucite	2.817
bottom C1	Al	.5894
gas	Freon-12	.5176
baffel	Al	.1713
gas	Freon-12	.0982
bottom gas det.	Al.	.6168
C2	UVT-lucite	2.2479
bottom C2	Al	.1380
S2'	NE 102	.3277
bottom S2'	Al foil	.1380
S2	NE 102	2.620
bottom S2	Al foil	.0069

TABLE II.3

1977 Material list

Name	material	thickness [g/cm^2]
atmosphere	air	3.30
insulation	plastic	.1422
gondola	Al	.5915
S1	NE 102	.8195
top S1'	Al	.0082
S1'	NE 102	.3276
top C1	Al	.4114
C1	UVT-Lucite	2.817
top gas det.	Al	.4183
gas	Freon-12	.2598
baffel	Al	.1713
gas	Freon-12	.0466
top C2	Al	.5486
C2	UVT-Lucite	2.098
top S2'	Al	.0082
S2'	NE 102	.4095
top S2	Al	.0082
S2	NE 102	.9829

TABLE II.4

1978 Material list

Name	material	thickness (g/cm^2)
atmosphere	air	4.25
insulation	plastic	.1422
qondola	Al	.5915
S1	NE 102	.8195
top S1'	Al	.0082
top qas det.	Al	.4112
qas	Freon-12	.2131
baffel	Al	.1645
qas	Freon-12	.0569
bottom gas det.	Al	.4112
qas shields	polyethelene	.0763
MWPC qas	P-10	.0198
top C1	Al	.1713
C1	UVT-Lucite	2.997

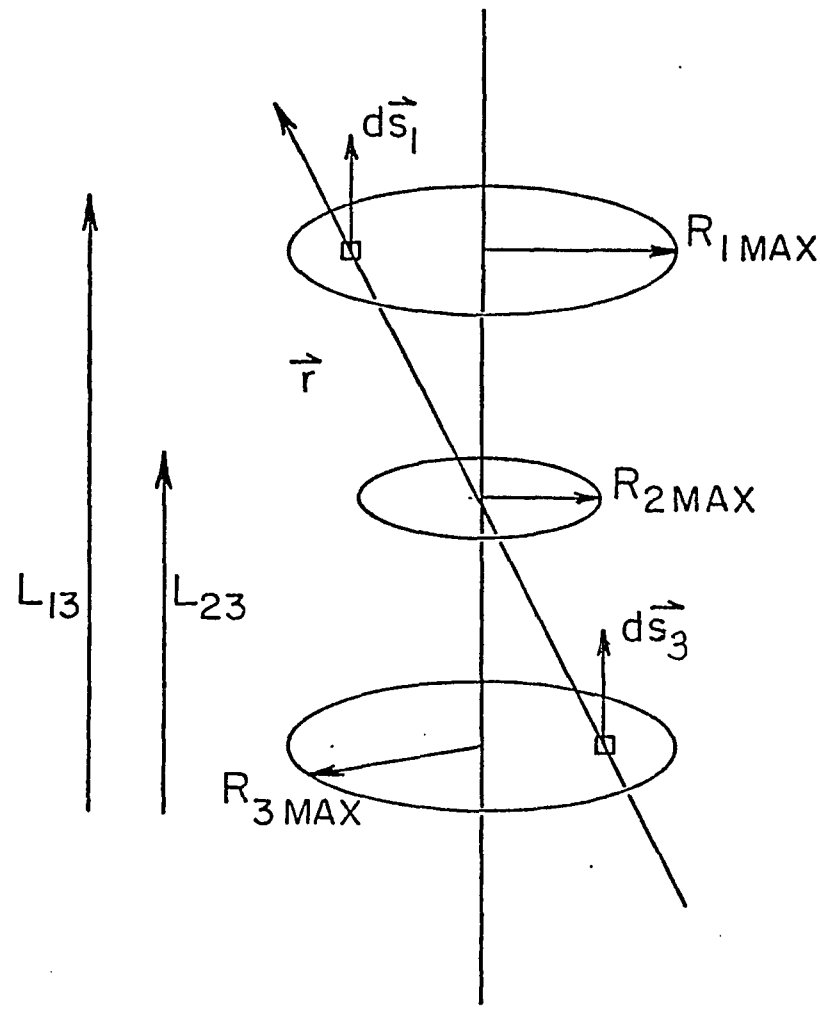

II.4 Three element geometry factor configurations

TABLE II.5

Summary of geometry and collection factors

Year	1976	1977	1978
Two element GF (cm^2-sr)	815.0	889.3	1643.3
Three element GF(cm^2-sr)	719.8	815.1	1643.3
Two element collection factor w/dead time corrections (m^2-sr-sec)	8462.0	23790.0	27119.0
Three element collection factor w/dead time corrections (m^2-sr-sec)	7463.5	22767.0	26549.5

instrument weights for the three flights were 650, 700, and 675 kg respectively. The Mt. Washington neutron monitor average daily counting rate for the three respective flight times were 2392, 2340, and 2310.

An event was defined when a signal was observed above a preselected threshold of six times minimum ionizing $\beta=1$, $Z=1$ particles in the S1-S2 coincidence elements. Each event was characterized by a leading twelve bit sync word followed by a twelve bit digitized pulse height for each of the detectors. Parity and multiplexed housekeeping bits were also included in the data stream. The data were telemetered back to the ground station at ~20 kilobits /sec. The data were then recorded on videotapes during the balloon flights and then later reformatted into seven track computer tapes.

Changes in the pulse height due to temperature changes were corrected by viewing several prominent $\beta = 1$ Cerenkov peaks such as C, O, and Fe at one hour intervals. The 1976 and 1977 flights required gain corrections that were less than five percent. The 1978 flight required no temperature corrections. Master tapes were produced that included the corrected gains and path length corrections derived from the S1/S1' detector system. These tapes were then used for the remaining data analysis.

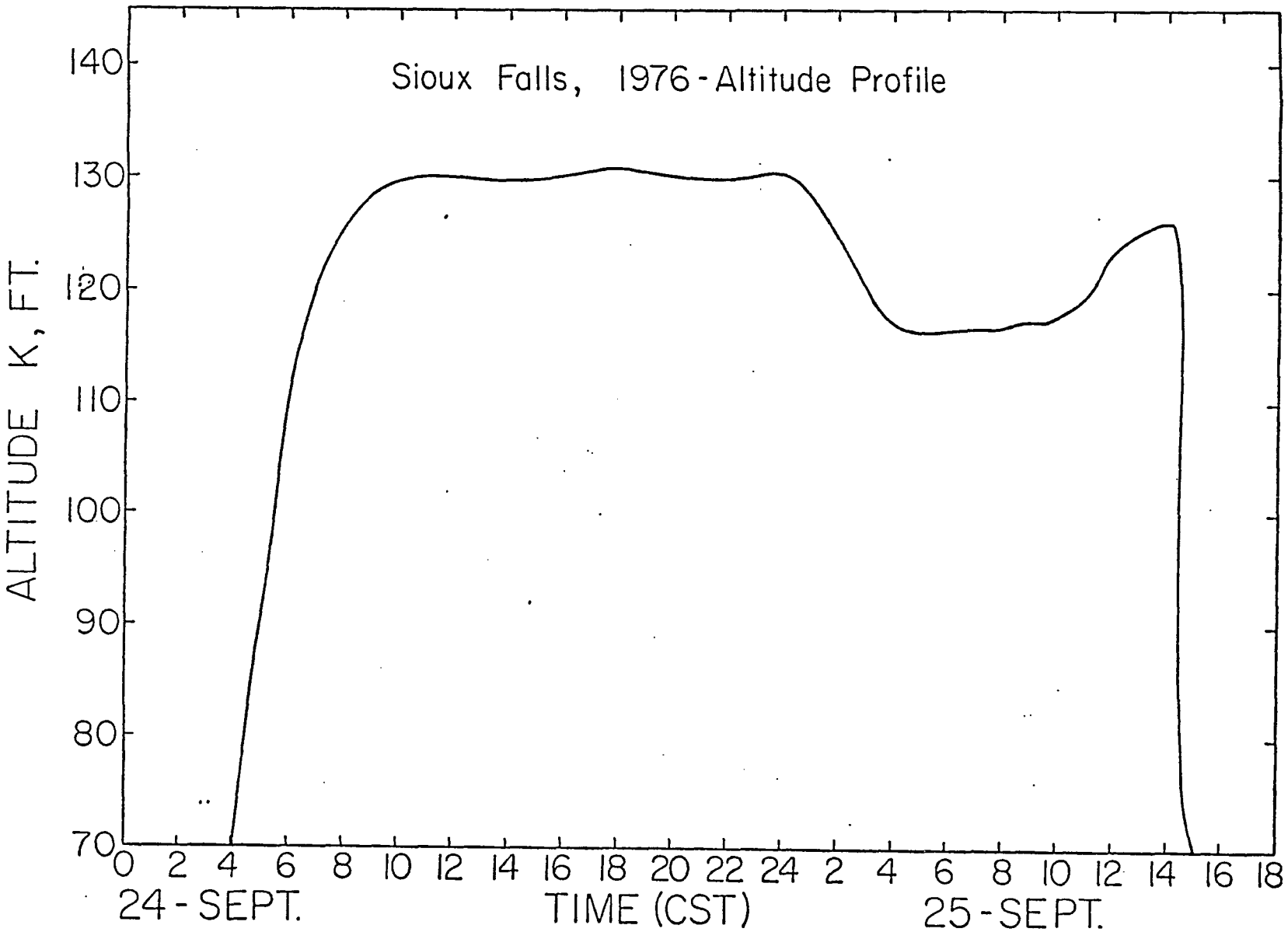

II.5 1976 altitude profile

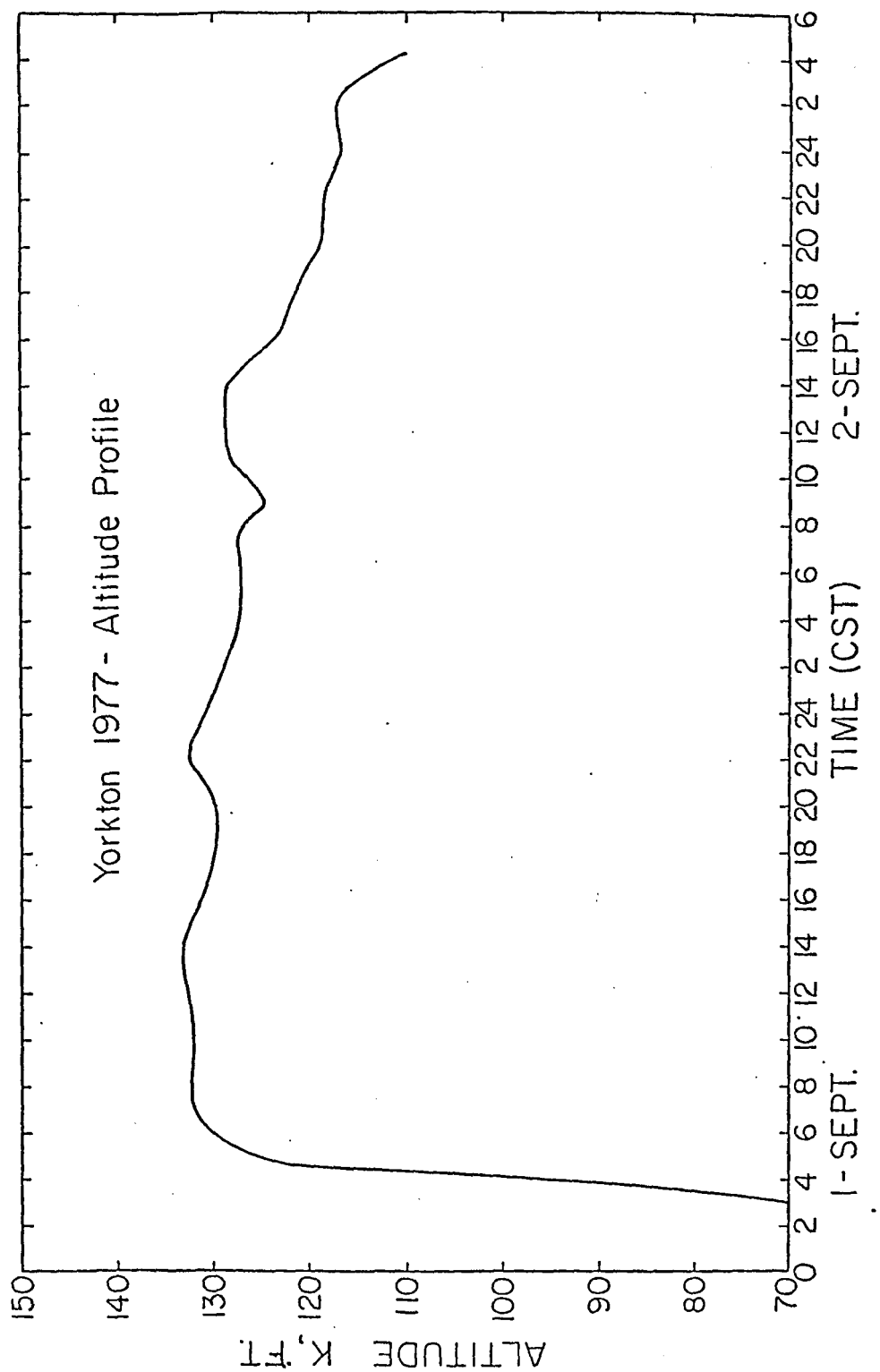

II.6 1977 altitude profile

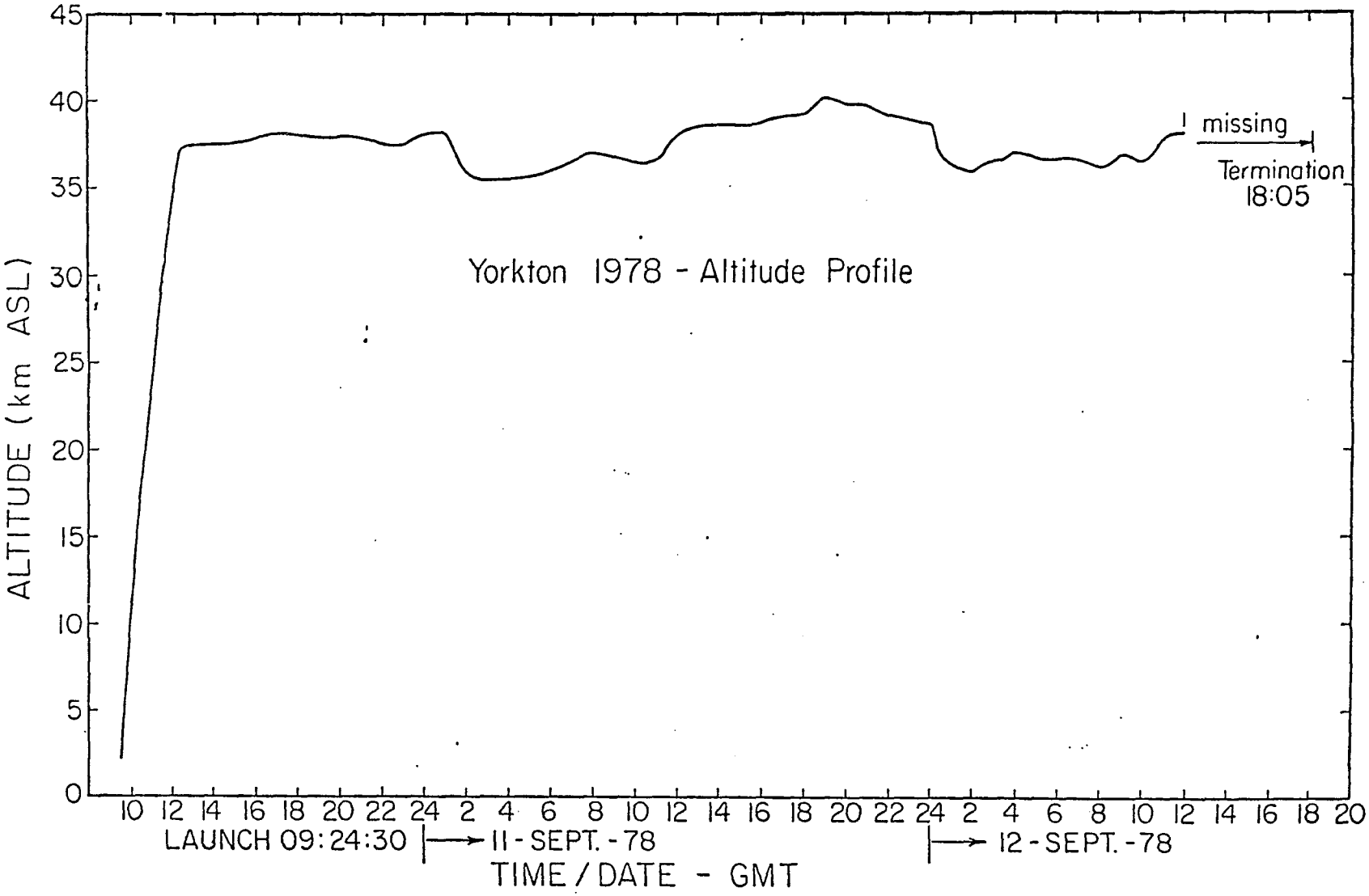

III.7 1978 altitude profile

CHAPTER III

CHARGE ANALYSIS

Ideally, the charge and energy of the nuclei would be determined by systematic observation of the different energy loss mechanisms as discussed in Sections III-1 and III-2 of this chapter. The problem is complicated by the various interactions and fluctuations associated with real detector systems. Sections III-3 through III-6 of this chapter discuss the consistency requirements that were placed on the outputs of the various detectors in order to remove the events that have interacted and fragmented in the telescope. The pulse heights of the various counters can be combined and plotted such that the charge and energy of the cosmic rays can be identified as shown in Section III-7.

The pulse height of the detectors are primarily determined by two energy loss mechanisms: ionization energy loss and Cerenkov radiation.

III-1) Ionization Energy Loss

As a charged particle traverses matter, it undergoes collisions and transfers energy by Coulomb interactions to the atomic electrons of the medium. A significant fraction of this energy loss goes into exciting or ionizing the

medium. Measurement of this scintillation light provides us with a direct link to the energy and charge of the incident particle. The rate of ionization energy loss can be expressed by the Bethe-Bloch formula as

$$3.1) \qquad -\frac{dE}{dx} = \frac{2\pi n Z^2 e^4}{mv^2}\left[\ln\left(\frac{2mv^2 \cdot W_{max}}{I^2(1-\beta^2)}\right) - 2\beta^2 - \delta - u\right]$$

where
Wmax=the maximum energy transfer from the incident particle to the target atom
I=mean excitation potential of the target atoms
n=number of electrons per cm of the target
m=mass of the electron
β=v/c of the incident nuclei
Z=charge of the incident nuclei
δ=correction factor for the density effect
u=correction factor for the inner shells (K,L,.) for low velocity particles

The rate of ionization energy loss is plotted in Figure III.1 as a function of energy. The derivation of the Bethe-Bloch formula has been discussed in detail in several references (Sternheimer(1961)).

It is true, however, in a real detector, that the observed light produced is not linearly proportional to the actual ionization energy loss of the incident particle. The saturation or "quenching effects" are most likely due to a combination of ion recombination along the particle's path and dissipation of vibrational energy into thermal energy states which are then convected away to nearby molecules resulting in a loss of photon production. The observed effects of the saturation in the scintillator result in a

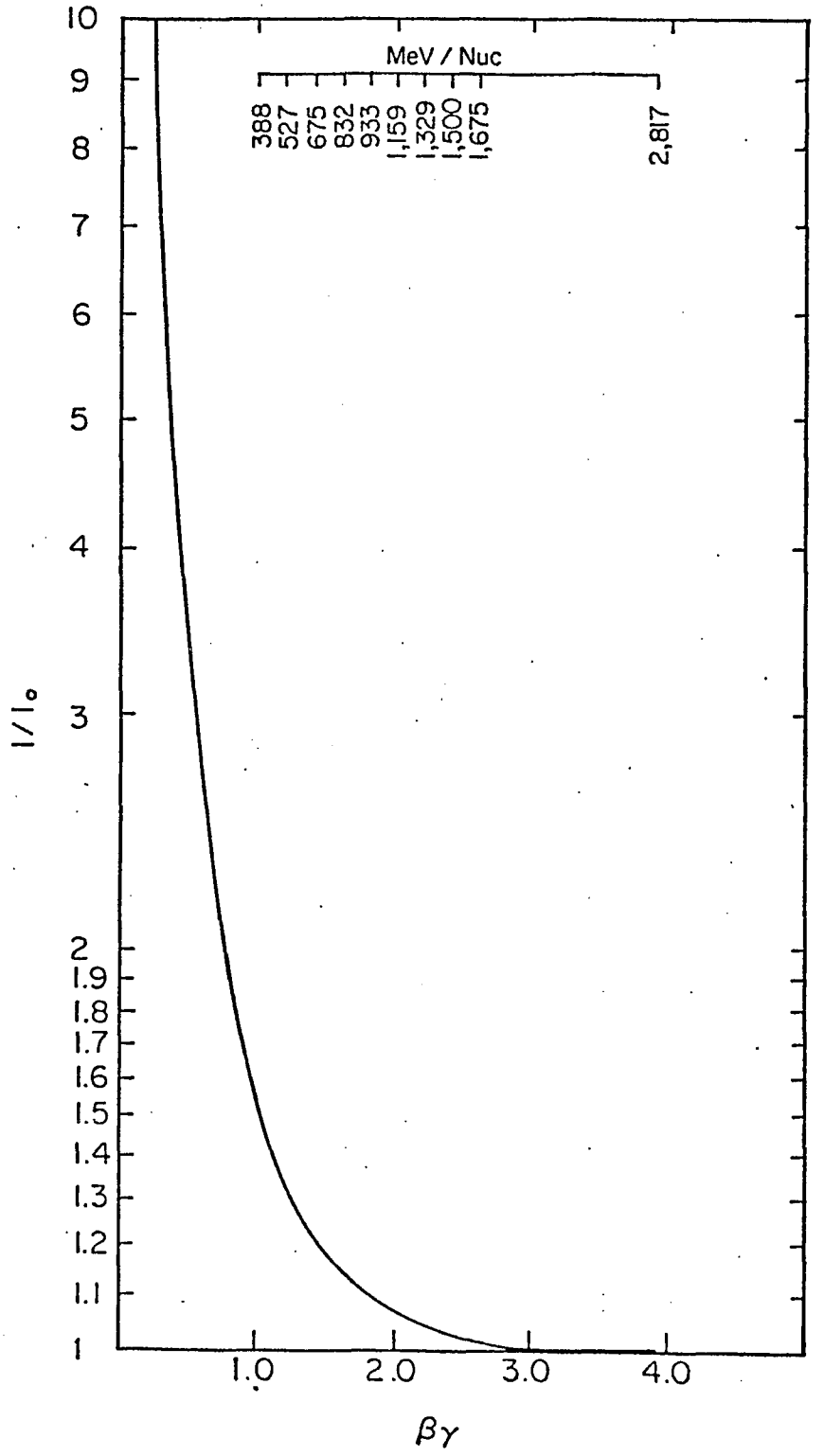

III.1 Ionization enrgy loss (dE/dX) vs. energy ($\beta\gamma$)

deviation from the expected Z and dependence predicted by the Bethe-Eloch formula. This effect is most evident in the outputs of the sum of the S+C detectors as shown in Figure III.9 . The deviation from the expected output varies as much as 40.% below that predicted by the energy loss formulas at high light outputs.

III-2) Cerenkov Radiation

When the velocity of a charged particle exceeds the velocity of light in a medium, a coherent response of the medium causes the emission of Cerenkov radiation. The radiation is directly related to the polarization (ie. density) effects of the medium. The radiation produced per unit pathlength for $\beta > 1/n$ can be expressed by

$$3.2) \qquad -\left.\frac{dE}{dx}\right|_{rad.} = \frac{Z^2e^2}{c^2}\int_{\epsilon(\omega)>(1/\beta^2)}\left(1-\frac{1}{\omega^2(\epsilon)\beta^2}\right)\omega d\omega$$

Where $\epsilon(\omega)$ is the dielectric constant. The corresponding number of phctons collected is related to

$$3.3) \qquad N = CZ^2\left[1-\frac{1}{n^2\beta^2}\right]$$

Where C is a constant that involves the spectral response of the radiation, photomultiplier tube sensitivity, and the light collection efficency. Figure III.2 shows the theoretical Cerenkov output versus energy.

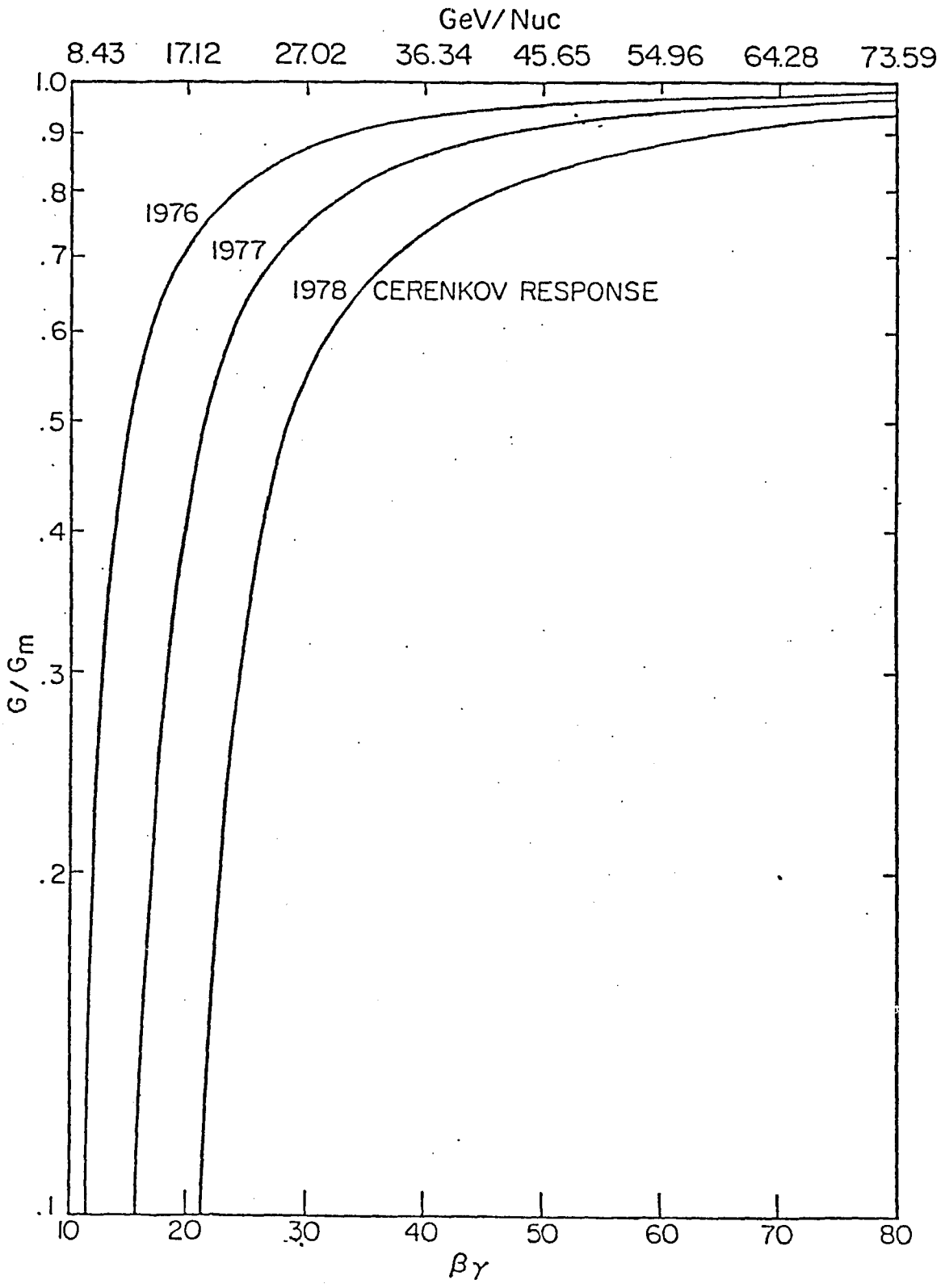

III.2 Cerenkov radiation loss vs energy ($\beta\gamma$)

With the use of these two energy loss mechanisms, one is able to identify the charge (Section III-6) and energy (Chapter IV) of an event by forming crossplots of the outputs of the various detector pairs. Before accurate determination of the charge and energy can be made, it is necessary to 1) identify and remove events that have interacted within the telescope (Section III-3), 2) select the proper energy domain and exclude the low energy events from the data analysis (III-4), and 3) identify and remove events that have exessive statistical fluctuations in the production of photoelectrons (III-5).

III-3) Consistency Requirements - S1 X S2

As the cosmic ray particle penetrates the detector, there is a significant probability that it will collide with other nuclei and undergo a spallation reaction. As many as 30% of the incident particles may fragment in the telescope. By placing consistency requirements on individual banks of each detector as well as detector pairs, one is able to to exclude a large percentage of the unwanted charge changing reactions.

Figure III.3 shows a crossplot of the S1 detector versus the S2 detector for the 1976 flight. Since the pulse heights of the two scintillation detectors are correlated as

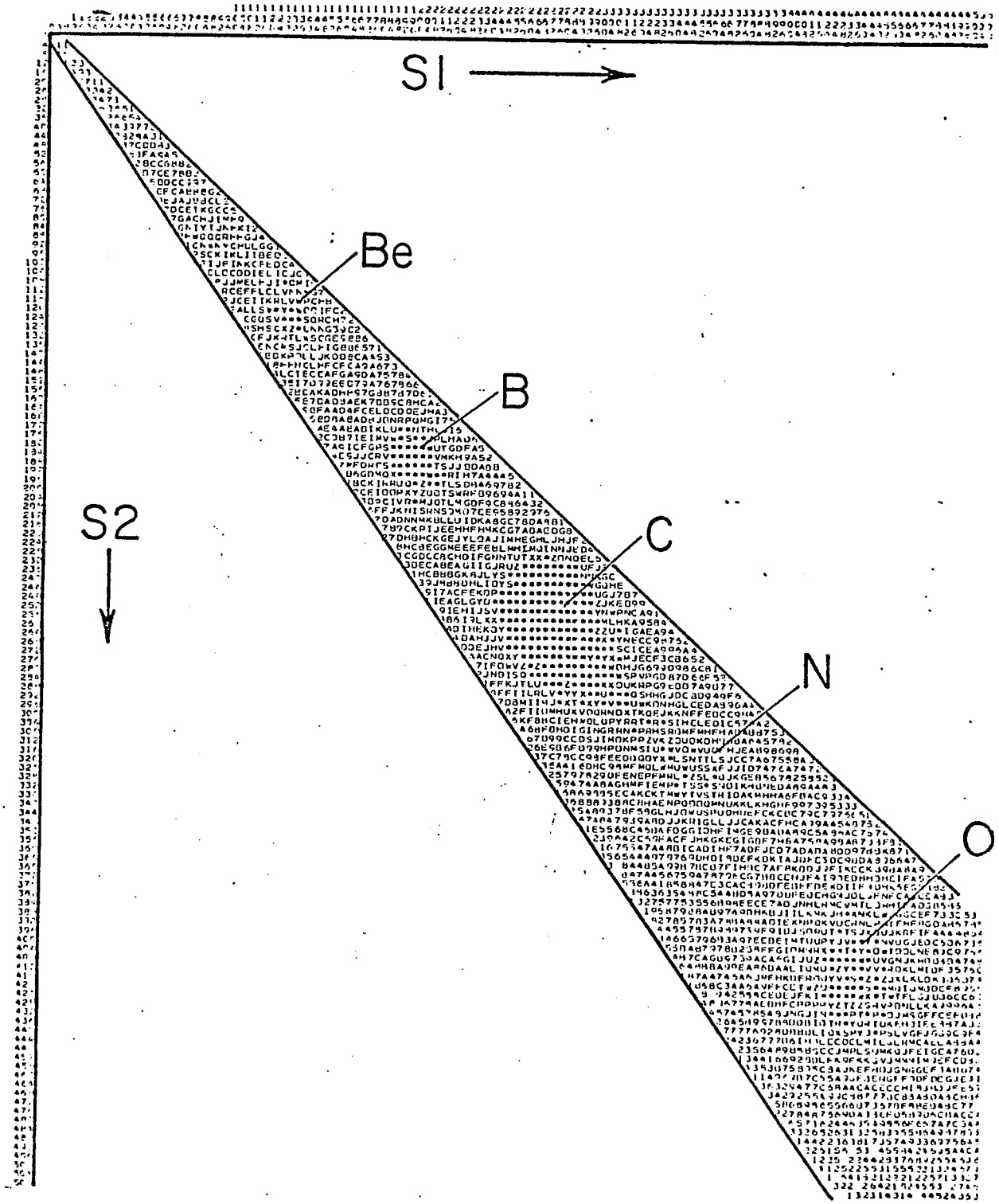

III.3 Matrix plot of S1 detector vs. S2 detector

a function of β and Z, interacting events will lie outside of the correlation zone. A selection criteria of the form

$$34) \quad \frac{|S1 - S2|}{S1 + S2} < k$$

was applied to the pulse heights of the S1 and S2 detectors, where k is a constant. In order to investigate these interacting and background events, several matrix distributions were produced with various values of k. The selected value for k was determined by the individual resolutions of each detector. The resulting criteria were calculated to remove events that have fluctuations greater than three standard deviations. This technique removes 80 to 90 % of the spallation events while removing on the order of 2. percent of the non-interacting events.

III-4) Consistency Requirements - C X S

A second criterion was applied in order to remove the low energy events from the high energy data analysis. Ideally these low energy events would lie below the gas Cerenkov threshold and would therefore have a zero pulse height in the gas detector. However, these events that lie below the Cerenkov threshold will generate a non-zero signal by producing 1) Cerenkov light in the reflective paint that coats the walls of the gas detector, 2) light produced by production of knock on electrons in the photomultier tubes,

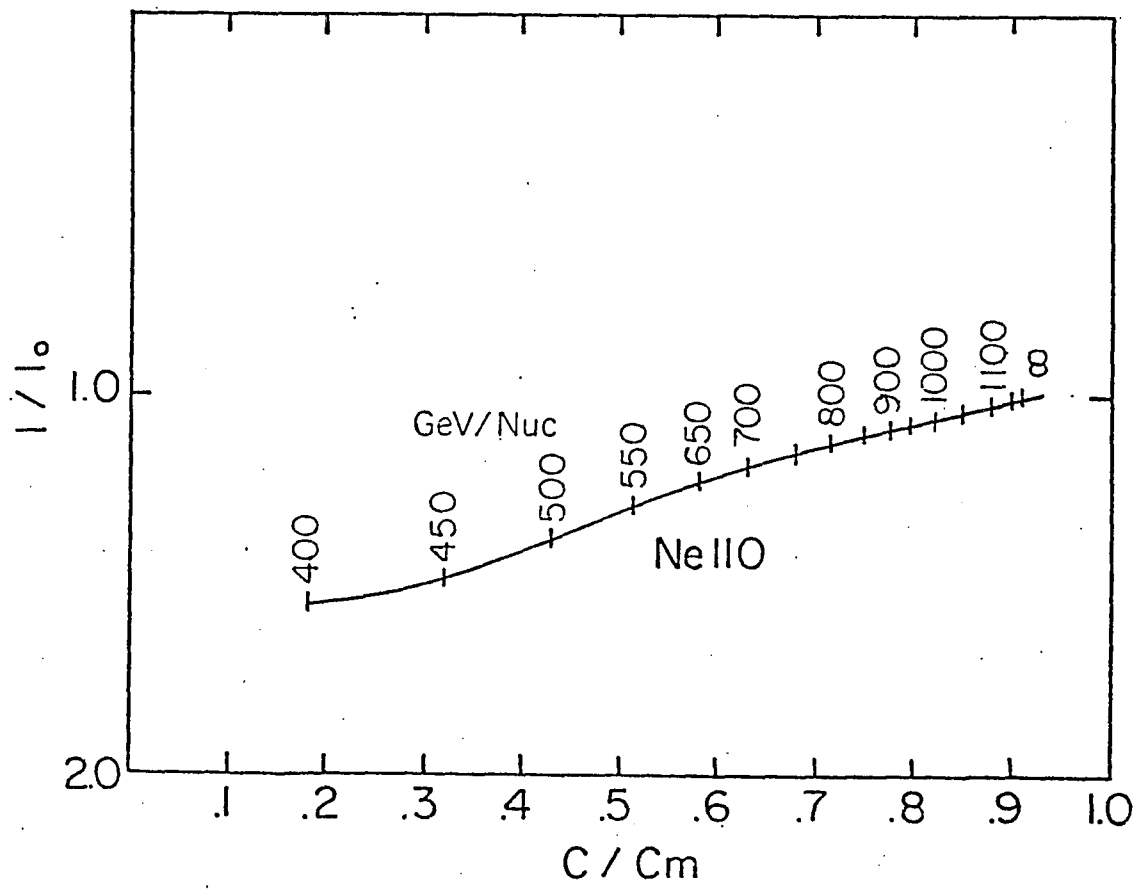

III.4 Expected distribution of events in the S1 detector vs. C1 detector for a single charge species

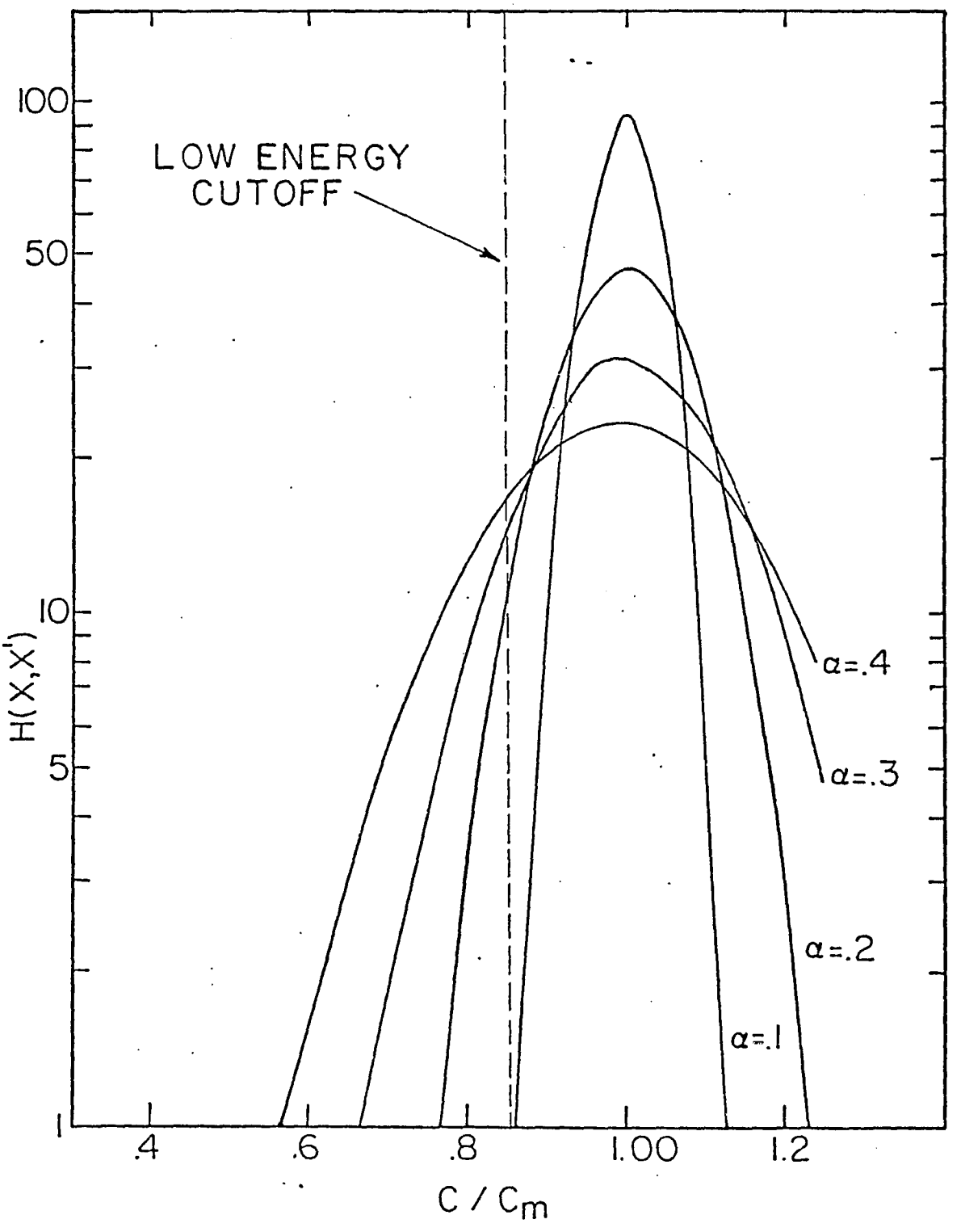

III.5 The resolution redistribution function (H(x, x') for different detector resolutions.

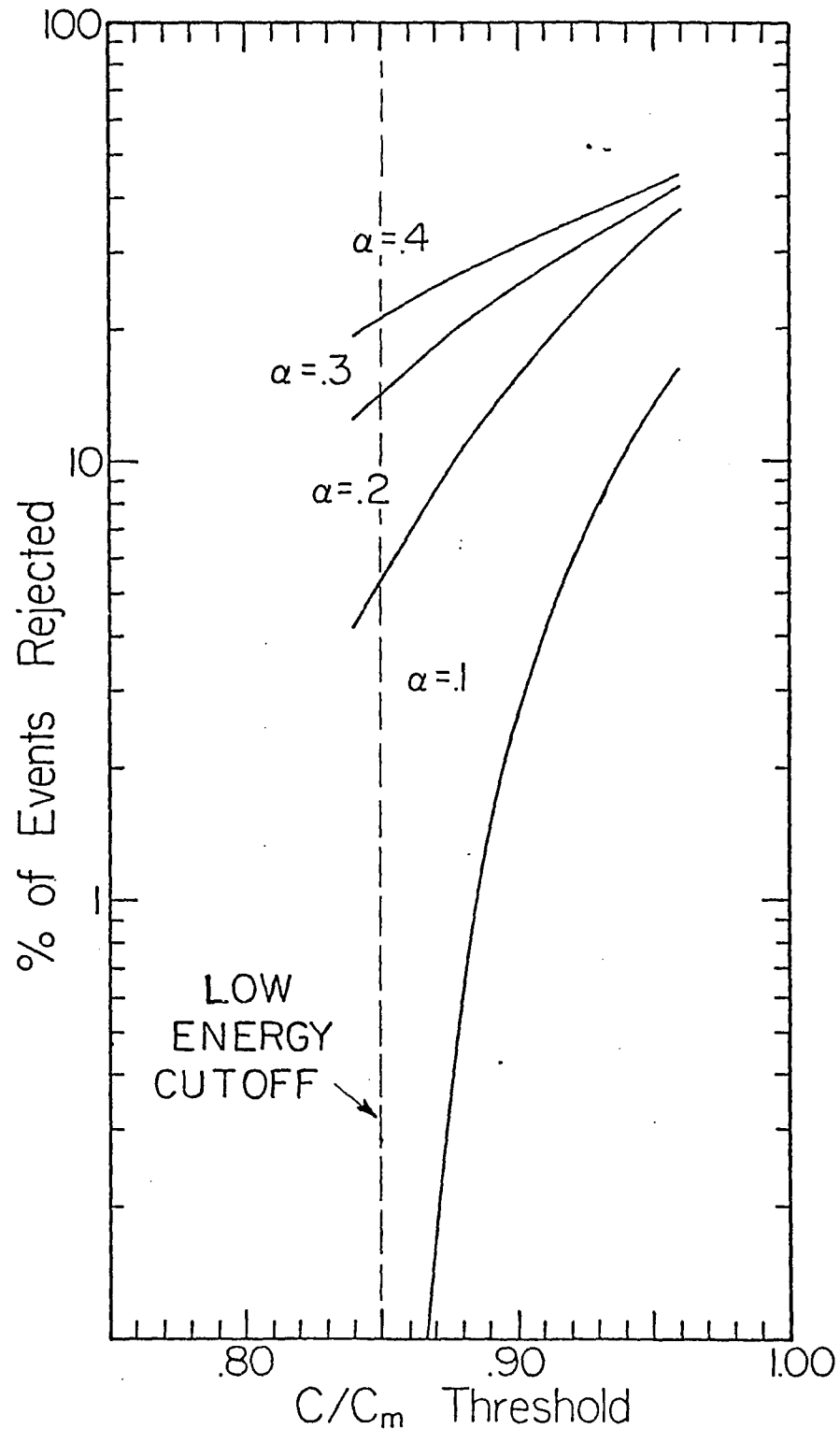

III.6 Rejection of valid events vs. solid Cerenkov criteria

and 3) residual scintillation light in the Freon-12 gas. This, coupled with the statistical variances associated with real detector systems, produces a significant population of events that "spill over" into the high energy bins. By removing as many of these low energy events as possible, one can significantly reduce the background contamination of the high energy particle population. Figure III.4 shows the ideal crossplots of the solid Cerenkov detector pulse height versus the scintillator pulse height for a single charge species. The outputs of the scintillator and the solid Cerenkov counters reach their asymptotic value above a few GeV and ideally the high energy events will lie in this asympotic region. One can place criteria on the S X C matrix that excludes events below ~.85 C/Cm (~ 1.4 GeV/nuc) from the high energy analysis. This same criteria is capable of removing valid high energy events that spill over into the low energy domain. How many of the high energy events will be removed by this criteria as a result of resolution broadening?

As discussed in Chapter IV-3, the redistribution function that describes this spreading of events in Cerenkov space is

$$3.5) \quad H(x,x') = \frac{1}{\sigma\sqrt{2\pi}} \exp\left[-1/2\left(\frac{x-x'}{\sigma}\right)^2\right]\left\{\left[1-\frac{\beta_o^2}{1-\delta x}\right]^{-\frac{3}{2}}\cdot(1-x)^{-2}\right\}$$

Figure III.5 shows the expected distributions of the high

energy events as a function of C/Cm for various resolutions of the solid Cerenkov detector. Numerical calculations have been carried out that show the expected percentage of valid high energy events that will be rejected as a function of C/Cm for different values of the detector resolution. This has been plotted in Figure III.6. Criteria was placed on the pulse heights of the scintillators and solid Cerenkov detectors such that less than .5% of the expected high energy events were excluded.

III-5) Consistency Requirements - G1 X G2

The gas Cerenkov detector contains two banks of photomultiplier tubes, thus providing two independent measurements of the same event. This provides us with a tool that enables us to separate the two major causes of resolution broadening. By plotting the pulse height of one bank versus that of the other bank, fluctuations in the signal due to differences in trajectory (ie. pathlength variations) will be correlated in both banks. However, statistical fluctuations in the photoelectron production in general will not be correlated. Criteria can then be imposed on the two banks of the detector such that events that lie outside a specified range of standard deviations can be excluded from analysis. Since the fluctuations are expected to be proportional to the square root of the total

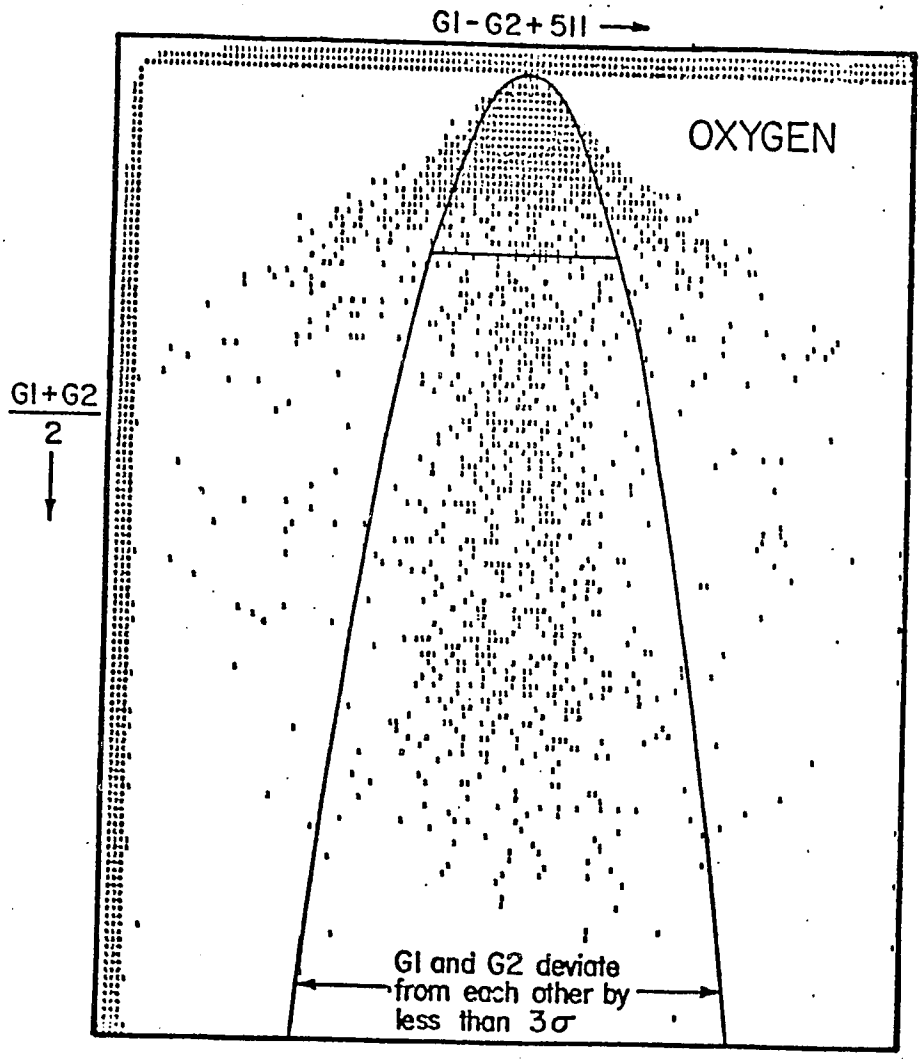

III.7 Matrix of the gas Cerenkov dtector pulse heights G11 vs. G22

signal, a criterion of the form

$$3.6) \quad \frac{|G11 - G22|}{\sqrt{G11+G22}} < k$$

was applied as shown in Figure III.7 . As discussed in Section III-3, k was systematically varied to investigate the effects that this criteria had on the removal of background events as well as the effects on valid high energy events. k was varied such that events with a 15 sigma down to one sigma deviations were allowed. From this investigation, k was selected such that the variances less than three standard deviations were allowed. As one demands a tighter consistency between the two pulse heights, a certain percentage of valid events will be excluded from analysis. Criteria were placed on the banks of the gas detector such that 4.0% of the 1976 high energy events were removed, and 11.2% of the 1977 events and 23.5% of the 1977 and 1978 high energy events were removed from analysis due to excessive background contanimantion. Tighter criteria were applied on the sucessive flights in an attempt to remove the increased background caused by the residual scintillation effects and increased pathlength variations.

III-6) Charge Determination

At energies at or above the gas Cerenkov thresholds, the scintillator and the solid Cerenkov detector have reached their asymptotic value. Crossplots of C+S/2 versus G11+G22 /2 effectively plots the charge versus energy since changes in the C+S/2 dimension are essentially energy independent and vary only as a function of Z . Figure III.8 shows a matrix of C+S/2 versus G for the 1976 flight. The centroids of the distributions in the C+S/2 dimension that lie above the "below threshold" event peak were determined and plotted in Figure III.9 for the three flights as a function of Z. The obvious deviation from a Z dependence is due to the scintillator inefficiency in the conversion of ionization energy loss into detectable light. The saturation effects have been discussed by Birks (1967). Figures III.10, III.11, and III.12 show the charge histograms for events above the usable Cerenkov threshold for each flight. The sigma charge resolution for the three flights for Oxygen was ~ .21 charge units.

The charge resolution was sufficient such that no charge overlap factors were needed except for charges 9, 11, and 13. The correction factors were derived from estimates of events that spill over into the adjacent charge bands by resolution broadening from the heavier populated charge

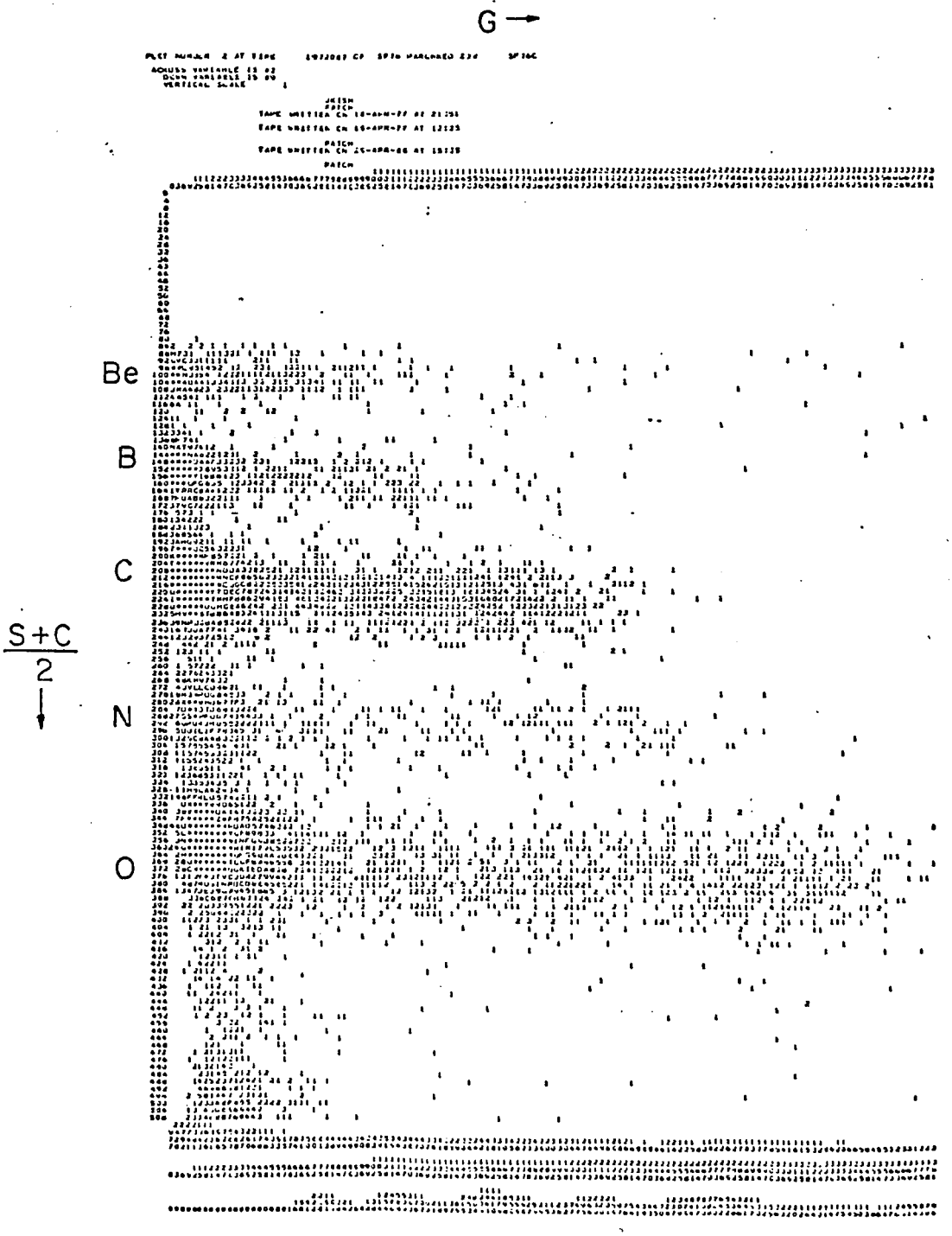

III.8 Matrix of the charge vs. energy ((C+S)/2 vs. G)

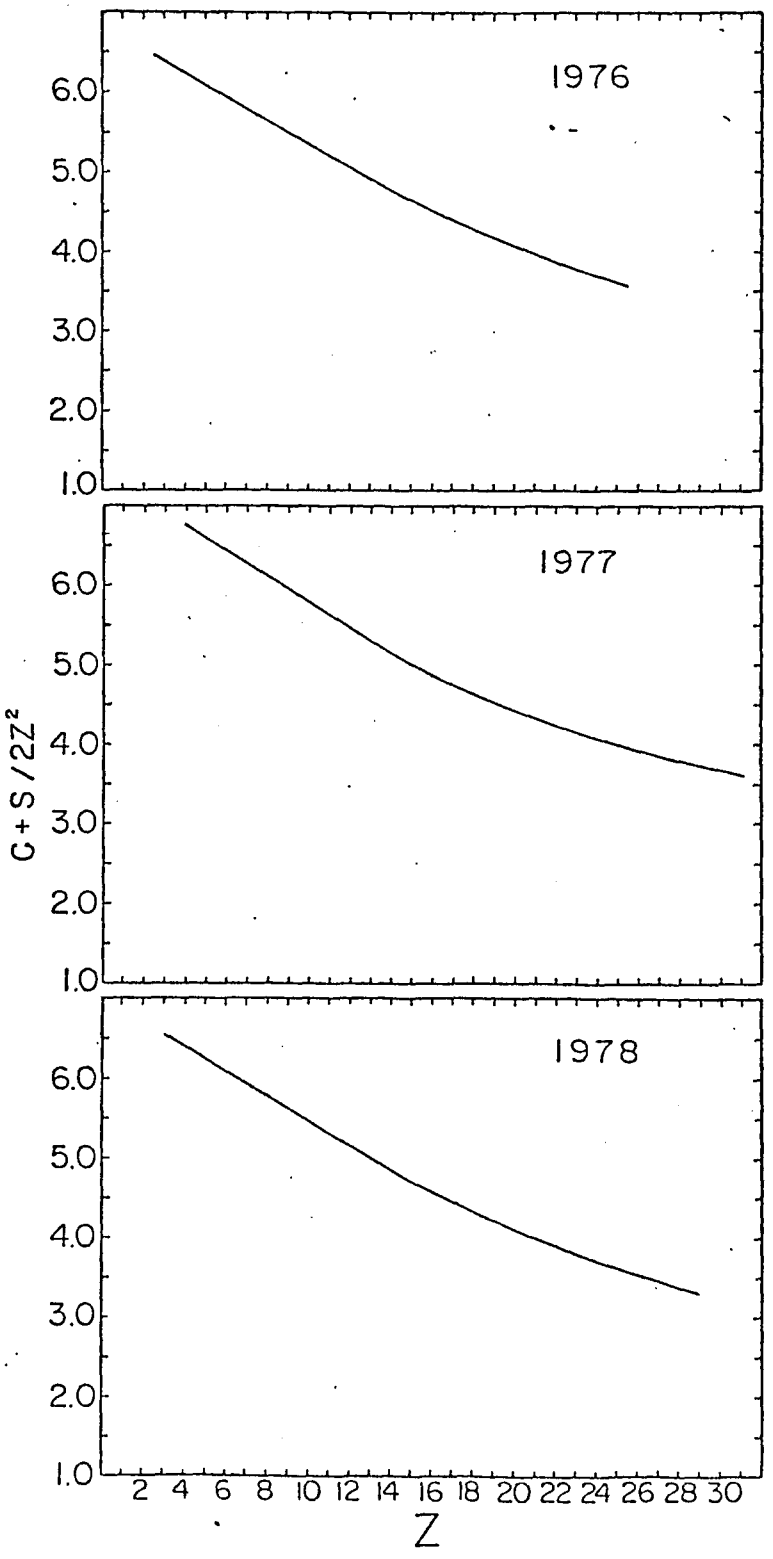

III.9 Measured saturation in the charge scale for 1976, 1977 and 1978 (ie. (C+S)/2z vs. Z)

groups. These estimates were derived by using a Gaussian fit to the charge distributions to determine the overlap for each charge. The correction factors for these odd charges resulted in reductions of the flux of 16% to each of the three charges in 1978, 9% in 1977, and 0% in 1976. The sparsely populated charge groups 9+11+13, 17-19, and 21-24 were grouped together in order to increase their statistics for data analysis.

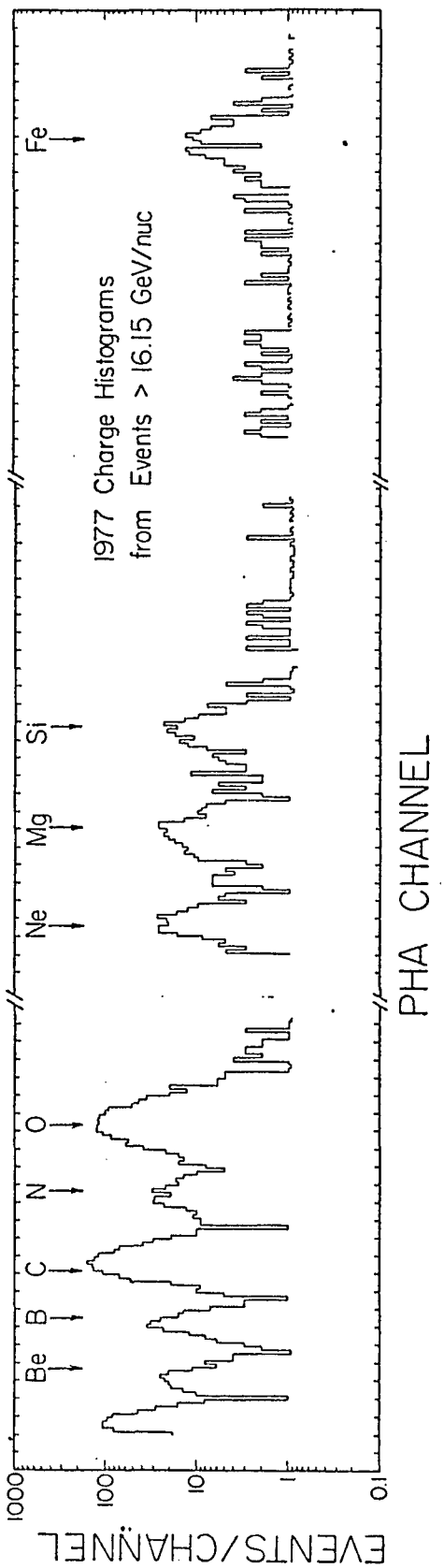

III.11 1977 charge resolution histograms

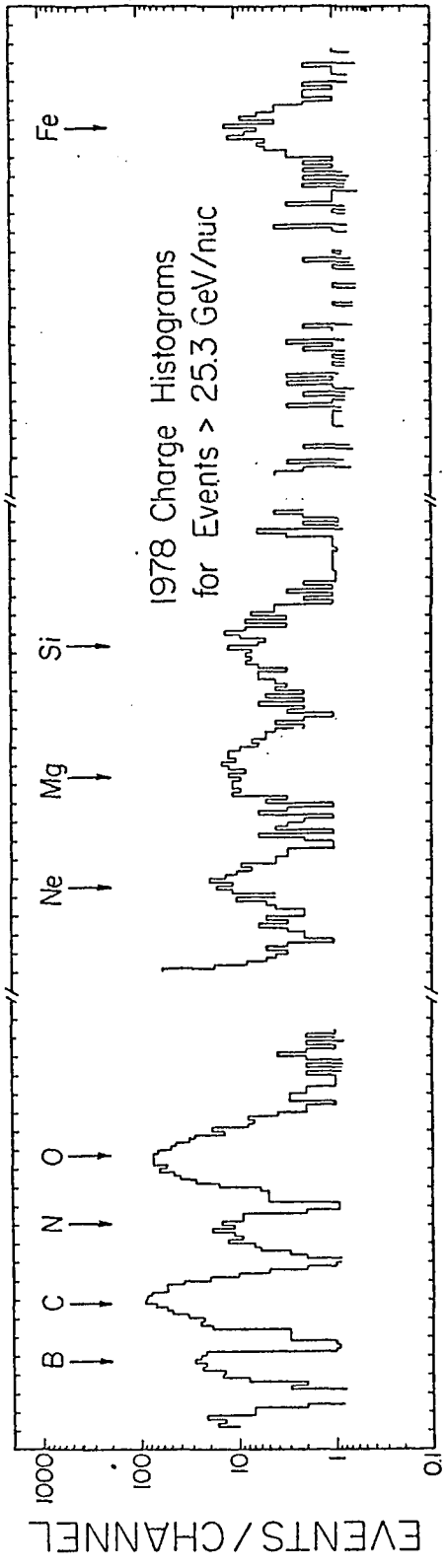

III.12 1978 charge resolution histograms

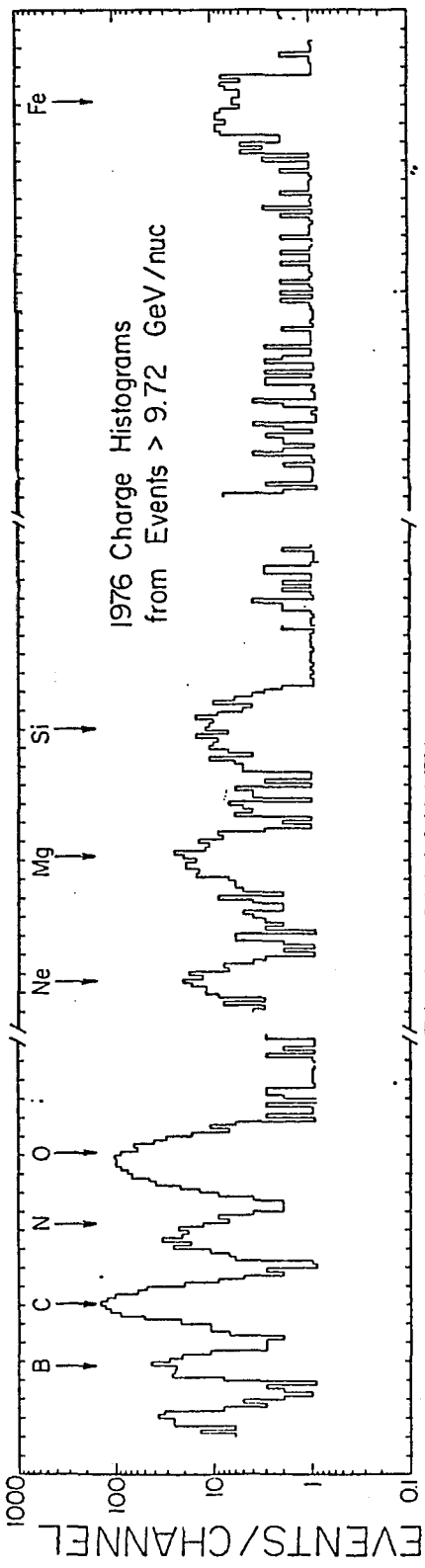

III.10 1976 charge resolution histograms

CHAPTER IV

ENERGY ANALYSIS

We begin this chapter with a discussion of the expected distributions of events in the Cerenkov (energy) dimension. This is followed by a derivation of the actual distribution of expected events in a real detector system that involves finite resolutions. Section IV-4 discusses the various methods used to determine the resolution of the gas detector. Sections IV-5 and IV-6 are involved with the assignment of the energy scales and other factors that influence the accuracy of these scales.

IV-1) Ideal Cerenkov Distributions

The (C+S)/2 by G matrices discussed in the last chapter form the basis for determining the particles energy spectra. Since the data is expressed in terms of a Cerenkov pulse height distribution, it is convenient to have a change of variables such that the intensity variable J is defined in terms of a ratio of Cerenkov pulse heights, G/Gm, where G is the observed pulse height and Gm is the expected pulse height for relativistic $\beta = 1$ events.

The intergral flux J as a function of energy is defined by

$$4.1) \qquad J(\Delta E) = \int_{E_2}^{E_1} j(E)dE$$

where E is the kinetic energy, j(E) is the differential flux (#/Gev-sec-str-m**2) and J has dimensions of #/sec-str-m**2. It is assumed that j(E) can be expressed in terms of a power law , $E^{-\gamma}$, where γ is the spectral index. The transformed integral becomes

$$4.2) \qquad J(\Delta x) = \int_{x_1}^{x_2} j(x)\frac{dE}{dx}dx \qquad ; x = \frac{G}{Gm}$$

The light from a Cerenkov detector can be expressed by the relationship

$$4.3) \qquad G = kZ^2(1 - \frac{1}{n^2\beta^2})$$

Where n is the index of refraction, $\beta = v/c$, Z is the charge of the incident particle, and k is a constant. The gas pulse height G may be expressed in terms of the $\beta = 1$ pulse height, Gm.

$$4.4) \qquad x = (1 - \beta_o^2/\beta^2) / (1 - \beta_o^2) \qquad ; \beta_o^2 = 1/n^2$$

By inverting this equation and solving for β , one obtains an expression for β as a function of G/Gm.

$$4.5) \qquad \beta^2 = \left[\frac{\beta_o^2}{1 - \delta x}\right] \qquad ; \delta = (1 - \beta_o^2)$$

Then

$$4.6) \qquad E = (\gamma - 1)E_o = \left[\left\{(1 - \beta_o^2) / (1 - \delta x)\right\}^{-1/2} - 1\right]E_o$$

$$4.7) \qquad \frac{dE}{dx} = \frac{\delta \beta_o^2 E_o}{2}\left[\left\{1 - \beta_o^2/(1 - \delta x)\right\}^{-3/2}(1 - \delta x)^{-2}\right]$$

Placing Equations 4.7 and 4.6 into Equation 4.2, yields

$$4.8) \qquad J(\Delta x) = C\int_{x_1}^{x_2}\left[\left\{\left[(1-\beta^2)/(1-\delta x)\right]^{-1/2}-1\right\}\left\{\left[(1-\beta^2)/(1-\delta x)\right]^{-3/2}(1-\delta x)^{-2}\right\}\right]dx$$

One can continue and solve for the differential flux j(x').

$$4.9) \qquad j(x) = \frac{dJ(\Delta x)}{dx} = C\left[\left\{\left[(1-\beta^2)/(1-\delta x)\right]^{-1/2}-1\right\}\left\{\left[(1-\beta^2)/(1-\delta x)\right]^{-3/2}(1-\delta x)^{-2}\right\}\right]$$

Figure IV.1 is a plot of j(x') vs x' for various spectral indices. This figure represents the distribution of events that one would expect for an ideal detector as a function of the Cerenkov pulse height.

It should be noted that for energies above ~ 50.Gev the expression for the differential flux can be simplified by making the approximation that E~P in Equation 4.6. This leads to an expression for the differential flux of

$$4.10) \qquad j(x) \cong K(1-x)^{\frac{\gamma-3}{2}}$$

The differential flux from this expression is plotted in Figure IV.2 . Substantial error can occur in deriving the energy spectra when using this approximation in the inapproprate energy domain.

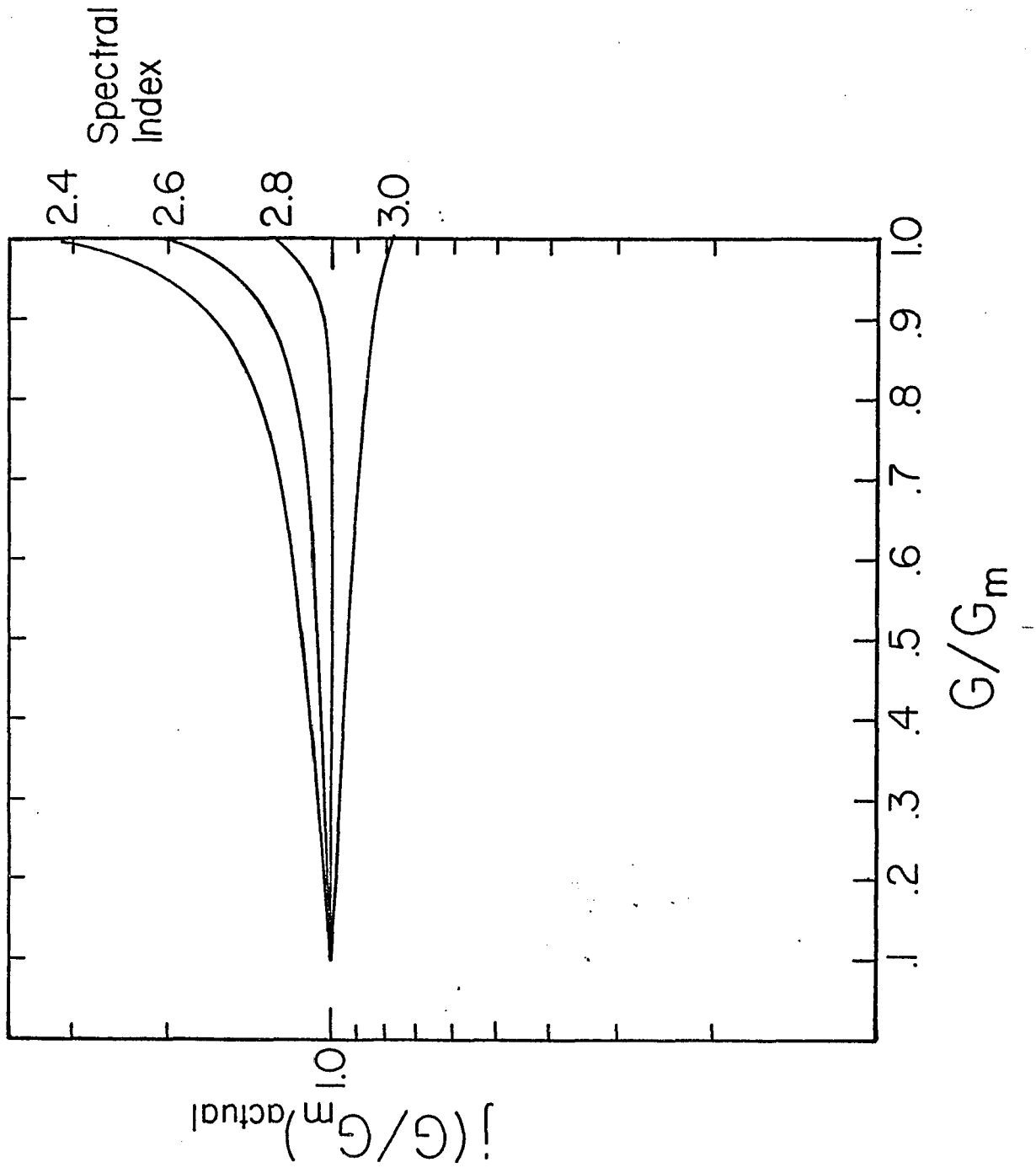

IV.1 Ideal distribution of events as a function of the Cerenkov pulse heights

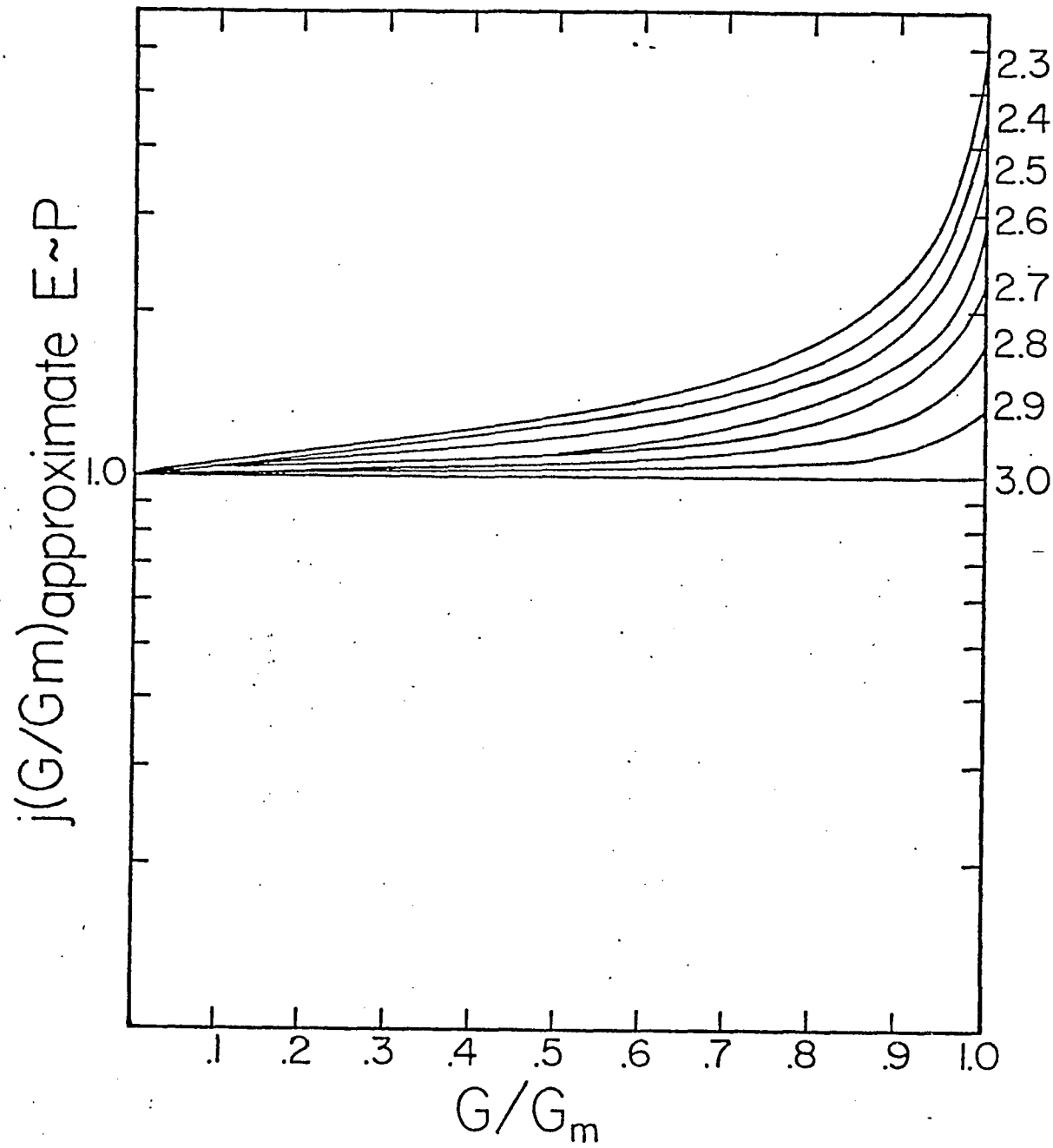

IV.2 Approximate distribution of events as a function of the Cerenkov pulse height (P~E)

IV-2) Instrument Response

For an ideal detector Equation 4.8 would describe the distribution of events in the Cerenkov dimension: however, due to statistical fluctuations in the energy loss process, the spectrum that one observes is a convolution of the actual spectrum with the instrument response. In order to determine the actual energy spectrum one must consider the convolution-deconvolution process, instrument resolution functions (photoelectron statistics), and any extraneous contributions to the Cerenkov signal (i.e. other scintillation or Cerenkov effects and pathlength variations). From the parameters extracted from the data one must account for these effects and apply correction factors that will yield the actual energy spectrum.

IV-3) Deconvolution Process

The techniques described in this section are similar to those described by J.A. Lezniak (1975). For a monoenergetic beam of particles passing through a real detector, one would observe a spreading or broadening of the energy distribution. One begins with the assumption that in Cerenkov detectors with sufficient production of photoelectrons, the spreading function may be described by a Gaussian redistribution function F(x,x').

$$4.11) \qquad F(x,x') = \frac{1}{\sigma\sqrt{2\pi}} \exp\left[-1/2 \frac{(x - x')}{\sigma^2}\right]$$

Where x' is the incident Cerenkov ratio G/Gm, x is the redistributed value of G/Gm, and σ is the standard deviation which is proportional to the number of photoelectrons produced. The problem is further compounded by the fact that the spectrum is not monoenergetic but a continuous input energy spectrum whose sigma is a function of the particle energy.

One can modify Equation 4.2 to include the redistribution function F(x, x'). Equation 4.2 becomes

$$4.12) \qquad J_{inst}(\Delta x) = \int_{x_1}^{x_2} F(x,x') \cdot j_{act}(x') \cdot \frac{dE}{dx'}\, dx'$$

Where Jinst is the intergral flux as measured by the instrument. F(x, x') must also meet the normalization requirement that

$$4.13) \qquad \int F(x,x')dx' = 1$$

Then the differential flux observed by the instrument becomes

$$4.14) \qquad j_{inst}(x') = \frac{dJ_{inst}}{dx} = \frac{C}{\sigma\sqrt{2\pi}} \exp\left[-1/2\left(\frac{x-x'}{\sigma}\right)^2\right]\left\{\left[1-\frac{\beta_o^2}{1-\delta x'}\right]^{-1/2}-1\right\}^{-\gamma}\cdot\left\{\left[1-\frac{\beta_o^2}{1-\delta x'}\right]\right\}^{-3/2}(1-\delta x')^{-2}$$

Let

$$4.15) \qquad H(x,x') = \frac{C}{\sigma\sqrt{2\pi}} \exp\left[-1/2\,\frac{(x-x')^2}{\sigma}\right]$$

Figure IV.3 is a plot of H(x, x') vs x' for various values of x. H(x, x') represents a weighting function for the

differential kinetic energy spectrum in the transformed integral expression.

Figures IV.4 through IV.6 show the expected instrument response for several differential kinetic energy input spectrum vs PHA channel. These plots show that for most spectra, the resolution of the detector is such that the observed spectra tracks the actual spectra up to .7 to .9 G/Gm. Past this point there is a noticeable non-symmetric feeding of events into other channels due to the resolution redistribution function.

To correct the observed flux back to the actual flux an average correction factor for a given energy bin is determined by taking the average ratio of (j-act./j-inst) over the energy interval. Figure IV.7 shows these correction factors for different input spectra and gas detector resolutions. Tables IV.1 through IV.3 show the average correction factors when summed over finite energy range and their associated errors for the three flights. The integral correction factors shown in Figure IV.8 is derived in the same manner.

In almost all cases it is clear that the correction factors are weakly dependent on the spectral index. The correction factors at the worst case vary by ~ 2.% for a spectral index varing from 2.4 to 2.8 . The integral and differential correction factors have been selected from a

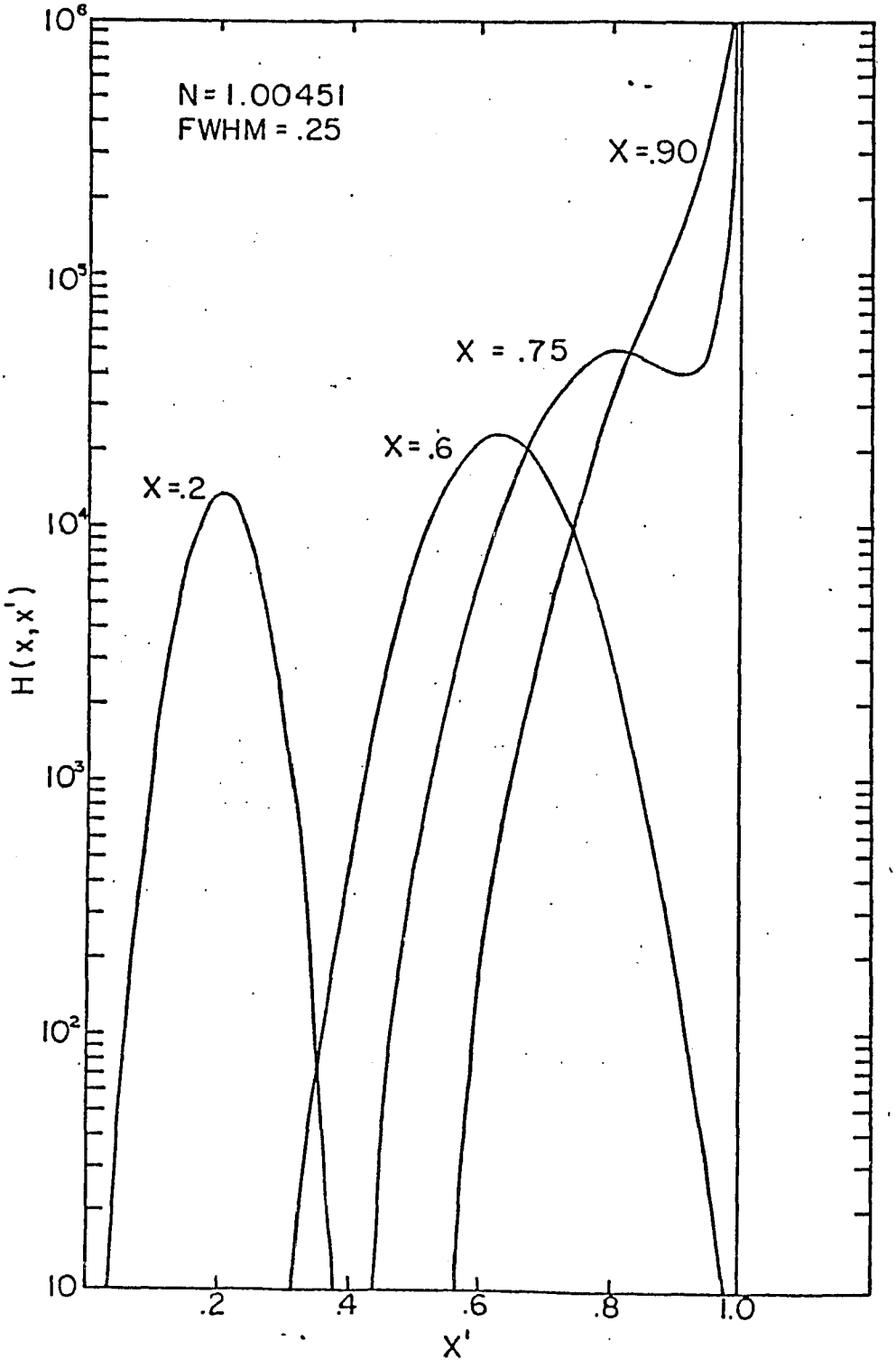

IV.3 The resolution redistribution function H(x, x') vs energy (x')

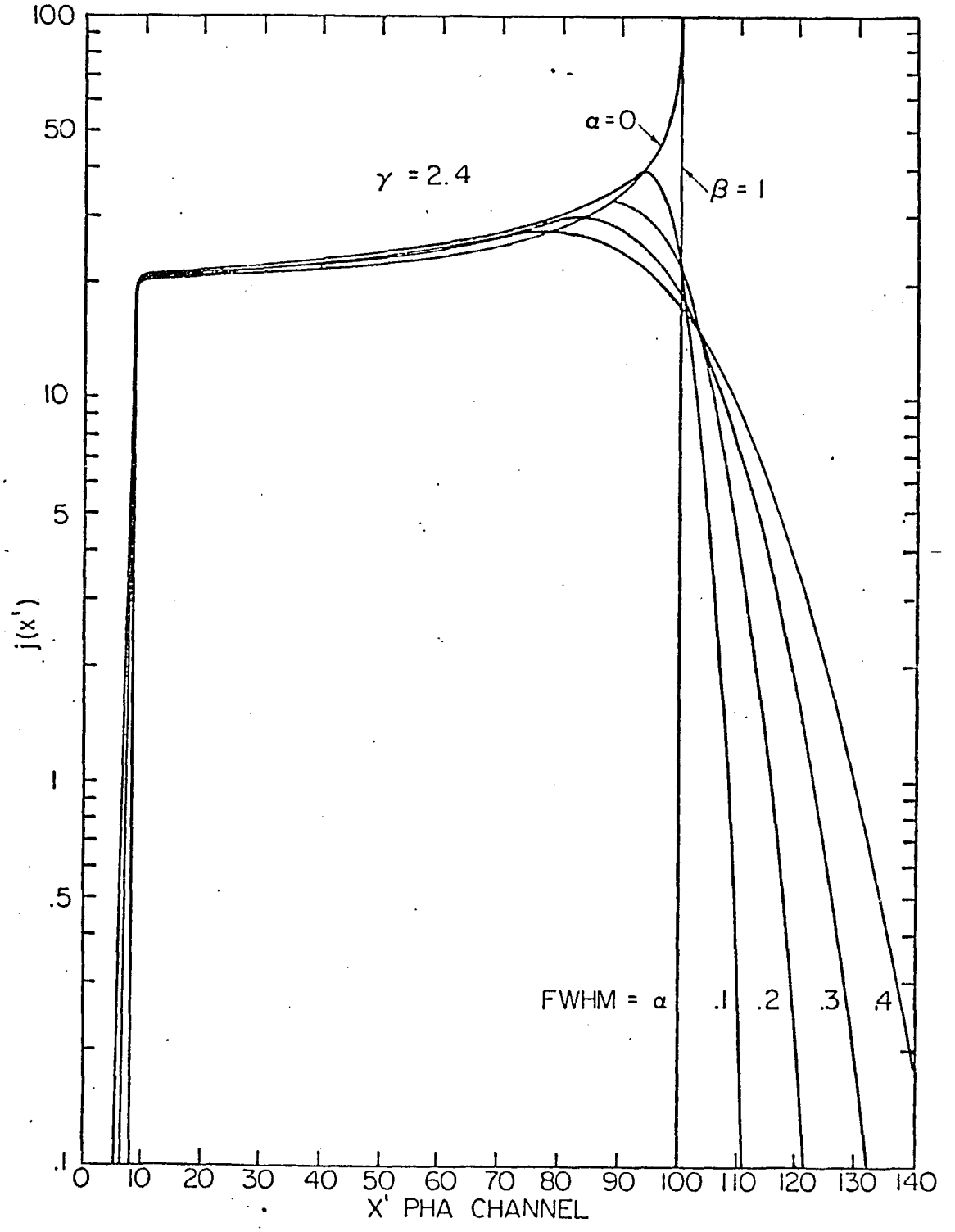

IV.4 The instrument response to the differential flux j(x) vs. x, with gamma = 2.6

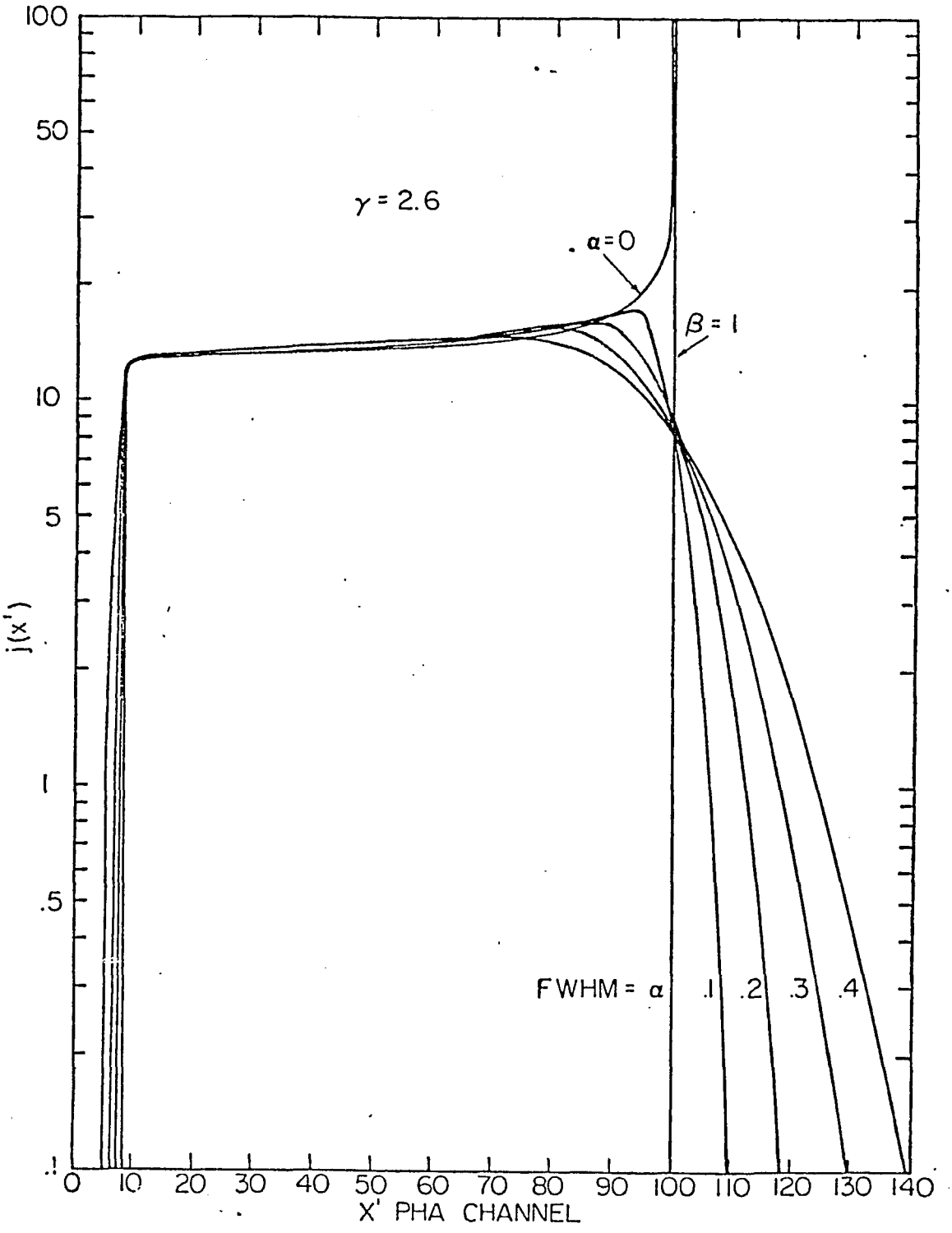

IV.5 The instrument response to the differential flux j(x) vs. x, with gamma = 2.7

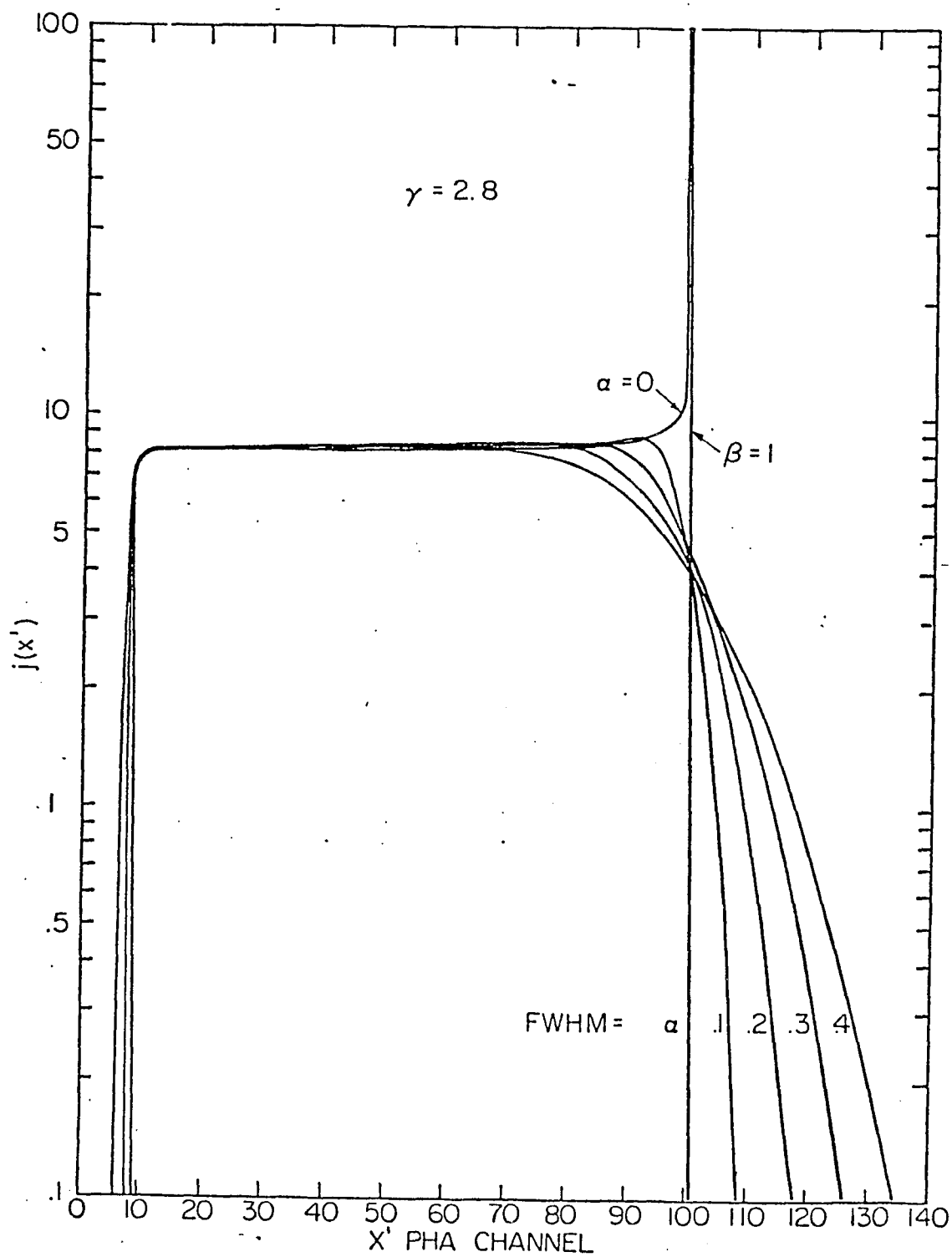

IV.6 The instrument response to the differential flux j(x) vs. x, with gamma =2.8

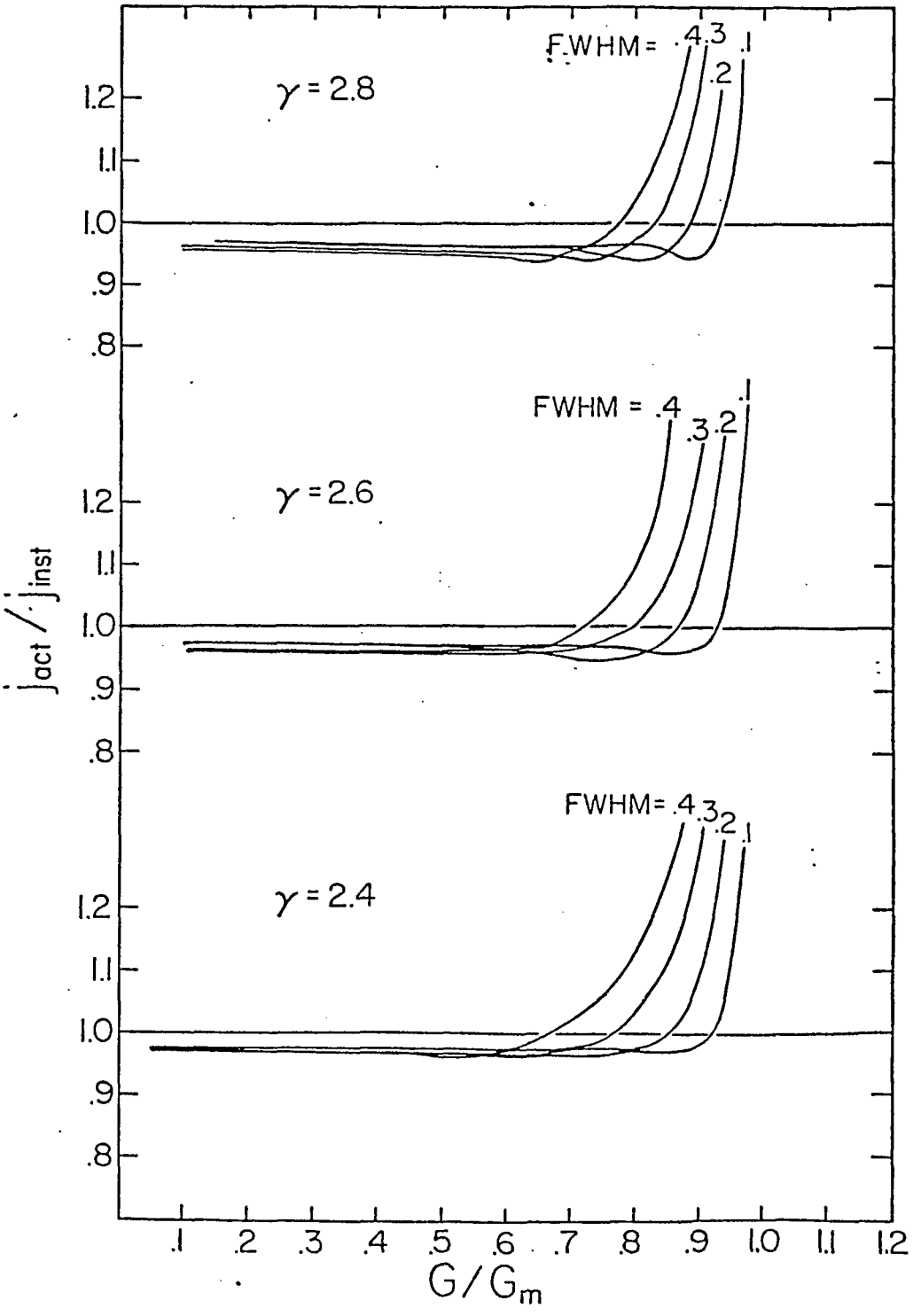

IV.7 The differential resolution correction factors j-act./ j-inst. vs. G/Gm

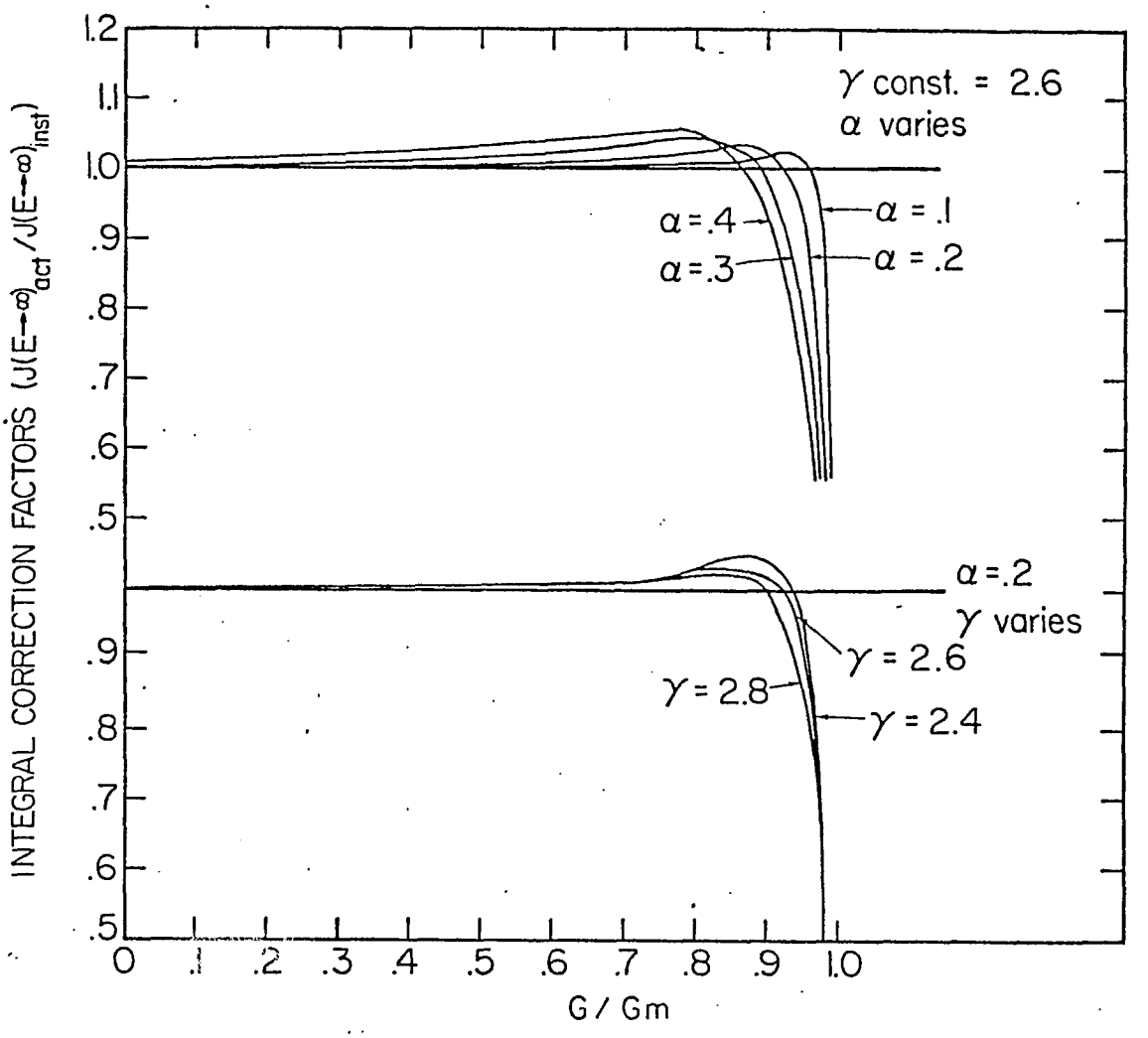

IV.8 The integral resolution correction factors J-act./ J-inst. vs. G/Gm

AVERAGE CORRECTION FACTORS - 1976 - j_{Act}/j_{Inst}

FWHM	0.20 - 0.40	0.40 - 0.56	0.56 - 0.70	0.70 - 0.82	0.82 - 0.90	0.90 - 0.95	$I_{>0.95}$
0.10	0.974	0.973	0.973	0.971	0.964	1.017 ± .055	1.022
0.15	0.970	0.969	0.968	0.964	0.969±.015	1.128 ± .098	0.976
0.20	0.969	0.968	0.966	0.958	1.005±.039	1.250 ± .121	0.917
0.25	0.968	0.967	0.962	0.963 ± .008	1.059±.060	1.362 ± .134	0.857
0.30	0.968	0.965	0.968	0.977 ± .019	1.122±.075	1.464 ± .141	0.802

ACTUAL CORRECTION FACTORS - 1977 - j_{Act}/j_{Inst}

FWHM	0.40 - 0.56	0.56 - 0.70	0.70 - 0.82	0.82 - 0.90	0.90 - 0.95	$J_{>0.95}$
0.10	0.979	0.978	0.976	0.970	1.013 ± 0.050	1.031
0.15	0.970	0.968	0.964	0.965 ± .012	1.113 ± 0.095	0.987
0.20	0.968	0.965	0.958	0.996 ± .036	1.231 ± 0.120	0.932
0.25	0.967	0.961	0.959 ± .006	1.046 ± .057	1.343 ± 0.207	0.875
0.30	0.964	0.957	0.970 ± .016	1.105 ± .073	1.444 ± 0.143	0.823
0.35	0.962	0.955	0.989 ± .029	1.167 ± .085	1.536 ± 0.148	0.776

AVERAGE CORRECTION FACTORS - 1978 - j_{Act}/j_{Inst}

FWHM	0.56 - 0.70	0.70 - 0.82	0.82 - 0.90	0.90 - 0.95	$f_{>}$ 0.95
0.10	0.985	0.984	0.977	1.012 ± 0.45	1.041
0.15	0.965	0.965	0.957	1.097 ± 0.91	0.996
0.20	0.966	0.958	0.984 ± .024	1.211 ± .118	0.954
0.25	0.963	0.954	1.032 ± .053	1.321 ± .133	0.892
0.30	0.958	0.956	1.088 ± .069	1.421 ± .142	0.841

spectral index of 2.6 in the following calculations.

From matrix distributions described in Chapter III-6 and Figure III.8, one obtains the distribution of events in the Cerenkov dimension for 0 as shown in Figures IV.12 through IV.14 . Inspection of these distributions show several evident features. Each distribution is characterized by a residual scintillation peak at low pulse heights where below threshold effects are the dominant contribution to the signal. As the pressure is reduced in successive flights, the contribution of the residual scintillation to the total signal becomes significant. Near the end of the distribution there is a slight peak or broad plateau followed by a sharp decrease in the number of events. This plateau (Gm-inst.) is related to the actual $\beta = 1$ point. Since the broad peak is not well defined in the distribution , it is not a suitable deconvolution parameter to use. A more consistent and well defined point which is used in the energy deconvolution process may be obtained by taking 1/2 of the average Gm-inst point. This point lies on the sharply decreasing tail of the distribution. The use of this feature will be discussed in Chapter IV-6.

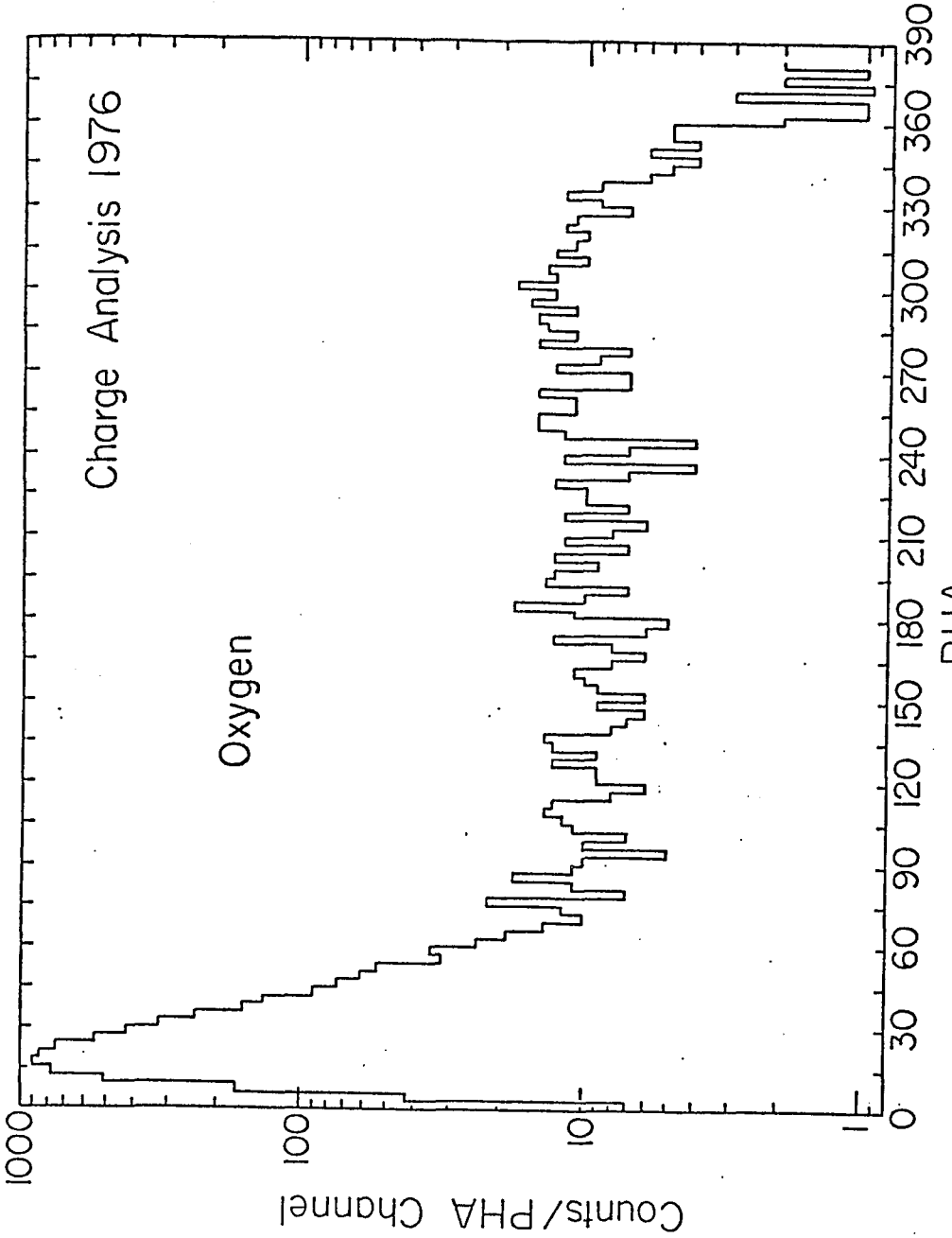

IV.12 1976 Cerenkov distributions for Oxygen

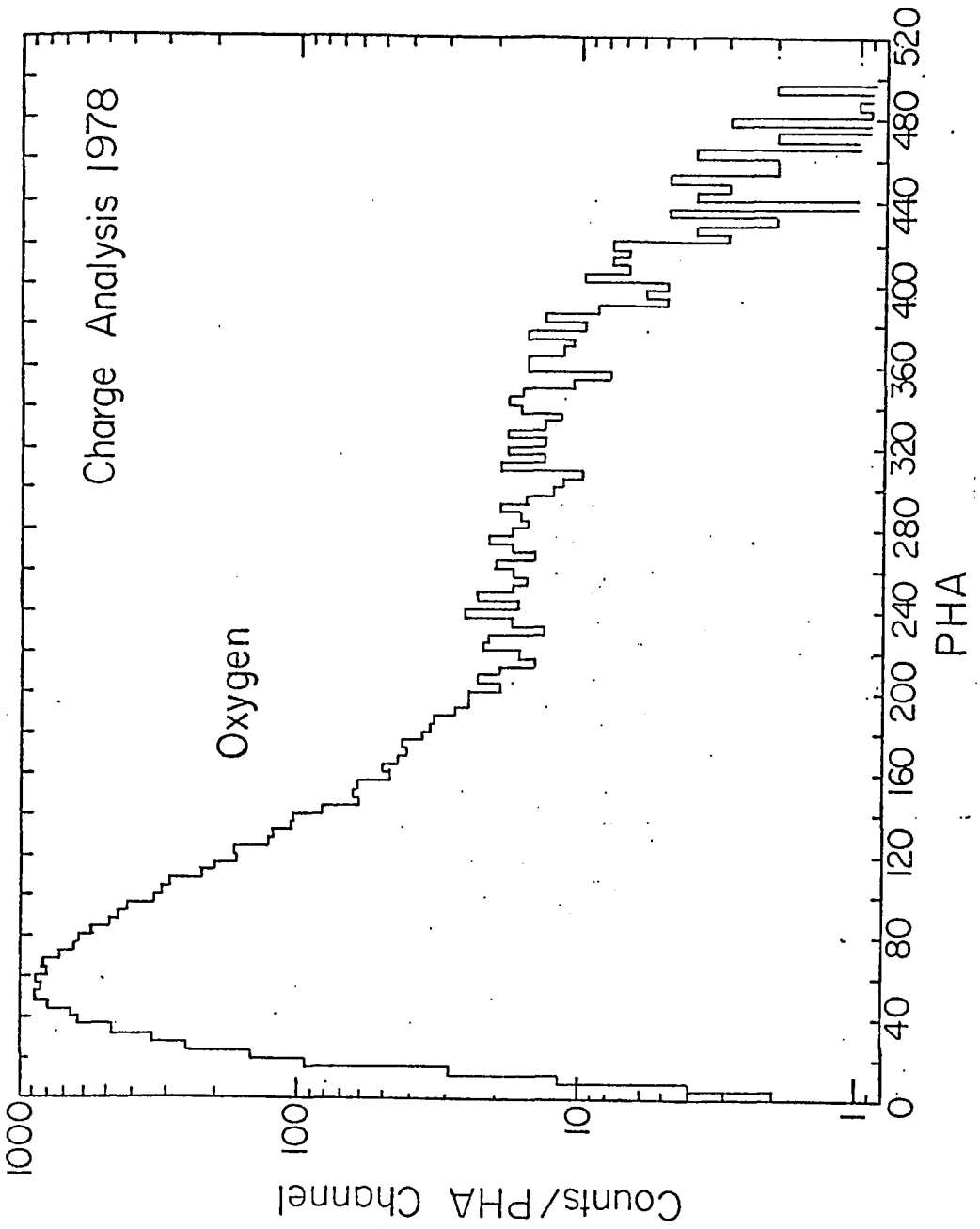

IV.14 1978 Cerenkov distributions for Oxygen

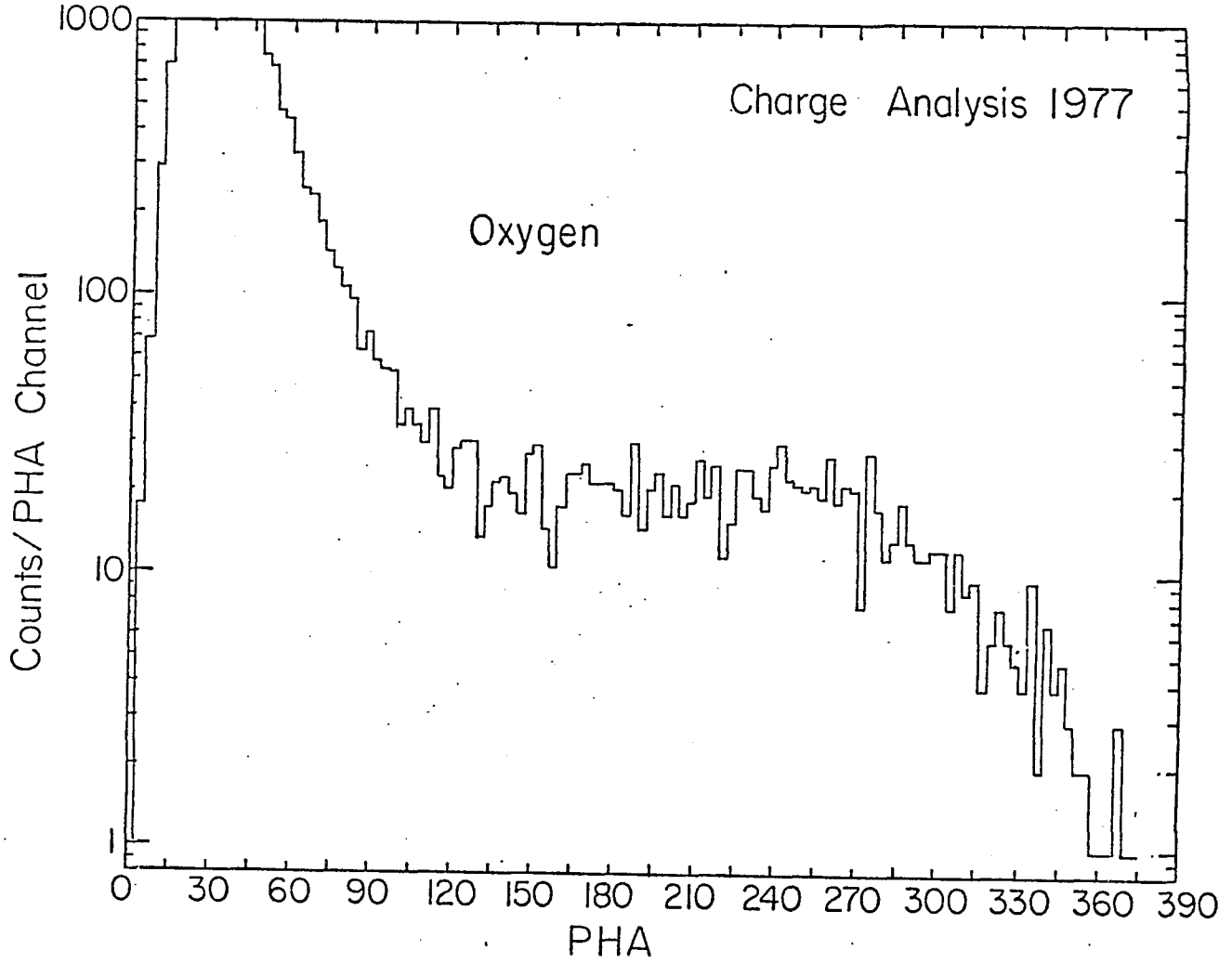

IV.13 - 1977 Cerenkov distributions for Oxygen

IV-4) Gas Counter Resolution

The gas signal is measured by two banks of photomultiplier tubes, which provide two independent measurements of the energy deposited. Associated with each measurement of G11 and G22 there will be corresponding standard deviations S-g11 and S-g22 respectively. A weighted average is used to determine the total resolution of the detector.

$$4.16) \qquad G = \frac{w_1 G11 + w_2 G22}{w_1 + w_2} = \frac{G11 + G22}{1 + w}$$

Where $w = w_1/w_2$ and w1, w2 are the respective weighting functions. The associated standard deviation in the average signal is

$$4.17) \qquad S_G = \left(\frac{S_{G11}{}^2 + S_{G22}{}^2}{(1+w)^2} \right)^{1/2}$$

S_{G11} and S_{G22} are the corresponding standard deviation of the pulse height in each bank. Since each bank is weighted equally $w = 1$, giving

$$4.18) \qquad S_G = \left(\frac{S_{G11}{}^2 + S_{G22}{}^2}{2^2} \right)^{1/2}$$

Figure III.7 shows a plot of G11-G22+offset vs. the average gas signal (G11+G22)/2 . The standard deviations and FWHM of the combined signal may now be expressed in terms of these modified matrices. Resolutions were measured for various values of the average gas pulse height (G11+G22)/2

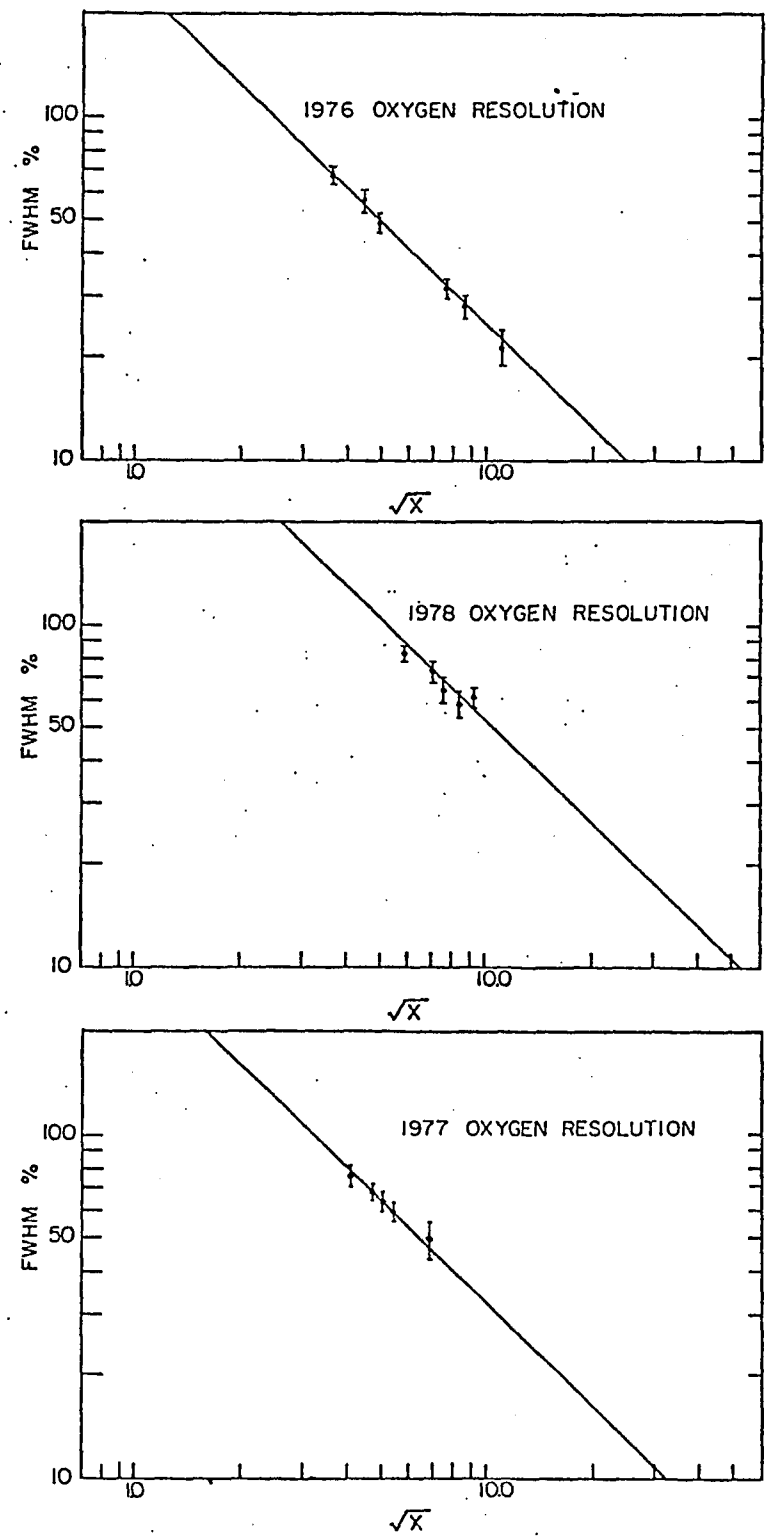

IV.9 1976, 1977 and 1978 gas counter resolutions

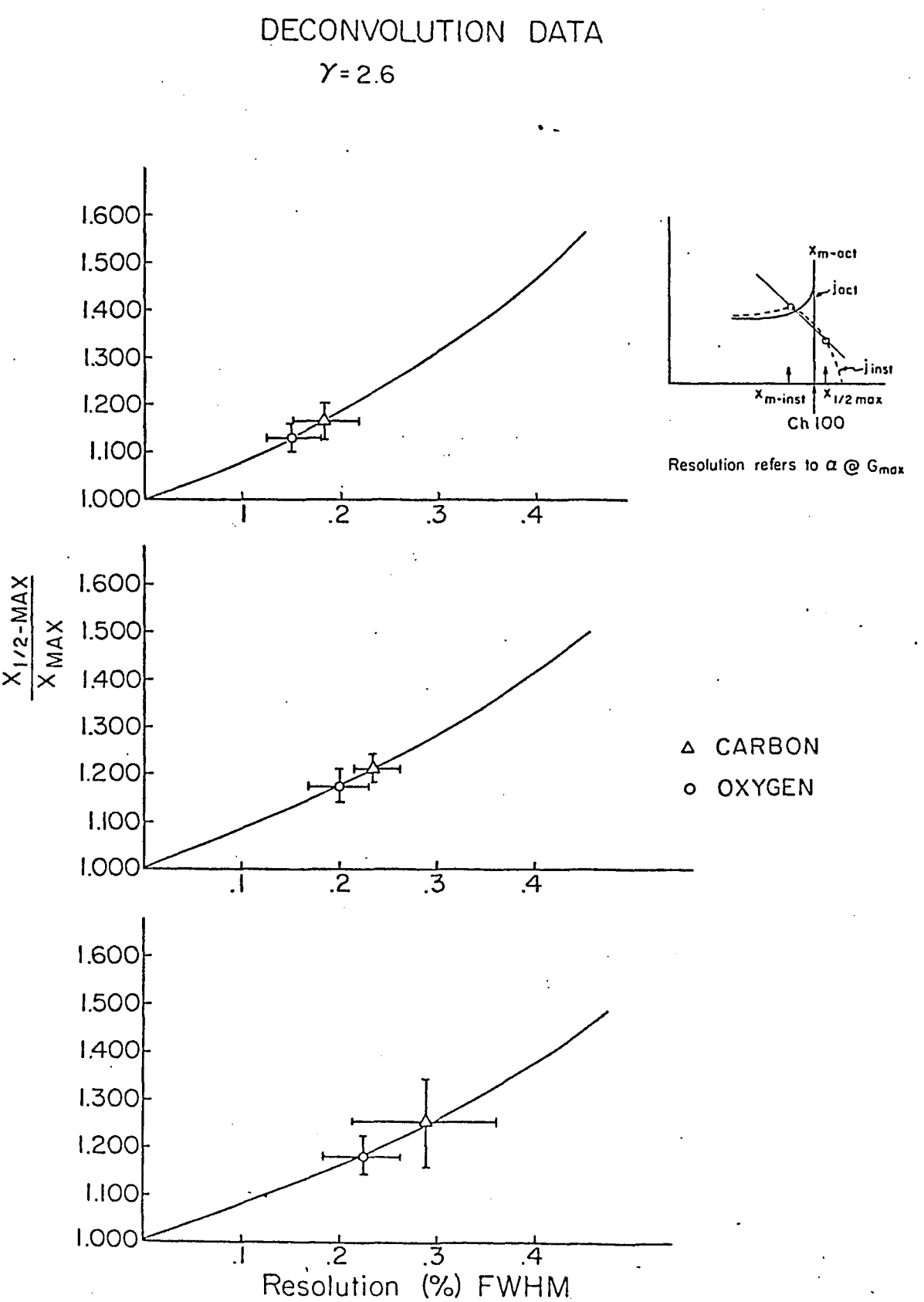

IV.10 1976, 1977 and 1978 deconvolution parameters (G-½)/G-act. vs. resolution

TABLE IV.4

RESOLUTION SUMMARY TABLE

Flight	Measured FWHM % $\beta = 1$	Deconvolution estimates Estimate	measured
1976	(108.8% ± 7.3)/Z	C 18.2% ± 3.4	18.1%
		O 15.0% ± 2.6	13.6%
1977	(147.9% ± 28.7)/Z	C 23.5% ± 2.6	24.6%
		O 20.0% ± 3.0	18.5%
1978	(212.0% ± 74.0)/Z	C 28.0% ± 7.6	35.0%
		O 25.0% ± 3.9	26.5%

and plotted in Figure IV.9. The results are tabulated in Table IV.4.

A second method was used to help verify the measured resolutions. By using deconvolution parameters defined in Section IV-2 , one observes that the ratio of G-1/2 / G-m inst vs. the resolution can be used on the abundant nuclei to provide limits on the resolutions as shown in Figure IV.10 with the measured ratios for C and O. These results are compared to the measured values shown in Table IV.4.

In summary, the resolutions were viewed by two techniques: 1) measured resolution of the combined signal and 2) using deconvolution data to set limits on the resolution of the abundant nuclei. Both of these methods yield consistent results. Table IV.4 lists the results and associated errors in determining the resolution of the gas detector.

IV-5) Other Contributions to the Cerenkov Signal

There exist other contributions to the primary radiation in the gas Cerenkov detector. These sources of added radiation are: 1) Cerenkov light produced by knock-on electrons that reach the photomultiplier tubes; 2) Cerenkov light produced in the $BaSO_4$ paint; and 3) residual scintillation of the Freon-12 gas. From cross plots of the

solid Cerenkov detector pulse height versus the pulse height of the gas detector, one observes the total "below gas threshold" contribution as a function of energy. The light production from knock-on electrons for this telescope has been calculated by Lezniak (1975) and is shown in Figure IV.11 . The absolute magnitudes of the scintillation (dE/dX) in the Freon 12 and the Cerenkov radiation from the BaSO paint were then used as adjustable parameters such that when all the contributing radiation affects were summed, they yielded the total effects observed in the solid Cerenkov versus gas matrices as shown in Figure IV.11 .

In sucessive years the absolute pressure in the gas Cerenkov detector was reduced to give different energy thresholds. This resulted in a reduction of the primary radiation emitted due to the reduced path length. This reduction of pressure affects the relative contribution of the knock on component, whereas the contribution of the Cerenkov radiation generated in the BaSO paint is unaffected. Table IV.5 summarizes the relative contribution of each component on the total observed signal (normalized to 1976).

The connection between the actual versus the measured G/Gm due to the added radiation components is given by

$$\frac{G'}{G_m'} = \frac{G/Gm + (\text{Residual scintillation comp.})}{1 + (\text{Residual scintillation comp.})} \qquad 4.19)$$

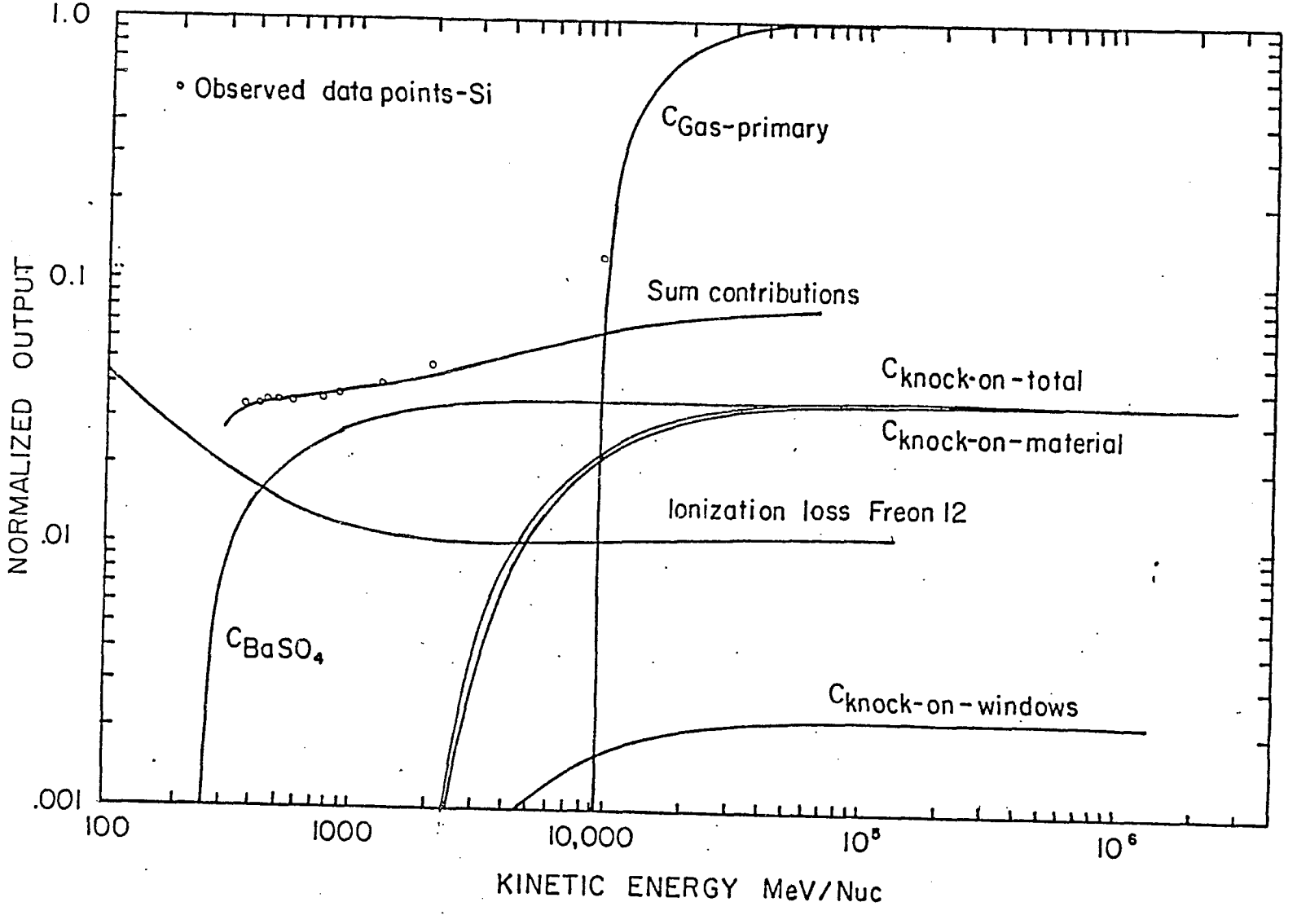

IV.11 Extraneous contributions to the gas Cerenkov signal

where G/Gm, G'/G'm is the measured and actual ratios respectively.

The following method was used to verify the effects and relative contribution of the residual scintillation on the resolution. The standard deviations for the three flights are proportional to the number of photoelectrons produced by the primary Cerenkov radiation (Np) as well as the photoelectrons produced by the scintillations (Ns) effects. Therefore:

$$4.20) \qquad \sigma(\%) \cong \frac{1}{\sqrt{N_p + N_s}}$$

Np should vary proportionally to the pressure whereas Ns should remain roughly a constant for the three flights.

From the measured resolutions, the number of photoelectrons was calculated by the relation:

$$4.21) \qquad N = \frac{1}{\sigma^2}\left(\frac{\delta_1}{\delta - 1}\right)$$

Where δ = the gain of the first dynode in the photomultiplier tube = 4. Normalizing the FWHM to the 1976 flight, one would expect to observe the following FWHM's to scale as shown in Table IV.4.

TABLE IV.5

Contributions to the Cerenkov signal

Year	Primary	Knock-on	$BaSO_4$	K.O.+$BaSO_4$	% of primary
1976	1.00	0.035	0.045	0.080	8.0%
1977	0.50	0.018	0.045	0.060	12.6%
1978	0.28	0.010	0.045	0.055	19.9%

IV-6) Assignment of Energy Scales

In order to define a consistent energy scale it is necessary to extract well defined parameters from the data and relate these quantities to the actual $\beta = 1$ point. Once Gmax-act has been accurately determined, one may then proceed to assign energy scales as a function of ratio of G/Gm as derived in Equations 4.5, 4.6, and 4.7.

$$E = (\gamma - 1)E_o = \left[\left\{(1-\beta_o^2)/(1-\delta x)\right\}^{-1/2} - 1\right]E_o \qquad (4.22)$$

This expression must be modified accordingly to account for the residual scintillation effects in determining the $\beta = 1$ point.

The problem is to relate 1/2 Gm-inst to the actual Gm as shown in Figure IV.11. The true Gm-act is then determined by Equation 4.22.

$$G_{m-act} = \left(\frac{G_{m-act}}{1/2\, G_{m-inst}}\right)\Bigg|_{\text{from deconvolution data}} \cdot (1/2\, G_{m-inst})\Big|_{\text{from distribution}} \qquad (4.23)$$

Once Gm-act has been determined, the energy scales may be assigned as a function of G/Gm as dictated in Equation .

The assignment of the energy scale is a function of the assignment of Gm. Figure IV.15 shows the expected error that result in an error in the placement of Gm. The lower energy assignments are relatively insensitive to errors in the placement of the $\beta = 1$ point. However, the higher

energies are exceedingly sensitive to the placement of Gm. Chapter V discusses consistency requirements that were made between the three flight data sets that shows inconsistencies in the energy scale assignments down to the 2% level.

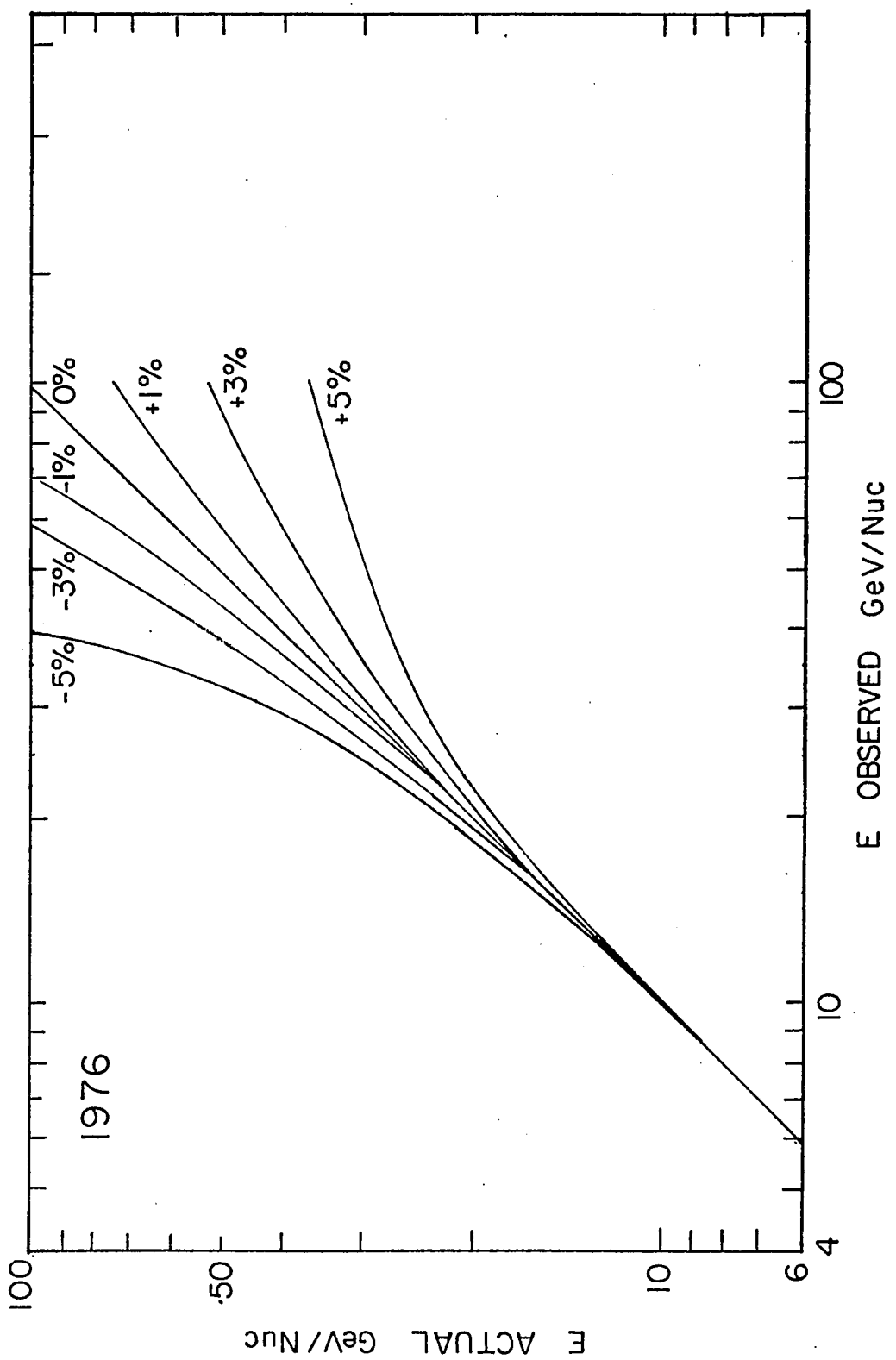

IV.15 Error in the energy scale due to an improper selection if Gm

CHAPTER V

RESULTS

V-1) Instrument and Atmospheric Correction Factors

After the proper energy scales have been assigned to the Cerenkov distributions, it is necessary to calculate the number of expected events incident at the top of the instrument. To do this, one must apply correction factors to the raw counts that take into account the events that have interacted in the telescope.

The number of surviving nuclei at the lower concidence element is a function of the amount of material in the telescope. A majority of the events that fragment in the telescope will be removed from analysis by the consistency requirements discussed in Chapter III-4,5,6. However, due to the inefficency in identifying and removing all of the fragmented particles, a detection and removal efficency factor of 80.% (± 5.%) was incorproated in the intensity calculations (i.e., 8 out of 10 of the fragmented events have been removed). The number of events incident at the top of the telescope is then determined by calculating and applying the appropriate interaction mean free paths for the material in the telescope.

5.1) $$\frac{N_i}{N_{obs}} = \left\{ e^{\frac{x}{\lambda}} + E\left(1 - e^{\frac{-x}{\lambda}}\right) \right\}^{-1}$$

where E= .20, the fraction of fragmented events that were not detected and removed by the consistency criteria

x= the amount of material in the telescope

λ = the weighted interaction mean free path

Ni=the number of nuclei incident to the telescope

Nobs=the number of surviving nuclei

The vertical thickness of each of the curved detectors was multiplied by a path length correction factor of 1.04 which corresponds to an average acceptance angle in the telescope of ~ 18 degrees from the zenith.

The atmospheric correction factors were determined by the use of a one dimensional atmospheric slab model which corrects for the depletion of the incident nuclei and the build up of secondaries in the atmosphere. The model makes use of target factors and cross sections discussed by Lindstrom et al. (1975) and Silberberg and Tsao (1977) to calculate the nucleus-nucleus cross sections. The uncertainty in the derivation of the fragmentation cross sections are inherently on the order of 10-15%. A zenith correction factor of 1.06 was multiplied times the vertical atmospheric depth to give the average slant atmospheric depths of 4.03, 3.50, and 4.51 gm/cm^2 for the respective flights.

The instrument and atmospheric correction factors for the three flights are listed in Table V.1.

V-2) Calculations of the Differential Intensities

After computing the corrected raw counts for each energy interval, calculations of the differential intensities were determined from the data by the following relationship:

$$5.2) \qquad j(E_m) \cong \frac{J(\Delta E)}{\Delta E}$$

where Em is defined to be the mean energy between the upper and lower edges of the energy interval, ΔE is the width of the interval in GeV and $J(E \to \infty)$ represents the corrected raw counts divided by the collection factor $(A\,\Omega\,t)$.

On the one hand, one would like to have the advantage of a large ΔE energy width which gives an increase in the number of counts and thereby improves statistics. On the other hand, if one has too large an energy width, the differential approximation in Equation 5.2 breaks down. In order to understand the errors involved in this approximation, the exact differential flux was calculated from an assumed power law spectrum and then compared to the results that the differential approximation would yield. Figure V.1 shows a graph of $\Delta E/E$ versus

TABLE V.1

INSTRUMENT AND ATMOSPHERIC CORRECTION FACTORS

	1975		1977		1978	
Z	inst.	atm.	inst.	atm.	inst.	atm.
5	1.460	1.023	1.416	1.020	1.216	1.027
6	1.480	1.130	1.434	1.112	1.225	1.155
7	1.508	1.065	1.458	1.056	1.236	1.077
8	1.533	1.162	1.480	1.139	1.247	1.193
9	1.092	1.022	1.084	1.104	1.047	1.108
10	1.593	1.141	1.534	1.121	1.272	1.167
11	1.627	1.093	1.564	1.080	1.286	1.110
12	1.654	1.189	1.588	1.162	1.297	1.225
13	1.678	1.104	1.610	1.090	1.307	1.124
14	1.706	1.198	1.634	1.107	1.318	1.237
16	1.760	1.184	1.681	1.158	1.339	1.220
17	1.787	1.058	1.705	1.050	1.350	1.068
18	1.816	1.116	1.730	1.100	1.361	1.138
19	1.847	1.116	1.757	1.100	1.373	1.138
20	1.880	1.175	1.786	1.150	1.386	1.208
21	1.916	1.081	1.817	1.070	1.399	1.096
22	1.954	1.093	1.850	1.080	1.414	1.110
23	1.996	1.069	1.887	1.060	1.429	1.082
24	2.030	1.151	1.916	1.130	1.442	1.180
25	2.092	1.151	1.970	1.130	1.464	1.180
26	2.119	1.320	2.017	1.273	1.474	1.387

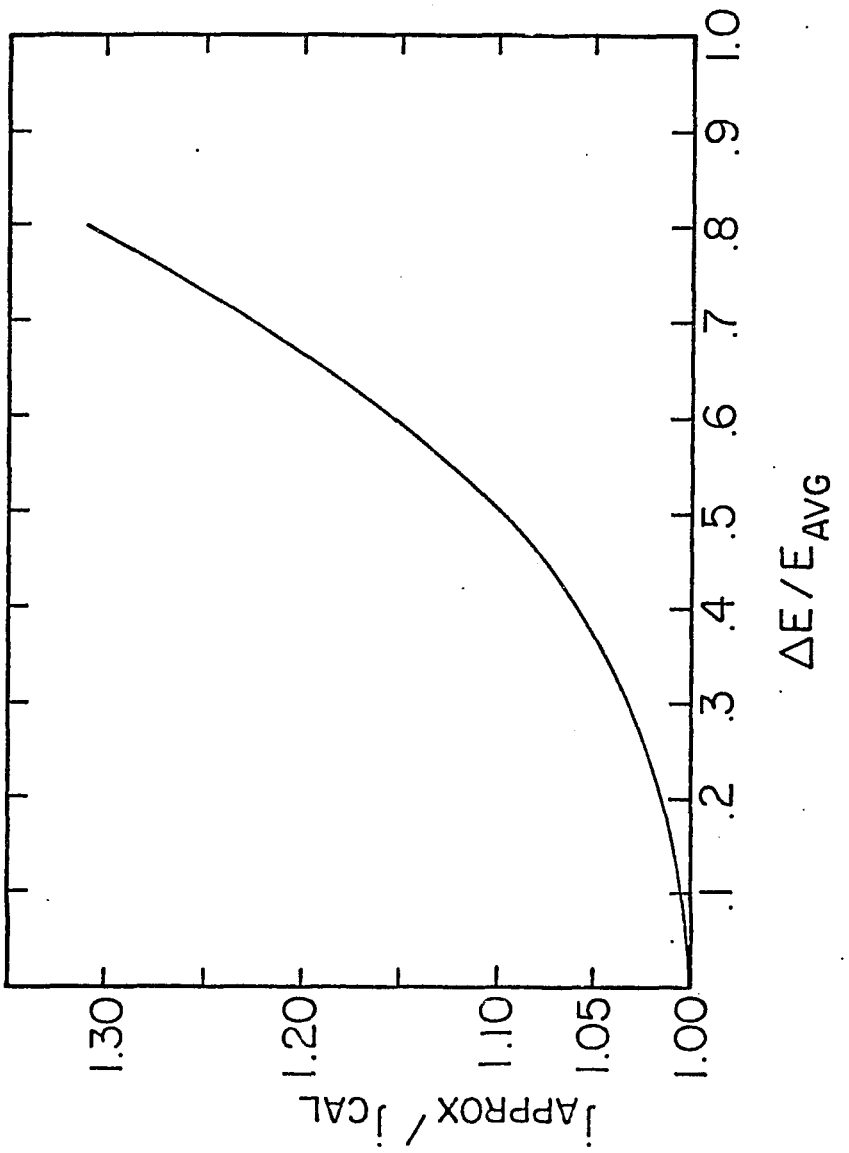

V.1 $\Delta E/E$ vs. error in flux estimates

j(E) approx/ j(E) exact. If the value of $\Delta E/E$ remains $\lesssim .3$, then the resultant error in the differential flux approximation above the actual flux would be overestimated by ~3.6% or less. $\Delta E/E$ values for this experiment range from .15 at the lowest energy interval to .35 at the highest interval.

At energies above the last energy bin of .95 G/Gm the remaining integral spectrum can be converted into a differential flux measurement by assuming that the differential flux can be expressed as a power law in the form of $j=E^{-\gamma}$. From that assumption, it follows that

$$5.3) \qquad j(E_1)=\frac{(\gamma-1)J(E_1\to\infty)}{E_1}$$

A nominial value of 2.7 was chosen for gamma. The conversion from differential to integral flux is most sensitive to the differential spectrum near E1. Since approximately two-thirds of the events lie between E1 and 2 E1, the differential data point constructed from the integral flux data was plotted at a value of 1.5 times E1.

The less abundant charge groups have been combined and their associated differential intensities determined.

V-3) Calculation of the Integral Intensities

The integral flux $J(E \rightarrow \infty)$ was determined by taking the sum of the corrected raw counts from the leading edge of the energy bin to infinity divided by the collection factor ($A\Omega$ t). Integral intensities were derived for each charge component from Z=4 through Z=26.

As discussed in Chapter IV-6, the assignment of Gm determines the energy scale assignment for each charge. Comparing the integral and differential intensities from the three flights with different Cerenkov thresholds and different instrument and atmospheric corrections provides an exceedingly sensitive test of the assignment of the energy scales. Inconsistencies in deriving the spectra down to the 2% level can be detected by this comparison test.

For the abundant nuclei, individual differential and integral points have been calculated and compared.

Table V.2 lists the total number of raw counts and corrected raw counts above the usable Cerenkov threshold for the three flights. Figures V.2 show the differential flux times $E^{-2.5}$ (combined and averaged data from the three flights) plotted versus kinetic energy in order to visually enhance the spectral shape. Any change in the spectral index as a function of energy becomes much more apparent in

this graphic representation.

Table V.3 is a summary of the differential and integral intensities showing

1) The mean kinetic energy and the associated delta E width for each bin in Gev; †
2) The kinetic energy value for the integral intensity point in Gev; †††
3) The differential intensity in #/m²-sec-sr-Gev; #
4) The integral intensity in #/m²-sec-sr; ##
5) The errors on the respective fluxes. @

The associated errors listed in this Table for the differential and integral fluxes are determined by the statistical variances on the raw counts only.

As a further consistency check on the average spectral indices and the selection of the energy scales, the differential and integral spectra were compared. If one assumes that the differential spectrum can be expressed as a power law, then the ratio of the differential flux times $E^{2.5}$ divided by the integral flux times $E^{1.5}$ yields the spectral index minus one.

$$5.4) \qquad \frac{J(E)\,E^{2.5}}{J(E\to\infty)\,E^{1.5}} = (\gamma - 1)$$

This comparison is sensitive to any inconsistencies in the selection of energy scales that might have occurred in deriving the energy spectra from the three overlapping

flights as discussed in Chapter V-3. If the spectrum is slowly changing as a function of energy, this also should be mirrored in the ratios. Table V.5 lists the derived best-fit differential spectra indices over the charge range from boron to iron.

Key for Table V.3

† energy at which the differential flux was evaluated (GeV/nuc)

†† ΔE (GeV/nuc)

††† energy at which integral flux was evaluated

differential flux #/ m^2-sec-sr-GeV

integral flux #/m^2-sec-sr

@ respective error in the measurement

Table V.3 1976 Particle intensity data

	Boron		Carbon		Nitrogen	
10.54[†]	6.04-3[#]	8.90-4[@]	3.21-2	2.19-3	6.95-3	1.00-3
1.62[††]						
9.72[†††]	3.77-2[##]	2.85-3[@]	2.32-1	7.52-3	4.37-2	3.22-3
12.38	3.40-3	6.01-4	2.05-2	1.55-3	3.79-3	6.6-4
2.05						
11.36	2.79-2	2.46-3	1.80-1	6.63-3	3.24-2	2.78-3
14.91	2.17-3	3.89-4	1.38-2	1.05-3	2.48-3	4.38-4
3.03						
13.40	2.09-2	2.13-3	1.38-1	5.82-3	2.47-2	2.43-3
18.94	9.94-4	2.07-4	6.34.3	5.52-4	1.48-3	2.65-4
4.99						
16.42	1.43-2	1.78-3	9.66-2	4.89-3	1.72-2	2.04-3
25.28	6.28-4	1.34-4	3.65-3	3.42-4	6.89-4	1.49-4
7.68						
21.46	9.38-3	1.45-3	6.50-2	4.04-3	9.78-3	1.55-3
35.32	1.73-4	6.10-5	1.13-3	1.63-4	1.51-4	5.70-5
12.43						
29.10	4.56-3	1.02-3	3.70-2	3.07-3	4.42-3	1.04-3
41.54	2.85-5	2.85-5	8.88-4	9.26-5	1.04-4	3.14-5
*						
41.54	2.41-3	6.89-4	2.17-2	2.26-3	2.55-3	7.68-4

	Oxygen		Neon		Magnesium	
10.54	3.66-2	2.35-3	6.37-3	1.02-3	7.78-3	1.17-3
1.62						
9.72	2.52-1	8.05-3	3.39-2	2.97-3	5.32-2	3.89-3
12.38	2.14-2	1.64-3	2.61-3	5.71-4	5.30-3	8.71-4
2.05						
11.36	1.93-1	7.10-3	2.36-2	2.47-3	4.06-2	3.40-3
14.91	1.29-2	1.05-3	1.59-3	3.65-4	2.79-3	5.00-4
3.03						

13.40	1.49-1	6.25-3	1.82-2	2.18-3	2.98-2	2.89-3
18.94	4.60-3	6.27-4	1.02-3	2.28-4	1.53-3	2.95-4
4.99						
16.42	1.10-1	5.38-3	1.34-2	1.88-3	2.13-2	2.46-3
25.28	4.26-3	3.78-4	5.76-4	1.40-4	7.50-4	1.64-4
7.68						
21.46	7.22-2	4.38-3	8.31-3	1.49-3	1.37-2	1.97-3
35.32	1.46-3	1.82-4	1.73-4	6.10-5	2.80-4	8.09-5
12.43						
29.10	3.95-2	3.28-3	3.89-3	1.04-3	7.91-3	1.52-3
41.54	8.78-4	9.75-5	7.13-5	2.91-5	1.81-4	4.67-5
*						
41.54	2.14-2	2.38-3	1.47-3	7.11-4	4.42-3	1.14-3

	Silicon		Iron		17-19	
10.54	5.54-3	1.01-3	4.88-3	1.12-3	1.49-3	6.66-4
1.62						
0.72	4.74-2	3.79-3	3.69-2	3.93-3	7.64-3	1.50-3
12.38	5.10-3	8.74-4	4.18-3	9.13-4	1.05-3	3.95-4
2.05						
11.36	3.85-2	3.41-3	2.89-2	3.48-3	5.36-3	1.26-3
14.91	2.87-3	5.34-4	1.99-3	5.32-4	2.65-4	1.53-4
3.03						
13.40	2.80-2	2.90-3	2.04-2	2.94-3	3.22-3	9.70-4
18.94	1.64-3	3.15-4	8.33-4	2.63-4	1.88-4	1.09-4
4.99						
16.42	1.93-2	2.41-3	1.43-2	2.46-3	2.41-3	8.53-4
25.28	7.50-4	1.72-4	4.36-4	1.54-4	8.72-5	6.17-5
7.68						
21.46	1.11-2	1.83-3	1.02-2	2.04-3	1.47-3	6.59-4
35.32	1.94-4	6.86-5	2.16-4	8.80-5	0.00-0	0.00-0
12.43						
29.10	5.36-3	1.26-3	6.83-3	1.71-3	8.04-4	4.64-4

41.54	1.21-4	3.82-5	1.70-4	5.38-5	3.29-5	1.90-5
*						
41.54	2.95-3	9.32-4	4.15-3	1.31-3	8.04-4	4.64-4
	21-24		9+11+13		16+18+20	
10.54	1.24-3	5.07-4	1.14-3	7.21-4	2.40-3	6.93-4
1.62						
9.72	9.78-3	2.04-3	1.96-2	2.29-3	1.90-2	2.50-3
12.38	9.15-4	3.74-4	1.57-3	4.53-4	1.63-3	5.17-4
2.05						
11.36	7.77-3	1.59-3	1.51-2	2.06-3	1.51-2	2.23-3
14.91	4.42-4	2.21-4	6.19-4	2.34-4	1.02-3	3.39-4
3.03						
13.40	5.90-3	1.39-3	1.13-2	1.47-3	1.17-2	1.94-3
18.94	5.37-4	1.90-4	9.67-4	2.28-4	8.59-4	2.38-4
4.99						
16.42	4.56-3	1.22-3	9.38-3	1.59-3	8.58-3	1.65-3
25.28	8.72-5	6.17-5	2.27-4	8.57-5	3.32-4	1.17-4
7.68						
21.46	1.88-3	7.66-4	4.56-3	1.11-3	4.29-3	1.15-3
35.32	3.23-5	3.23-5	8.63-5	3.86-5	4.31-5	3.05-5
12.43						
29.10	1.21-3	6.03-4	2.68-3	8.48-4	1.61-3	6.57-4
41.54	3.84-5	2.22-5	5.48-5	2.45-5	4.39-5	2.19-5
*						
41.54	9.38-4	5.43-4	1.34-3	5.99-4	1.04-3	5.36-4

1977 Particle intensity data

	Boron		Carbon		Nitrogen	
17.58	1.15-3	1.72-4	8.17-3	4.81-4	1.70-3	2.16-4
2.86						
16.15	9.49-3	7.48-4	9.73-2	2.85-3	1.84-2	1.21-3
21.11	6.07-4	1.03-4	4.69-3	3.00-4	1.05-3	1.40-4
4.20						
19.00	8.83-3	8.09-4	7.40-2	2.50-3	1.35-2	1.04-3

26.72 7.02	3.50-4	6.10-5	2.87-3	1.85-4	1.07-4	6.69-5
23.20	6.28-3	6.98-4	5.43-2	2.16-3	9.09-3	8.59-4
35.54 10.64	1.65-4	3.60-5	1.35-3	1.05-4	2.44-4	4.31-5
30.22	3.82-3	5.52-4	3.42-2	1.72-3	7.64-3	8.82-4
49.52 17.31	5.07-5	1.79-5	4.72-4	5.64-5	8.63-5	2.09-5
48.86	2.06-3	3.97-4	1.92-2	1.31-3	3.65-3	5.56-4
58.17 *	3.47-5	7.95-6	3.40-4	2.70-5	6.29-5	1.23-5
58.17	1.19-3	2.72-4	1.16-2	9.23-4	2.15-3	4.22-4

	Oxygen		Neon		Magnesium	
17.58 2.86	9.61-3	5.37-4	1.51-3	2.15-4	2.07-3	2.61-4
16.15	1.12-1	3.01-3	1.77-2	1.26-3	2.13-2	1.45-3
21.11 4.20	5.76-3	3.43-4	8.68-4	1.34-4	1.12-3	1.58-4
19.00	8.48-2	2.72-3	1.34-2	1.10-3	1.53-2	1.20-3
26.72 7.02	3.23-3	1.98-4	4.32-4	7.40-5	5.63-4	8.59-5
23.20	6.02-2	2.29-3	9.75-3	9.43-4	1.06-2	1.00-3
35.54 10.64	1.37-3	1.07-4	2.77-4	4.81-5	2.72-4	4.89-5
30.22	3.79-2	1.85-3	6.72-3	7.87-4	6.68-3	8.04-4
49.52 17.31	5.43-4	5.72-5	9.13-5	2.28-5	1.07-4	2.51-5
40.86	2.38-2	1.48-3	3.78-3	5.97-4	3.78-3	6.13-4
58.17 *	4.20-4	3.23-5	6.42-5	1.31-5	5.65-5	1.26-5
58.17	1.44-2	1.10-3	2.20-3	4.48-4	1.93-3	4.23-4

	Silicon		Iron		17-19	

17.58	1.43-3	2.23-4	9.83-4	2.14-4	2.46-4	9.29-5
2.86						
16.15	1.57-2	1.26-3	1.41-2	1.38-3	2.77-3	5.33-4
21.11	8.78-4	1.44-4	1.86-4	1.38-4	1.46-4	5.98-5
4.28						
19.00	1.16-2	1.08-3	1.12-2	1.23-3	2.15-3	3.93-4
26.72	5.82-4	9.09-5	3.50-4	8.26-5	8.76-5	3.58-5
7.02						
23.20	7.91-3	8.95-4	8.78-3	1.09-3	1.58-3	4.23-4
35.54	1.11-4	3.22-5	2.56-4	5.72-5	1.65-5	1.17-5
10.64						
30.22	3.82-3	6.28-4	6.32-3	9.23-4	9.66-4	3.42-4
49.52	4.82-5	1.70-5	8.37-5	2.52-5	1.78-5	1.30-5
17.31						
40.86	2.64-3	5.27-4	3.60-3	6.93-4	7.91-4	3.23-4
58.17	5.26-5	1.28-5	6.29-5	1.57-5	1.41-5	8.15-6
*						
58.17	1.80-3	4.37-4	2.15-3	5.38-4	4.83-4	2.79-4

	21-24		9+11+13		16+18+20	
17.58	3.69-4	1.17-4	6.45-4	1.27-4	5.84-4	1.46-4
2.86						
16.15	3.51-3	6.12-4	7.64-3	8.01-4	5.40-3	7.64-4
21.11	1.46-4	5.98-5	4.60-4	9.81-5	3.14-4	8.70-5
4.20						
19.00	2.46-3	5.13-4	5.80-3	7.19-4	3.73-3	6.40-4
26.72	9.39-5	5.42-5	1.81-4	4.85-5	1.44-4	5.09-5
7.02						
23.29	1.84-3	4.47-4	3.82-3	5.83-4	2.42-3	5.27-4
35.54	6.19-5	3.10-5	9.08-5	2.87-5	7.43-5	2.81-5
10.64						
30.22	11.41-3	3.90-4	2.59-3	4.81-4	1.54-3	4.26-4

49.52	3.30-5	1.48-5	4.06-5	1.44-5	1.01-5	7.18-6
17.31						
40.86	9.66-4	3.22-4	1.67-3	3.83-4	7.47-4	3.05-4
58.17	1,28-5	6.42-6	2.82-5	8.51-6	1.28-5	6.42-6
*						
58.17	4.39-4	2.20-4	9.66-4	2.91-4	4.39-4	2.20-4

1978 Particle intensity data

	Boron		Carbon		Nitrogen	
28.07	3.74-4	6.32-5	2.84-3	1.91-4	5.03-4	7.88-5
5.54						
25.30	7.42-3	6.92-4	5.28-2	1.99-3	7.42-3	7.21-4
35.45	1.83-4	3.53-5	1.55-3	1.11-4	1.88-4	3.68-5
9.24						
30.83	5.35-3	5.98-4	3.71-2	1.68-3	4.63-3	5.75-4
47.07	1.08-4	2.41-5	5.27-4	5.69-5	8.34-5	2.15-5
14.00						
40.07	3.65-3	5.02-4	2.28-2	1.33-3	2.90-3	4.64-4
65.47	3.53-5	1.18-5	2.13-4	2.80-5	2.85-5	1.01-5
27.78						
54.07	2.15-3	3.74-4	1.54-2	1.07-3	1.73-3	3.54-4
76.86	2.58-5	5.27-6	1.94-4	1.60-5	2.08-5	5.21-6
*						
76.86	1.17-3	2.38-4	8.78-3	7.24-4	9.42-4	2.35-4

	Oxygen		Neon		Magnesium	
28.07	2.94-3	2.01-4	4.08-4	7.58-5	5.44-4	8.94-5
5.54						
25.30	5.48-2	2.07-3	7.42-3	7.65-4	9.64-3	8.99-4
35.45	1.47-3	1.09-4	2.08-4	4.16-5	2.81-4	5.05-5
9.24						
30.83	3.85-2	1.75-3	5.16-3	6.40-4	6.63-3	7.51-4

47.07	6.78-4	6.27-5	8.88-5	2.22-5	1.16-4	2.65-5
14.00						
40.07	2.49-2	1.43-3	3.24-3	5.12-4	4.:3-3	5.88-4
65.47	2.51-4	3.06-5	3.39-5	1.07-5	3.53-5	1.11-5
27.78						
54.07	1.52-2	1.13-3	2.00-3	4.07-4	2.41-3	4.56-4
76.86	1.87-4	1.70-5	2.33-5	6.23-6	3.17-5	7.46-6
*						
76.86	8.44-3	7.70-4	1.05-3	2.82-4	1.43-3	3.37-4

	Silicon		Iron		17-19	
28.07	4.15-4	7.98-5	3.06-4	7.65-5	7.48-5	3.34-5
5.54						
25.30	7.68-3	8.10-4	6.97-3	8.64-4	1.47-3	3.46-4
35.45	1.79-4	4.01-5	1.43-4	4.12-5	1.63-5	1.15-5
9.24						
30.83	5.39-3	6.79-4	5.27-3	7.53-4	1.05-3	2.93-4
47.07	7.00-5	2.02-5	9.95-5	2.76-5	2.15-5	1.08-5
14.00						
40.07	3.73-3	5.69-4	3.95-3	6.50-4	9.04-4	2.73-4
65.47	5.29-5	1.32-5	4.20-5	1.27-5	1.08-5	5.42-6
27.78						
54.07	2.75-3	4.94-4	2.56-3	2.53-4	5.65-4	2.14-4
76.86	2.83-5	7.31-6	3.08-5	8.55-6	5.00-6	2.89-6
*						
76.86	1.28-3	3.31-4	1.39-3	3.87-4	2.26-4	1.30-4

	21-24		9+11+13		16+18+20	
28.07	8.16-5	3.65-5	2.86-4	6.23-5	1.50-4	4.73-5
5.54						
25.30	.13-3	3.26-4	3.50-3	4.81-4	2.71-3	4.87-4
35.45	1.63-5	1.15-5	8.97-5	2.70-5	7.75-5	2.74-5
9.24						

30.83	7.16-4	2.53-4	2.52-3	4.46-4	1.88-3	4.11-4
47.07	1.08-5	7.61-6	7.00-5	1.94-5	2.96-5	1.32-5
14.00						
40.07	.27-4	2.15-4	1.66-3	3.62-4	1.17-3	3.24-4
65.47	0.00-0	0.00-0	5.42-6	3.83-6	4.07-6	2.88-6
27.78						
54.07	3.39-4	1.69-4	7.68-4	2.26-4	7.16-4	2.53-4
76.86	7.50-6	3.75-6	1.17-5	4.76-6	1.25-5	5.10-6
*						
76.86	3.39-4	1.69-4	5.27-4	2.15-4	2.65-4	2.31-4

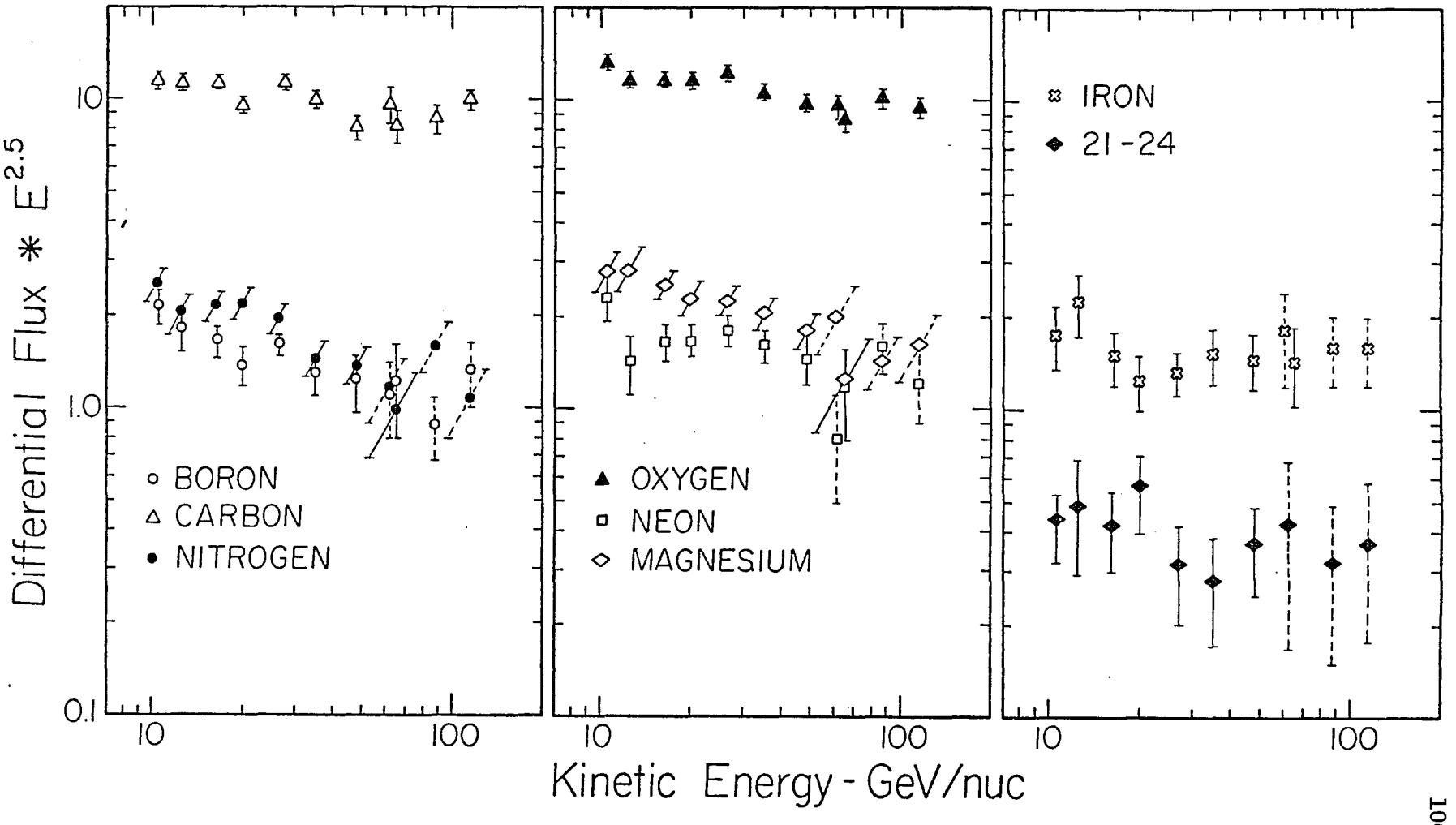

V.2 Differential flux times $E^{2.5}$

	1976		1977		1978	
	RC	CRC	RC	CRC	RC	CRC
	E_k>9.72 GeV		E_k>16.15 GeV		E_k>25.30 GeV	
B	174	281	161	216	115	197
C	958	1741	1165	2216	706	1401
N	184	326	230	418	106	197
O	983	1884	1290	2256	700	1454
F	18	36	24	46	16	31
Ne	130	253	198	403	94	197
Na	21	41	30	61	17	34
Mg	187	413	215	484	115	256
Al	34	70	37	68	20	38
Si	157	354	156	357	90	204
P	-	-	-	-	-	-
S	30	73	25	60	15	36
Cl	9	19	8	19	6	12
Ar	1	25	10	25	6	13
K	6	14	9	21	6	13
Ca	17	44	15	38	10	23
Sc	5	6	4	9	2	4
Ti	7	17	9	21	2	4
V	7	17	11	26	2	4
Cr	11	21	9	23	6	16
Fe	88	273	104	320	65	185

TABLE V.4
AVERAGE SPECTRAL INDICES

ELEMENT	SPECTRAL INDEX
Boron	-2.80 ± 0.07
Carbon	-2.65 ± 0.05
Nitrogen	-2.85 ± 0.07
Oxygen	-2.65 ± 0.03
Neon	-2.65 ± 0.09
Magnesium	-2.80 ± 0.09
Silicon	-2.81 ± 0.11
Iron	-2.53 ± 0.08
17-19	-2.63 ± 0.20
21-24	-2.58 ± 0.22
9+11+13	-2.89 ± 0.16

CHAPTER VI

PROPAGATION

In an attempt to interpret the results of Chapter Five, it would be advantageous to discuss general models of cosmic ray propagation. The first model discussed is derived from a general transport equation which includes the appropriate source and sink functions for cosmic ray propagation in the galaxy. The second model, the leaky box model, is derived from the general transport equation with simplifying assumptions that replace the diffusion term.

VI-1) PROPAGATION

One method of modeling cosmic ray propagation in the galaxy begins with the continuity equation

$$6.1) \qquad \frac{\partial n}{\partial t} + \nabla \cdot J_n + \text{sinks} = \text{source}$$

where n is a number density expressed in #/vol-energy. The source term can be divided into two major classes:

i) injection of particles into the energy-volume space by the source; and

ii) production of particles by fragmentation from higher Z species into lower Z nuclei (ie. k-type into i-type).

The losses or sinks from the energy-volume space can be characterized by

i) loss from i-type to k-type nuclei by fragmentation.

ii) loss from the volume space by diffusion.

iii) loss from the energy space by energy loss mechanisms.

iv) loss from particle type by nuclear decay.

v) loss by catastrophic losses.

vi) loss from containment volume.

The sink term can be expressed as

$$6.2) \qquad \left[\frac{\partial}{\partial E}\left\{\frac{dE}{dt}n\right\} + \frac{n}{\tau_i}\right]$$

The first term represents the number of particles lost between E and E′ due to energy losses. The second term represents the number of particles lost from an energy-volume bin by some type of escape from the system where τ is the mean lifetime for escape, decay, fragmentation, etc. Therefore

$$6.3) \qquad \frac{1}{\tau_i} = \frac{1}{\tau_{escape}} + \frac{1}{\tau_{decay}} + \frac{1}{\tau_{fragmentation}} + \cdots$$

The source term can be expressed as

$$6.4) \qquad q_i(r,t,E) + \sum_k \frac{n_k}{\tau_{ki}}$$

where the first term is the source production term and the

second term represents the injection of k-type nuclei being fragmented into i-type species in a fragmentation time τ_{ki} . The transport equation now becomes

$$6.5) \qquad \frac{\partial n_i}{\partial t} + \nabla J_{ni} + \left[\frac{\partial}{\partial E} \left(n_i \frac{dE}{dt} \right) + \frac{n_i}{\tau_i} \right] = q(r,t,E) + \sum \frac{n_k}{\tau_{ki}}$$

By assuming a linear diffusion model, the $\nabla \cdot J_{ni}$ term can be expressed in terms of a gradient in n_i .

$$6.6) \qquad J_{ni} = -D(E) \nabla_{ni}$$

where $D(E)$ is the diffusion coefficient. The energy dependent diffusion coefficient can be expressed in terms of a scattering mean free path

$$6.7) \qquad D(E) = 1/3 \lambda(E) \beta C$$

The cosmic ray transport equation for the number density becomes

$$6.8) \qquad \frac{\partial ni}{\partial t} - \nabla \cdot (D(E) \nabla_{ni}) + \frac{\partial}{\partial E} (\dot{E}_{ni}) + \frac{n_i}{\tau_i} = q(r,t,E) + \sum \frac{n_k}{\tau_{ki}}$$

The solution to the transport equation can be derived by constructing a suitable Green's function with the appropriate boundary conditions.

Syrovatskii (1959) first suggested the form of the Green's function of

$$6.9) \qquad G = \frac{1}{\dot{E}(E)} \exp\left[-\int_{E_o}^{E} \frac{dE'}{\dot{E}(E')\tau(E')}\right] \Phi(r,t,E)$$

where

$$6.10) \qquad \Phi(r,t,E) = \phi(r, r_o, x)\,\delta(t - t_o) \; ; \; x = \int_{E_o}^{E} \frac{D(E')}{\dot{E}(E')} dE'$$

and must satisfy the condition

$$6.11) \qquad \frac{\partial \phi}{\partial x} - \nabla^2 \phi = \frac{\dot{E}}{|\dot{E}|} \cdot \delta(x)\,\delta(r - r_o)$$

The boundary conditions placed on ϕ must be the same as those placed on n. Once the Green's function has been obtained, the transport equation becomes

$$6.12) \qquad n_i(r,t,E) = \frac{1}{\dot{E}(E)} \int_{E}^{\infty} dE_o \exp\left[-\int_{E_o}^{E} \frac{dE'}{\dot{E}(E')\tau_i(E')}\right] \int d^3 r_o\, \phi(r, r_o, x) \cdot \left[q_i(r,t,E_o) + \sum_k \frac{n_k(r,t,E_o)}{\tau_{ki}}\right]$$

For the steady state case where $\partial n / \partial t = 0$, the solution reduces to

$$6.13) \qquad n(r,E) = \int \frac{dE_o}{\dot{E}(E)} \exp\left[-\int_{E_o}^{E} \frac{dE'}{\dot{E}(E')\tau(E')}\right] \int d^3 r_o\, \phi(r, r_o, x) \cdot \left[q(r, E_o) + \sum \frac{n_k(r_o, E_o)}{\tau_{ki}}\right]$$

Assuming the source term can be factored as follows,

6.14) $$q_i(r_o,E_o) = f(r_o)\, q_i(E_o)$$
$$n_i(r_o,E_o) = f(r_o)\, n_i(E_o)$$

then the resulting solution is

6.15) $$n(r,E)=\int_E^{\infty}\frac{dE_o}{\dot{E}(E)}\exp\left[-\int_{E_o}^{E}\frac{dE'}{\dot{E}(E')\,\tau(E')}\right]\left[q_i(E_o)+\sum_k\frac{n_k(E_o)}{\tau_{ki}}\right]P(r_o,E_o)$$

where

6.16) $P(r,E_o)$ = Pathlength distribution function
$$= d^3r_o\,\phi(r,x,r_o)\,f(r_o)$$

Equation 6.14 can be rewritten in terms of a flux $j(x)$.

6.17) $$j(E)=\frac{1}{w(E)}\int_0^{\infty}dx'\,w(E')\exp\left[-\int_0^{x}\frac{dx}{\lambda_i}\right]\left[q_i(E_o)+\sum_k\left(\frac{j_i(E_o)}{\lambda_{ki}(E_o)}\right)\right]P(r,E_o)$$

where $\omega(E) = dE/dt$, and λ_i = mean free path. It should be noted that $P(r,E_o)$ contains all of the spatial information on the distribution of the cosmic ray sources.

VI-2) Leaky Box Model

In some cases it is appropriate to make assumptions that simplify the general transport equation. The "leaky box" model which has been commonly used assumes that efficient mixing occurs within a containment volume and the

cosmic rays maintain a given probablity of escape regardless of their position within the volume. The diffusive term in the transport equation is replaced by a generalized loss term

6.18) $$\nabla\cdot(D(E)\nabla n_i) \longrightarrow \frac{n_i}{\tau_i}$$

The transport equation becomes

6.19) $$\frac{d}{dE}(E_i, n_i) + \frac{n_i}{\tau_i} = q_i + \sum_k \left(\frac{n_k}{\tau_{ki}}\right)$$

By changing variables from E to X and changing from a number density to a flux, Equation 6.19 can be rewritten as

6.20) $$\frac{d}{dx}(wj_i) + \frac{wj_i}{\lambda_i} = \left[q_i + \sum_k \frac{j_k}{\lambda_{ki}}\right].$$

This first order differential equation has a solution of

6.21) $$j(E,x) = \frac{1}{w(E)}\int_0^x dx' w(E') \exp\left[-\int_x^{x'} \frac{dx'}{\lambda}\right]\left[q_i(E',x') + \sum_k \frac{j_k(E',x)}{\lambda_{ki}}\right]$$

Where the connection between E' and X lies in the range relationship

6.22) $$R_i(E') = R(E) + x$$

where E' = the energy measured at the source and E = the observed energy aftering traverising a path length of X g/cm^2. It is interesting to note at this point the similiarities between the solutions of the general and leaky box equations. If one looks specifically at Equations 6.17

and 6.21, it becomes obvious that in the context of the general transport equation, the leaky box model solution is identical for the case where the pathlength distribution function is described by

$$6.23) \quad P(x) = \exp\int_0^x \frac{dx}{\lambda} = e^{x/\lambda}$$

Figure VI.1 shows the various pathlength distributions predicted by the leaky box model, the no near source model of Lezniak and Webber (1978), and the nested leakybox model of Cowsik and Willson (1975). All of these distributions are based on solutions derived from Equation 6.17.

From the solutions derived above, the steady state intensities that we observe at the earth are influenced by four major factors.

1) The distribution of the cosmic ray sources. The actual distribution of the sources in space and time will determine the pathlength distributions through which the cosmic rays must propagate before they are observed at the earth.

2) Escape losses. As the cosmic ray traverses the galactic disk, there exists a finite probablity that the particle will escape the bounds of the confinement volume either by a diffusive mechanism or other physical mechanisms that remove the cosmic ray from the energy-space dimensions. The probablity of escape increases as the energy of the

particle increases. This will result in in a steepening of the spectra at the higher energies.

3) Energy loss mechanisms. The rate of ionization energy loss that occurs in the interstellar medium depends on the energy and charge of the cosmic ray and the amount of material traversed. If one assumes that the ratio of two species at the source are constant, the observed ratios will be modified as a function of energy due to the different rates of energy losses. For example, j(B)/j(C) will show a rise at the lower energies due to the increased rate of ionization energy loss of the higher Z species.

4) Fragmentation in the interstellar medium. The amount of fragmentation that occurs depends on the pathlength distribution function, energy, and the interaction mean free path of the individual nuclei. Spallation reactions are directly proportional to the amount of material traversed in the interstellar medium. The primary particles at the lower energies will undergo a larger amount of spallation reactions due to the longer residence time in the galaxy and thereby enhance the secondary nuclear components at these energies.

In discussing the results of the experiment, propagation calculations were carried out for 202 nuclei through a distribution of pathlengths of the form

6.24) $$P(x,E) = 1/\lambda \cdot \exp\left[x/\lambda(E)\right]$$

where $\lambda(E) = 7.0 E_K^{-0.33}$ for $E_K > 1.0$ GeV/Nuc

$\lambda(E) = 7.0$ for $E_K \leq 1.0$ GeV/Nuc

This distribution was choosen as a best fit to the observed data as shcwn in Chapter VII-3. The propaqation proqrams were provided by J. A. Lezniak.

The Silberberq and Tsao (1977) semi-emperical cross sections have been used for the propaqation calculations. These cross sections have been modified using the results of Lindstrom (1978) and Perron (1976). These calculations were done usinq an interstellar hydrogen density of .25 atoms/cm^3. The assumed source injection spectra was of the form

6.25) $j(E) = E_K^{-2.4}$

The source abundances presented by Lezniak and Webber (1978) were used in the calculations except where noted.

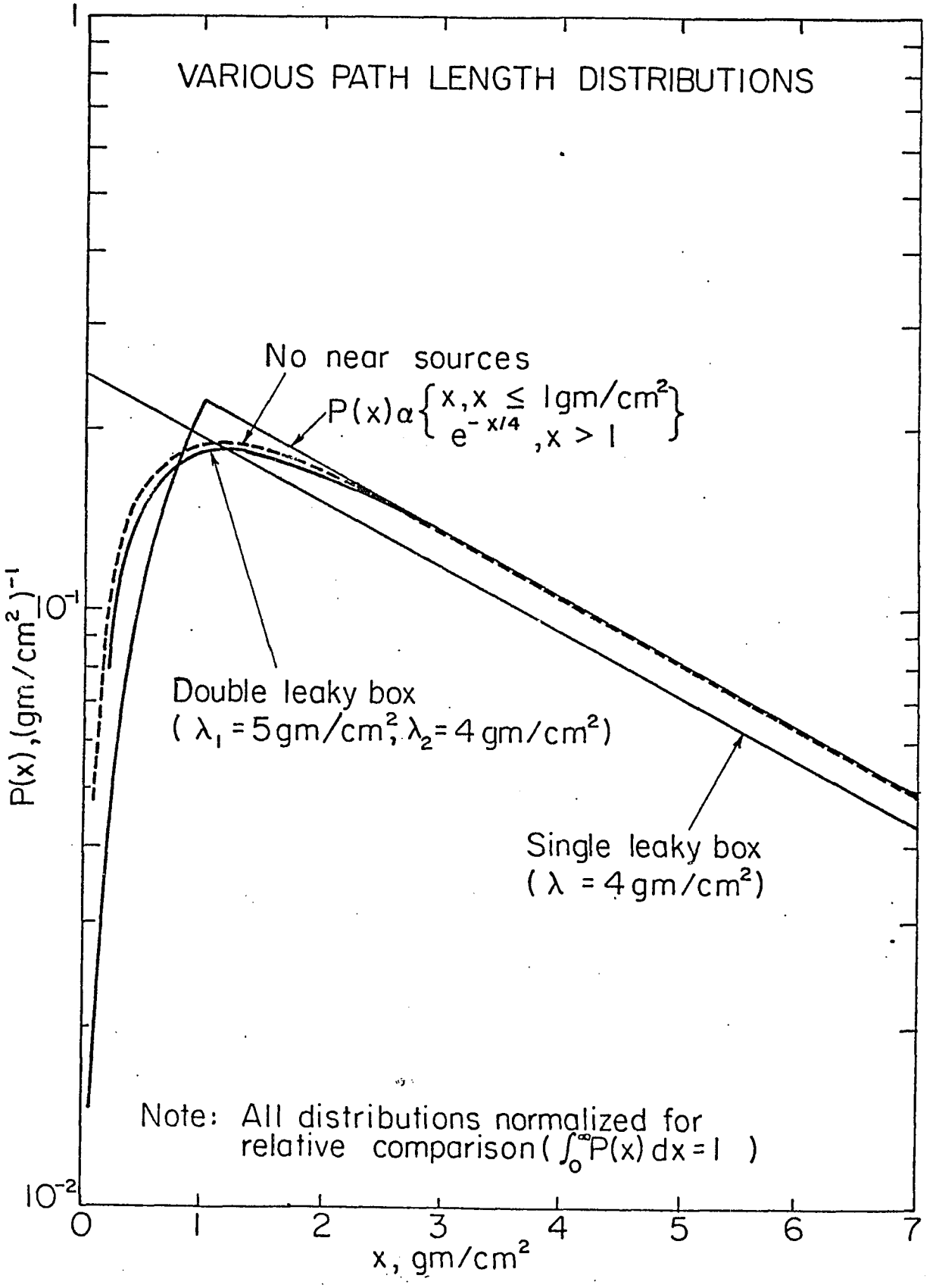

VI.1 Various path length distribution functions

CHAPTER VII

DISCUSSION

VII-1) Observation of Primary Spectra.

There are two general features present in the observation of the primary species. 1) When attempting to fit the differential intensities to a power fit either by a chi-square test or by a least-square method, it becomes apparent that the spectral index is slowly changing as a function of energy. The spectrum is steepening as it approaches the higher energies. For example, carbon and oxygen between the energy ranges of 10 to 30 GeV/nuc have spectral indices of -2.53 .05 and -2.49 ±.05 respectively. In the interval between 30.0 and 100.0 GeV/nuc, the spectra steepen to -2.63 ± .04 and -2.65 ±.08 respectively. 2) There is a trend for the low Z nuclei to have an overall steeper slope than the slope of the higher Z elements. Carbon, oxygen and iron have a overall best fit spectral index of -2.65 ±.04, -2.65 ±.04 and -2.53 ±.06 respectively. The low Z nuclei have spectral indices which are close to the observed proton spectrum.

In the context of a diffusive or leaky box model, these features can be explained by the competing effects of the galactic escape and nuclear interaction parameters. As discussed in Chapter VI-1, for the steady state leaky box

model

$$7.1) \qquad 1/\lambda_T = 1/\lambda_{escape} + 1/\lambda_{interaction} + 1/\lambda_{decay}$$

represents the total interaction mean free path. The flatness of the iron spectrum can be attributed to the fact that the interaction mean free path for iron ($\sim 2.6 g/cm^2$) is much larger than that of the lower Z nuclei. This implies that the interaction losses dominate at lower energies as compared to the escape interactions. Therefore, one would expect to see a flatter spectra for the higher Z nuclei due to the depletion of particles by nuclear interactions. The observed steepening of the individual spectra reflects the point where escape from the confinement volume begins to dominate. As the energy increases, the probability of interaction decreases since the confinement time is proportional to β and the probability for escape increases. Selected primary to primary ratios have been plotted in Figure VII.5 along with the predicted ratio derived from an energy dependent leaky box model.

Figure VII.1 shows the differential intensity of oxygen as determined by other experimenters. The intensities presented in this thesis are in good agreement with the other reported results over the observed energy range. The absolute intensities of the primaries are in general slightly less than those reported by Simon et al. (1979) and Orth et al.(1979) over the energy range of 10 to 30

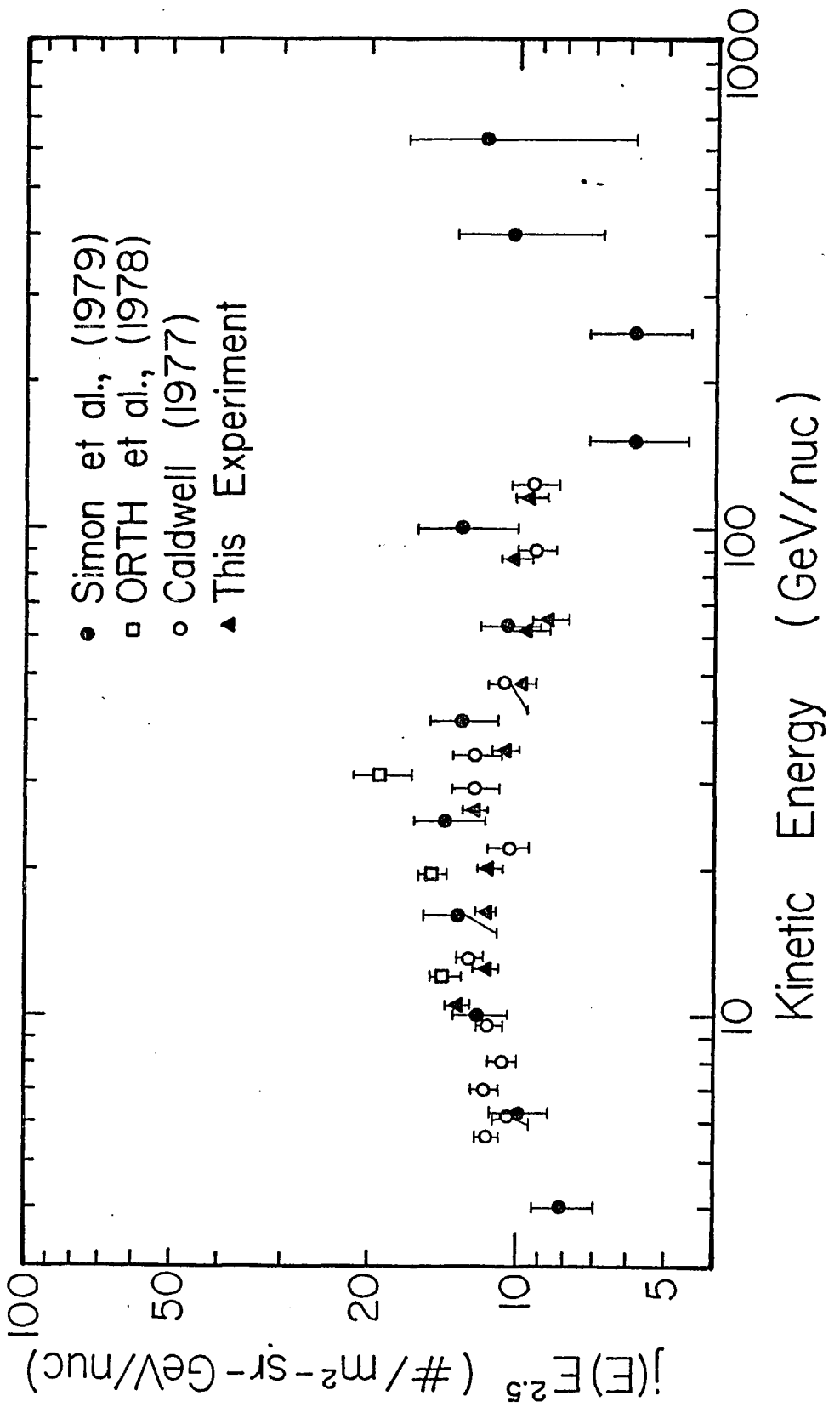

VII.1 The differential intensity j(E) vs. E for Oxygen, other experimental observations

GeV/nuc and in good agreement with the results reported by Caldwell (1977).

VII-2) Observation of the Secondary Spectra.

The spectra of the secondaries are in general steeper than that of their respective primaries. These nuclei are produced mainly by spallation of their respective primaries. If one assumes that the secondary has the same velocity (Ek/nuc) as its parent nuclei, then one would expect to see the fragment having the same energy spectra as the incident particle. The increased slope of the spectrum can be attributed to the energy dependence of the escape mean free path and to the energy dependence of the cross sections at the lower energies.

VII-3) Secondary to Primary Ratios.

The secondary to primary ratios are of prime interest in determining the path length distribution and the escape parameters. The ratios were selected such that the secondary component is thought to be absent or have a small source component and produced mainly by fragmentation. These ratios have been plotted in Figure VII.2 along with the expected ratios derived from an energy dependent leaky

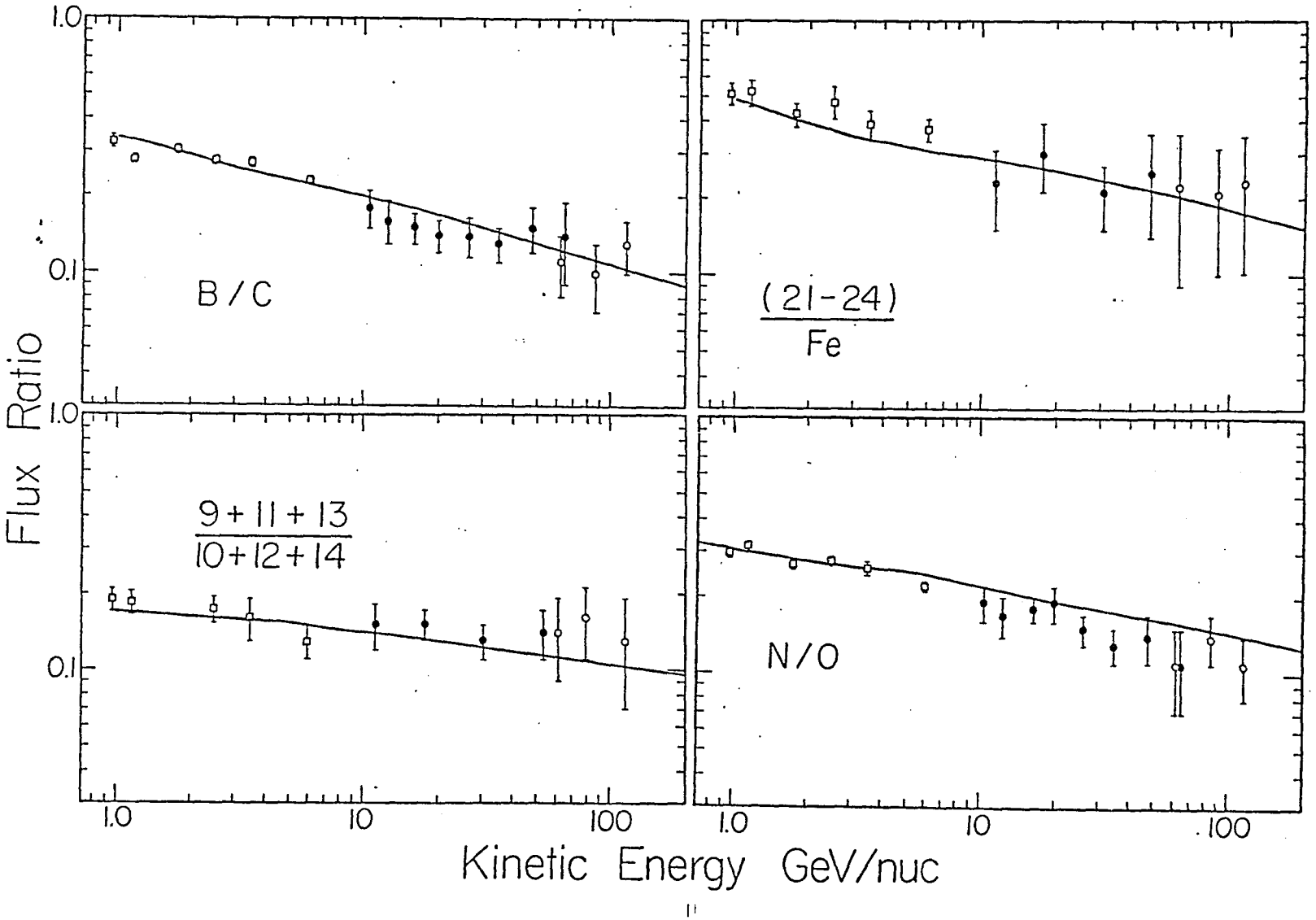
1.0
0.1
B/C
(21-24)
Fe
9+11+13
10+12+14
N/O
Flux Ratio
1.0
10
100
Kinetic Energy GeV/nuc

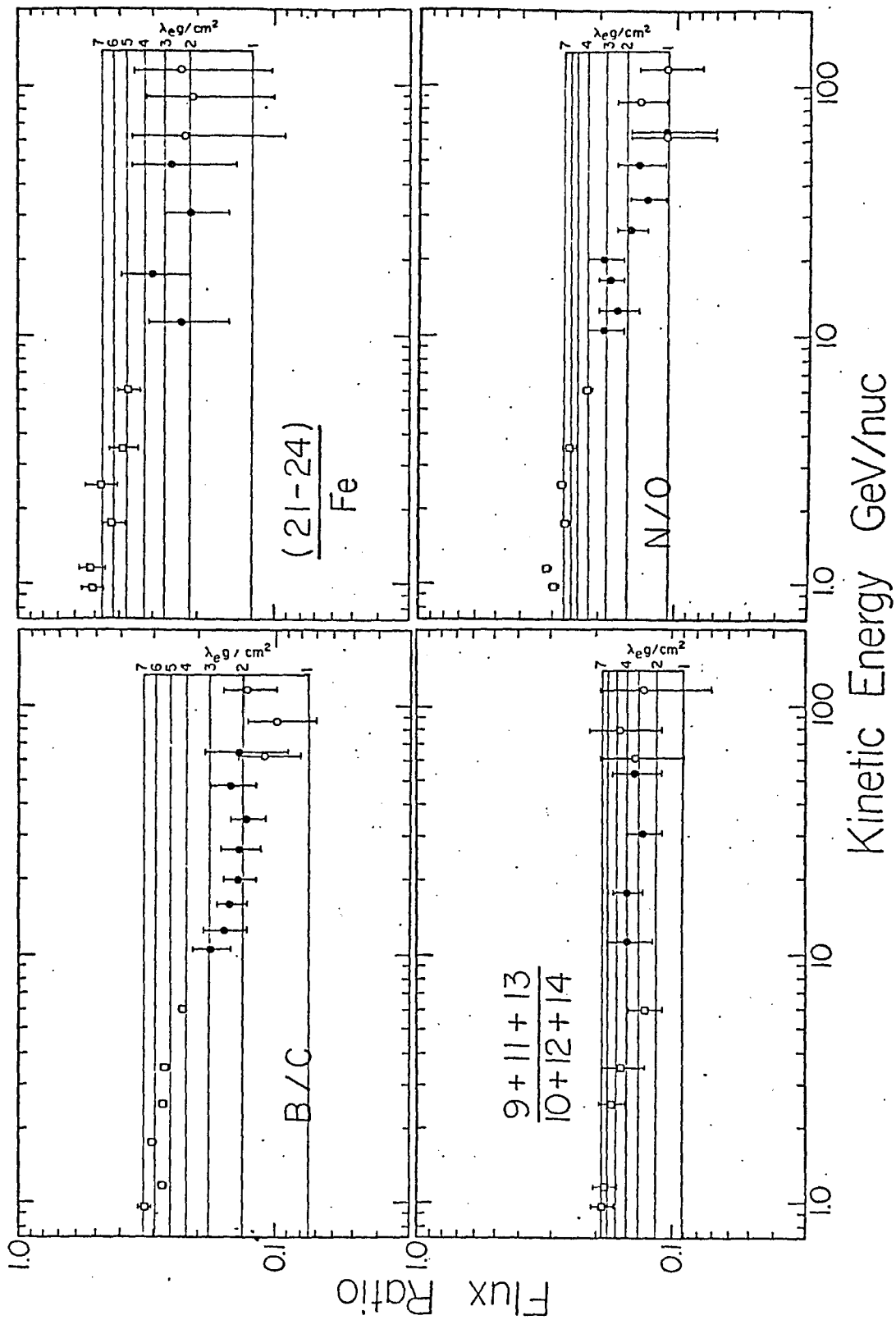

VII.3 Secondary to primary ratios as a function of traversed matter

box model. The parameters used in the calculation are discussed in Chapter V-2. The individual ratios for the three flights have been averaged in cases where the data points overlap. The resulting error bars on the energy scales have not been plotted. The low energy data points spanning the energy range 0.95 to 6.0 GeV/nuc are those reported from Lezniak and Webber 1978. The expected secondary to primary ratios were calculated using a leaky box model with a path length distribution of

7.2) $P(x)=\exp(-x/\lambda)$

where λ is treated as a energy independent variable of constant grammage. The observed and expected ratios are shown in Figure VII.3 for different values of the escape mean free path λ . The general observations of the data indicate that all of the ratios decrease as a function of energy. The ratios imply that the primaries have traversed a path length of ~7g/cm at 1 GeV/nuc which steadily decreases to about ~1.5 g/cm at 100 GeV/nuc.

In the propagation calculations we have assumed that boron and charges 21 through 24 have a zero source component. The other ratios that are thought to have a non-zero source component were adjusted to bring them into agreement with the boron to carbon and the 21 through 24 to iron ratios. The source components derived indicate that

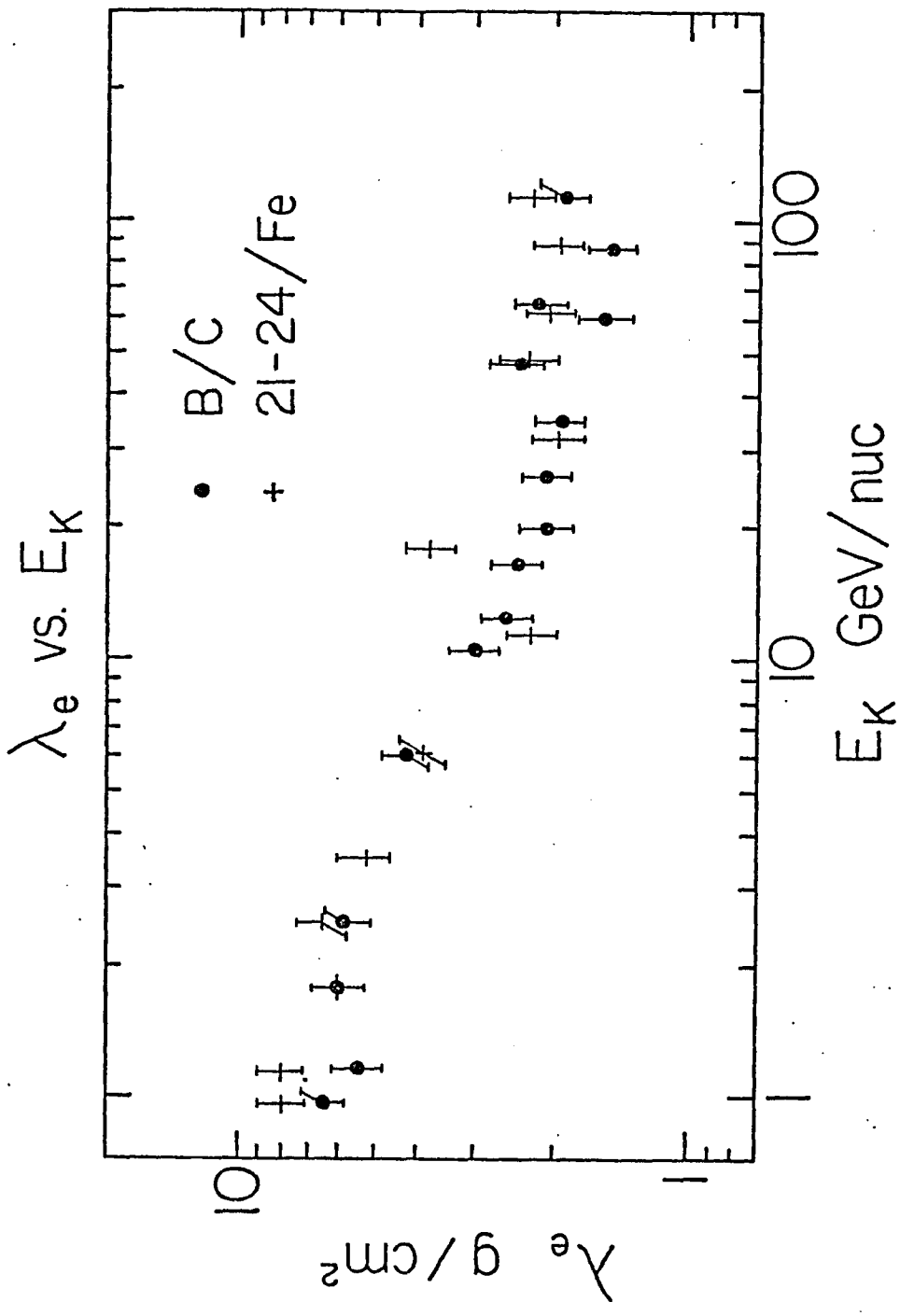

VII.4 Escape mean free path as a function of E

$(17-19)_S = .035\ Fe_S$

$(9+11+13)_S = .047\ (10+12+14)_S$

$N_S = .05\ O_S$

The 21-24/Fe ratio is probably the most reliable of the group due to the lack of contamination from higher charge groups although the boron to carbon ratio has the best statistics and the spallation crossections are well known. The lower charge groups are dependent on the accurate knowledge of the partial cross sections from the primary species above the observed fragment. It should be noted that in spite of the uncertainties in the cross-sectional measurements, all of the escape lengths inferred from the ratios are in remarkably close agreement. The B/C and 21-24/Fe ratios have been plotted versus their apparent exponential escape length in Figure VII.4. Individual exponential fits have been calculated and are presented in Table VII.1. Using the combined data set, the average escape mean free path is

7.3) $\lambda_e = (7.21 \pm .86) E_K^{-(0.32 \pm 0.10)}$

over the energy range from 1.0 to 100.0 GeV/nuc.

TABLE VII.1

Power fits to individual secondary to primary ratios

Ratio	exponent (Ek)	exponent (E-total)
B/C	-0.322 ± 0.027	-0.369 ± 0.033
21-24/Fe	-0.330 ± 0.034	-0.378 ± 0.042
17-19/Fe	-0.289 ± 0.059	-0.324 ± 0.072
9+11+13/10+12+14	-0.166 ± 0.049	-0.184 ± 0.059
N/O	-0.476 ± 0.036	-0.548 ± 0.041

Although the statistics are limited, the data shows a possible flattening of the escape mean free path at high energies. If this feature is correct, it would indicate a break in the energy dependence of the escape mean free path. This flattening would indicate that the escape length is becoming comparable to or less than the thickness of the confinement volume.

In the context of a diffusive model, Owens and Jokipii (1977) have pointed out the inter-relationship of the escape mean free path and the diffusion coefficient. If the interstellar magnetic field fluctuations are of the order $P(k) \sim k^{-5/3}$, where k is the wave number, then this Kolomogorov scattering spectrum will result in a diffusion coefficient of $D \sim R^{1/3}$ where R is the particle rigidity. This would lead to an escape mean free path variation of

$\sim E^{-1/3}$ at these energies. This rigidity is dependent upon the power spectrum of the magnetic field. Cearsky et al. has pointed out that the escape mean free path with an energy dependence greater than -0.6 would have difficulty in explaining the observed anisotropies.

Other experimental determinations of the energy dependence are summarized in Table VII.2 and Figure VII.6. This determination of the energy dependence escape mean free path (in total energy) in this thesis is in good agreement with Lezniak and Webber (1978) and Simon et.al. (1979).

TABLE VII.2

EXPERIMENTAL DETERMINATION OF λ BY:

This work	$\lambda \sim \exp[-0.37 \pm 0.13]$
Orth et al. (1979)	$\lambda \sim \exp[-0.60 \pm 0.10]$
Simon et al. (1979)	$\lambda \sim \exp[-0.40 \pm 0.10]$
Lezniak and Webber (1978)	$\lambda \sim \exp[-0.30 \pm 0.06]$
Ormes and Frier (1978)	$\lambda \sim \exp[-0.40 \pm 0.10]$
Caldwell (1977)	$\lambda \sim \exp[-0.59 \pm 0.09]$
Jullussion (1972)	$\lambda \sim \exp[-0.40 \pm 0.05]$

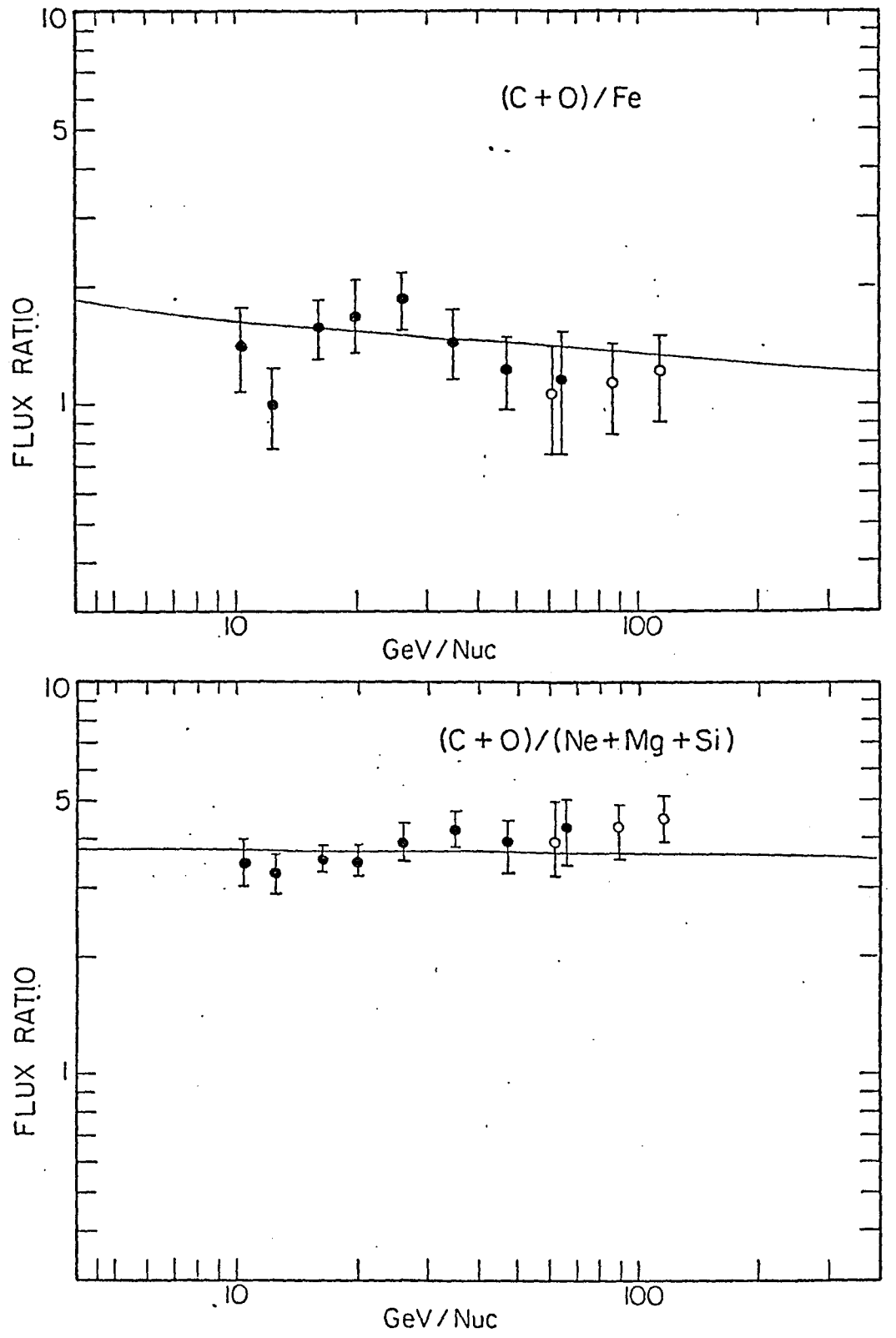

VII.5 Primary to primary ratios

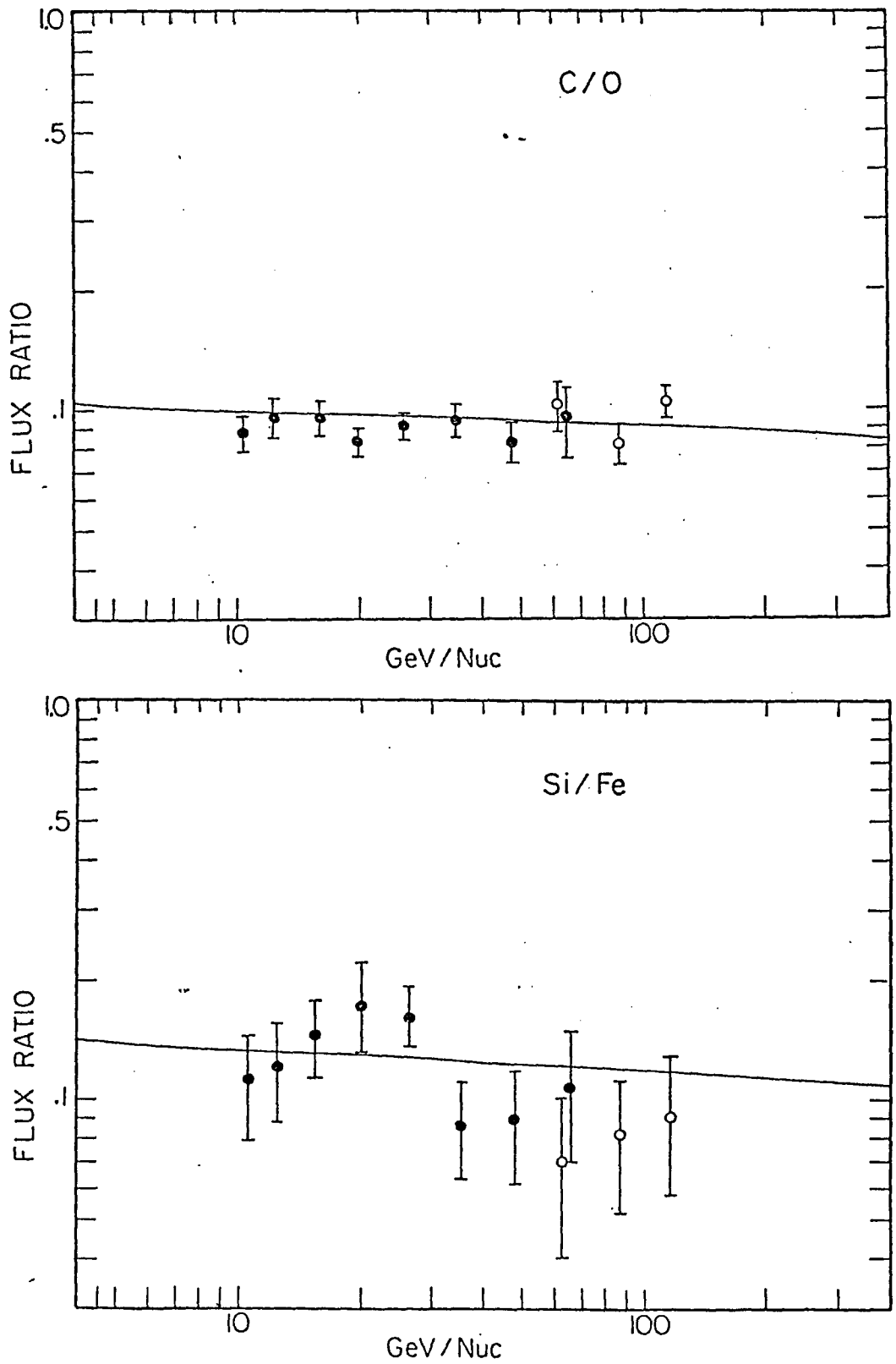

VII.5 (cont'd) Primary to primary ratios

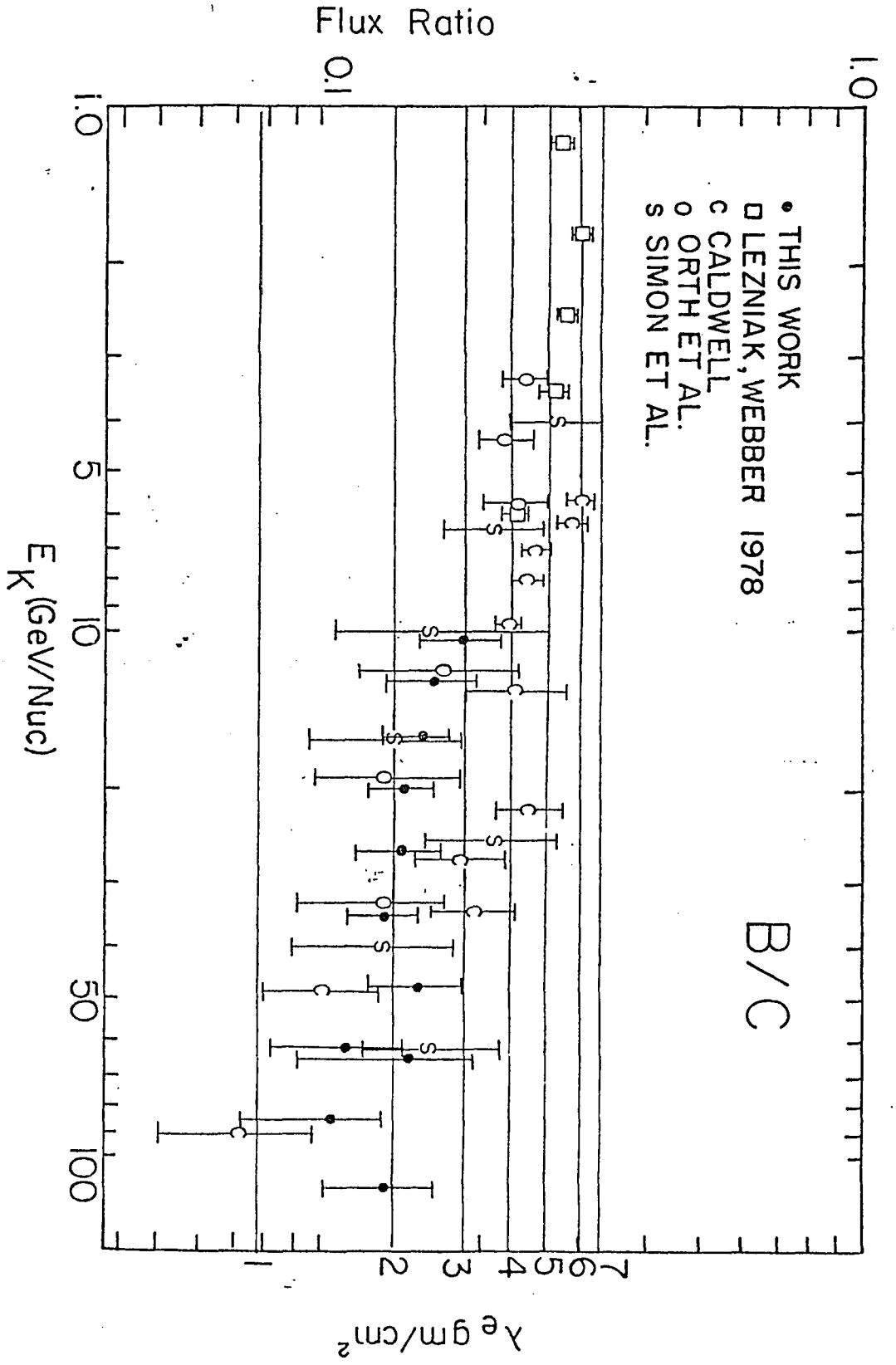

VII.6 Other experimental determinations of the Boron to Carbon ratios

Further insight can be gained on the injection spectrum by observations of high energy species where the interaction lengths are much larger than the escape lengths (ie.). Equation 6.20 can be simplified in the high energy limit such that the observed spectrum is related to the injection spectrum by

7.4) $q_i \cong \frac{j_i}{\lambda}$

Since the escape mean free path can be expressed as a power law, $E_K^{-\gamma}$, then the injection spectrum must be a factor of harder than the observed proton- He spectra where $\lambda_i = 33.5$ g/cm^2 $>> \lambda_{esc} = 2.0$ g/cm^2. At energies greater than 50 GeV/nuc the observed proton spectrum is $j(E) = E^{-2.71}$ (Ryan et. al. 1972). Therefore the injection spectrum chosen for the propagation calculations was chosen to be

7.5) $j(E) = E_K^{-2.4}$

This spectrum is somewhat steeper than one would expect from a model that accelerates cosmic rays by shock acceleration.

VII-4) Conclusion

In this thesis we have measured the charge and energy spectra of the high energy cosmic rays spanning an energy range from 10 to 100 GeV/nuc and a charge range of Z=4

through Z=26. The changing spectral indices can be explained in terms of a leaky box propagation model with a energy dependent escape mean free path as discussed in Chapter VII. Systematic investigation of the primary and secondary components indicate an energy dependent escape mean free path of

$$\lambda_e = (7.21 \pm .86) E_K^{-(0.32 \pm 0.10)}$$

for energies greater than 1 GeV/nuc. This result is consistent with a diffusive scattering propagation model that contains a Kolomogorov spectrum of magnetic irregularities in the galaxy. There are indications in this measurement that the energy dependence of the secondary to primary ratios is becoming softer at the higher energies. Investigations of the primary to primary ratios are consistent with a model where the cosmic rays are injected into the interstellar medium with an injection spectrum of the form

$$7.7) \quad j(E) = E_K^{-2.4}$$

and does not require an charge dependent source spectrum. The source abundances presented by Lezniak and Webber (1978) were used in the propagation calculations (except where noted) and provide good fits to the observed data.

This measurement has provided the best statistical determination of the high energy cosmic ray spectrum made to date (~ 20 m^2-sr-hr). This, combined with the consistency requirements that were placed on the three experiments, has proven to be an exceedingly sensitive test for the removal of systematic errors in the derivation of the spectrum. In this thesis the instrumental corrections have been reduced down to a degree where the major source of error in determining the cosmic ray intensities lies in the uncertainities in the fragmentation cross section parameters in the interstellar medium and the atmosphere. These interaction parameters, as well as accurate measurements that extend above and below the energy range investigated by this thesis, are needed in order to understand more fully the complex problems of nucleosysthesis, acceleration, and propagation of cosmic rays in our galaxy.

BIBLIOGRAPHY

Axford, W.I., Lear, E., and Skadron, G., 1977, Proc. 15 Int. Cosmic Ray Conf., Plovdiv

Baade, W., and Zwicky, F. 1934, Phys. Rev. 45,138.

Bell, A. 1978, M.N.R.A.S., 182,147.

Blandford, R.C., and Ostriker, J.P., 1978, Ap.J., 221, L29.

Blandford, R.D., and Ostriker, J.P., 1980, Ap. J.,237,793.

Caldwell, J.H., 1977 Ap.J. 218,269

Cesarsky, C.S. and Audouze, J. 1974, Astr. Ap., ~30,119

Garcia Munoz, M., Mason, G.M., Simpson, J.A. and Wefel, J.P., Proc. 15 Int. Cosmic Ray Conf., Plovdiv, OG-62.

Cowsik, R., and Wilson, L.W., 1975 Proc. 14 Int. Cosmic Ray Conf. 2, 475.

Fermi, E. 1949 Phys. Rev., 75, 1169.

Jones, F.C., 1979, Ap. J.,229,747.

Julliuson, E. 1949, Phys. Rev. 75, 331.

Lezniak, J.A., 1975, Nucl. Inst. and Methods, 126, 129.

Lezniak, J.A., 1976, Nucl. Inst. and Methods, 136, 299.

Lezniak, J.A., and Webber, W.R., 1978, Ap. J., 223, 676.

Lezniak, J.A., and Webber, W.R., 1979, Astrophys. and Space Sci.,63, 35.

Lezniak, J.A., 1979, Astrophys. and Space Sci.,63,279.

Lindstrom, P.J., Greiner, D.E., Heckman, H.H., Cork, B. and Bieser, F.S., 1975, preprint L.B.L. No. 3650.

Owens, A.J., 1977, Ap. Space Sci., 44,35.

Owens, A.J., and Jokippi, R. 1977, Ap. J., 215,677.

Ormes, J. and Frier, P., 1978, Ap. J.,222, 471.

Orth, C.D., Buffington, A., Smoot, G.F., and Mast, T.S., 1978 Ap. J.,226,1147.

Peron, C., 1976, Phys. Rev. C, 14,1108.

Peters, B. and Westergard, J.,

Ryan, M.J., Ormes, J.F., and Balasubrahmanyan, V.K., 1972, Phys. Rev. Lett., 28, 985.

Scott, J.S., and Chevalier, R.A., 1975, Ap. J., 197, L5.

Silberberg, R., and Tsao, C.H., 1973, Ap. J. Suppl. 25, 315.

Silberberg, R., and Tsao, C.H., 1977, Proc. 15 Int. Cosmic Ray Conf., Plovdiv.

Shapiro, M.M., Silberberg, R., and Tsao, C.H., 1975, Proc. 14 Int. Cosmic Ray Conf., Munich, 2, 532.

Simon, M., Spiegelhauer, H., Schmidt, W., Siohan, F. Ormes, J., Balasubrahmanyan, V.K., and Arens, J.F. 1980, Ap.J., 239, 712.

Simpson, G.A., 1977, Ph.D. Thesis, University of New Hampshire.

Sterheimer, R.M., 1961, Nuclear Physics Vol 5, part A, Yaun, L. and Wu, C. ed., Academic Press.

Webber, W.R., Damle, S.V., and Kish, J.C., 1972, Ap. Space Sci., 15, 245.

Webber, W.R., Lezniak, J.A., and Kish, J. 1973, Ap. J. 183, L81.